ABSTRACT

Title of dissertation: ANALYSIS OF AIR QUALITY WITH NUMERICAL SIMULATIONS (CMAQ), AND OBSERVATIONS OF TRACE GASES

Patricia Castellanos
Doctor of Philosophy, 2009

Dissertation directed by: Dr. Sheryl H. Ehrman
Department of Chemical and Biomolecular Engineering

Professor Russell R. Dickerson
Department of Atmospheric and Oceanic Science

Ozone, a secondary pollutant, is a strong oxidant that can pose a risk to human health. It is formed from a complex set of photochemical reactions involving nitrogen oxides (NO_X) and volatile organic compounds (VOCs). Ambient measurements and air quality modeling of ozone and its precursors are important tools for support of regulatory decisions, and analyzing atmospheric chemical and physical processes. I worked on three methods to improve our understanding of photochemical ozone production in the Eastern U.S.: a new detector for NO_2, a numerical experiment to test the sensitivity to the timing to emissions, and comparison of modeled and observed vertical profiles of CO and ozone. A small, commercially available cavity ring-down spectroscopy (CRDS) NO_2 detector suitable for surface and aircraft

monitoring was modified and characterized. The CRDS detector was run in parallel to an ozone chemiluminescence device with photolytic conversion of NO_2 to NO. The two instruments measured ambient air in suburban Maryland. A linear least-squares fit to a direct comparison of the data resulted in a slope of 0.960±0.002 and R of 0.995, showing agreement between two measurement techniques within experimental uncertainty. The sensitivity of the Community Multiscale Air Quality (CMAQ) model to the temporal variation of four emissions sectors was investigated to understand the effect of emissions' daily variability on modeled ozone. Decreasing the variability of mobile source emissions changed the 8-hour maximum ozone concentration by ±7 parts per billion by volume (ppbv). Increasing the variability of point source emissions affected ozone concentrations by ±6 ppbv, but only in areas close to the source. CO is an ideal tracer for analyzing pollutant transport in AQMs because the atmospheric lifetime is longer than the timescale of boundary layer mixing. CO can be used as a tracer if model performance of CO is well understood. An evaluation of CO model performance in CMAQ was carried out using aircraft observations taken for the Regional Atmospheric Measurement, Modeling and Prediction Program (RAMMPP) in the summer of 2002. Comparison of modeled and observed CO total columns were generally in agreement within 5-10%. There is little evidence that the CO emissions inventory is grossly overestimated. CMAQ predicts the same vertical profile shape for all of the observations, i.e. CO is well mixed throughout the boundary layer. However, the majority of observations have poorly mixed air below 500 m, and well mixed air above. CMAQ appears to be transporting CO away from the surface more quickly than what is observed.

Turbulent mixing in the model is represented with K-theory. A minimum K_Z that scales with fractional urban land use is imposed in order to account for subgrid scale obstacles in urban areas and the urban heat island effect. Micrometeorological observations suggest that the minimum K_Z is somewhat high. A sensitivity case where the minimum K_Z was reduced from 0.5 m^2/s to 0.1 m^2/s was carried out. Model performance of surface ozone observations at night increased significantly. The model better captures the observed ozone minimum with slower mixing, and increases ozone concentrations in the residual layer. Model performance of CO and ozone morning vertical profiles improves, but the effect is not large enough to bring the model and measurements into agreement. Comparison of modeled CO and O_3 vertical profiles shows that turbulent mixing (as represented by eddy diffusivity) appears to be too fast, while convective mixing may be too slow.

ANALYSIS OF AIR QUALITY WITH NUMERICAL SIMULATIONS (CMAQ), AND OBSERVATIONS OF TRACE GASES

by

Patricia Castellanos

Dissertation submitted to the Faculty of the Graduate School of the
University of Maryland, College Park in partial fulfillment
of the requirements for the degree of
Doctor of Philosophy
2009

Advisory Committee:
Associate Professor Sheryl H. Ehrman, Chair/Advisor
Professor Russell R. Dickerson, Co-Advisor
Professor Robert D. Hudson
Assistant Professor Chunsheng Wang
Assistant Professor Jeffery B. Klauda

Dedication

Para la abuela.

Acknowledgments

Special thanks to my co-advisors Sheryl Ehrman and Russ Dickerson for guidance, inspiration, and support (and especially for helping me find a job!!). Thanks to Jeff Stehr for his infinite patience and high threshold for persistent questioning. Thanks to Winston Luke and Paul Kelley at NOAA/ARL for taking the time out to bring their intrument to UMD. Thanks to Bill Thorn at NIST for helping out with the calibration. I would also like to thank all the RAMMPP folks at UMD and MDE for a great collaborative four years. Finally, a big thanks to my all my friends, family, lab mates, and fellow grad students. I wouldn't have made it without you.

Funding for this work was provided by the Maryland Department of the Environment and the Maryland Department of Natural Resources.

Table of Contents

List of Tables vi

List of Figures vi

List of Abbreviations xiv

1 Introduction 1
1.1 Overview . . . 1

2 Background 4
2.1 Ground-level Ozone . . . 4
2.2 Ozone Chemistry . . . 6
2.3 The Planetary Boundary Layer . . . 8
2.4 Meteorological Conditions Associated with Ozone . . . 10
2.5 Air Quality Models . . . 11
2.5.1 Emissions Modeling: Primary Pollutants, Emissions Inventories, and SMOKE . . . 13
2.5.2 Meteorological Modeling: MM5 . . . 17
2.5.3 Meteorology-Chemistry Interface Processor (MCIP) . . . 18
2.5.4 Chemical Transport Modeling: CMAQ . . . 19
2.5.5 Air Quality Monitoring . . . 23
2.6 AQM Sensitivity to Temporal Distribution of Emissions . . . 26
2.7 CMAQ Model Performance of CO . . . 27
2.8 Analysis of Vertical Turbulent Mixing in CMAQ . . . 28
2.9 Measurement of NO_2 Using Cavity Ring-Down Spectroscopy . . . 29

3 Sensitivity to Temporal Distribution of Emissions 31
3.1 Introduction . . . 31
3.2 Emissions Scenarios . . . 33
3.3 Modeling Domain . . . 35
3.4 Meteorology . . . 35
3.5 Modeling . . . 36
3.6 Observational Data and Model Performance Evaluation . . . 36
3.7 Results . . . 38
3.7.1 Emissions . . . 38
3.7.2 Regional Sensitivities to Uniform Temporal Distributions . . . 39
3.7.3 Regional Sensitivity to Increased Variation in Temporal Distributions. . . . 46
3.7.4 Local Sensitivities . . . 53
3.8 Discussion and Implications . . . 60

4 CMAQ Model Performance of CO 64
4.1 Introduction . . . 64
4.2 Modeling Set-Up . . . 66
4.3 Measurement of CO Vertical Profiles and at CO Surface Sites . . . 66
4.4 Results and Discussion . . . 67
4.4.1 Comparison of Modeled and Observed CO Vertical Profiles . 67
4.5 Conclusions . . . 86

5 Analysis of CMAQ Turbulent Vertical Mixing 87
5.1 Introduction . . . 87
5.2 Modeling Set-up . . . 91
5.3 Observed CO and O_3 Vertical Profiles . . . 92
5.4 Surface Observations of CO, O_3, and NO_X . . . 95
5.5 Results and Discussion: CMAQ Model Performance for $K_Z min = 0.5$ m^2/s and 0.1 m^2/s . . . 95
5.5.1 Model Comparison to AQS and CASNET O_3 Surface Observations . . . 95
5.5.2 Model Comparison to AQS O_3 and NO_X Surface Observations 96
5.5.3 Model Comparison to AQS CO Surface Observations . . . 105
5.5.4 Model Comparison to Observed CO & O_3 Vertical Profiles . . 105
5.6 Conclusions . . . 112

6 Measurement of NO_2 Using Cavity Ring-Down Spectroscopy 114
6.1 Introduction . . . 114
6.2 Cavity Ring-Down Spectroscopy . . . 117
6.3 Experimental Method . . . 119
6.3.1 Cavity Ring-Down Spectrometer . . . 119
6.3.2 Photolysis Followed by Chemiluminescence . . . 120
6.3.3 Intercomparison on Ambient Air . . . 122
6.4 Results . . . 122
6.4.1 Detection Limit and Response Time . . . 122
6.4.2 Calibration and Water Interference . . . 123
6.4.3 Ambient Intercomparison . . . 126
6.5 Discussion . . . 129

7 Conclusions 133
7.1 Overview . . . 133
7.2 Recommendations For Future Work . . . 136

Bibliography 139

List of Tables

2.1 2002 National (a) and Northeast (b) emissions by category in kilograms per year. 15

3.1 List of simulations and emissions combinations. 34

4.1 Comparison of observed and modeled change in total CO between downwind and upwind vertical profiles. 81

4.2 Summary of published observations of CO deposition velocity over various types of vegetation. 85

5.1 Linear least squares fit to a scatter plot of observed and modeled ozone at urban and rural monitoring sites. 96

6.1 A comparison of the performance statistics for a Thermo Electron Corp. chemiluminescence analyzer (as reported by the manufacturer), the CRDS analyzer, and the NOAA chemiluminescence instrument. 123

List of Figures

2.1 Counties in the U.S. out of compliance with the NAAQS as of June 2009. Figure obtained from www.epa.gov/oar/oaqps/greenbk. 5

2.2 Diagram of the diurnal variation of the planetary boundary layer. . . 9

2.3 Flow diagram of the EPA Models3 modeling system. The outputs of the SMOKE and MM5 models are used as inputs to CMAQ. Some MM5 outputs are used in SMOKE processing of biogenic, mobile, and point source emissions, which are a function of atmospheric dynamics. 12

2.4 Relative contributions of the five source categories to the 2002 National Emissions Inventory (right) and 2002 Emisisons in the Northeast (left). 16

3.1 The August 21, 2002 domain total hourly NO_X emissions for the (a) Base Case (BC), Area Uniform (AU), Mobile Uniform (MU), Point Uniform (PU), and Non-road Uniform (NU) simulations, and the (b) Base Case (BC), Area Increased Variability (AI), Mobile Increased Variability (MI), Point Increased Variability (PI), and Non-road Increased Variability (NI) sensitivity simulations. 40

3.2 The base case domain total nighttime (12:00 am - 7:00 am EST and 7:00 pm - 12:00 pm EST) and daytime (7:00 am - 7:00 pm EST) NO_X (left) and VOC (right) emissions by emissions sector on August 21, 2002. 40

3.3 The mean bias $\left(\frac{1}{N}\sum \text{Uniform case - base case}\right)$ between the AU (a), PU (b), MU (c), and NU (d) case and the base case in the daily 8HRMAX in each grid cell from May 15 to September 15. 42

3.4 The mean bias between the AU (a, b), NU (c, d), PU (e, f), ... 43

3.5 The difference between the AU (a), NU (b), PU (c), and MU (d) case and the base case in the number of days that the 8HRMAX exceeds 80 ppbv from May 15 to September 15.In areas where the base case predicted 20-30 days of exceedances, the MU case predicts 5-8 less days. 45

3.6 The frequency distribution of the 8HRMAX in urban (circles) and rural (triangles) areas in the base case (open markers) and MU case (filled markers). The top right corner inset is an enlargement of the right tail of the frequency distribution. In urban areas the fraction of 70-95 ppbv 8HRMAX concentrations decrease, and the fraction of 40-60 ppbv 8HRMAX concentrations in the MU simulation increases from the base case. 47

3.7 The mean bias between the AI (a), PI (b), MI (c), and NI (d) case and the base case in the daily 8HRMAX in each grid cell from May 15 to September 15. 49

3.8 The mean bias between the AI (a, b), NI (c, d), PI (e, f), and MI (g, h) simulation and the base case in the daily 8HRMAX in each grid cell from May 15 to September 15 when between 50 and 80 ppbv ozone (left column) and greater than 80 ppbv ozone (right column) occurs in the base case. 50

3.9 The difference between the AI (a), NI (b), PI (c), and MI (d) case and the base case in the number of days that the 8HRMAX exceeds 80 ppbv from May 15 to September 15. 51

3.10 The ratio of the average concentration of daytime (7:00 am - 7:00 pm EST) isoprene to NO_X averaged over the summer. In the Ohio River Valley, West Virginia, and areas throughout Georgia and Louisiana there is enough isoprene such that conditions are NO_X limited. Thus, more ozone is generated close to the large point sources when NO_X emissions increase during the day in the PI case. 52

3.11 The location of the PAMS type 2 (triangles), PAMS type 3 (squares), and CASTNET (circles) monitoring sites used for local sensitivity analysis in Baltimore (top) and Atlanta (bottom). 54

3.12 The hourly ozone concentrations averaged in time that were observed (pink squares) and modeled at the Essex (a, b) and Tucker (c, d) monitoring sites. The modeled average hourly ozone concentration plots are separated into uniform (left column) and increased variability (right column) groups. The base case (open triangles) is plotted with both groups. The error bars on the fourth point in each figure correspond to the standard deviation of the observed (pink), base case (black), and mobile case (blue) hourly ozone concentrations, and are typical for all hours. The plot to the right of each diel plot (a-1, b-1, c-1, d-1) is a magnification of these points next to each other to better illustrate the overlapping error bars. At the Essex and Tucker sites, the summer long average decrease from the base case in nocturnal ozone when mobile emissions are uniform is larger than one standard deviation. 56

3.13 The hourly ozone concentrations averaged in time that were observed (pink squares) and modeled at the Aldino (a, b) and Conyers (c, d) monitoring sites. The modeled average hourly ozone concentration plots are separated into uniform (left column) and increased variability (right column) groups. The base case (open triangles) is plotted with both groups. The error bars on the fourth point in each figure correspond to the standard deviation of the observed (pink), base case (black), and mobile case (blue) hourly ozone concentration, and are typical for all hours. The plot to the right of each diel plot is a magnification of this point. 57

3.14 The hourly NO_X concentrations averaged in time that were observed (pink squares) and modeled at the Essex (a, b) and Tucker (c, d) monitoring sites. The modeled average hourly ozone concentration plots are separated into uniform (left column) and increased variability (right column) groups. The base case (open triangles) is plotted with both groups. The error bars on the fourth point in each figure correspond to the standard deviation of the observed (pink), base case (black), and mobile case (blue) hourly ozone concentration, and are typical for all hours. The plot to the right of each diel plot is a magnification of this point. At the Essex site, NO_X model performance improves in the MU case. 59

3.15 The hourly ozone concentrations averaged in time that were observed (pink squares) and modeled at the Arendstville (a, b) and Sand Mountain (c, d) monitoring sites. The modeled average hourly ozone concentration plots are separated into uniform (left column) and increased variability (right column) groups. The base case (open triangles) is plotted with both groups. The error bars on the fourth point in each figure correspond to the standard deviation of the observed (pink), base case (black), and mobile case (blue) hourly ozone concentration, and are typical for all hours. The plot to the right of each diel plot is a magnification of this point. 61

4.1 The locations of some major cities in the Mid-Atlantic 68

4.2 The locations of the morning (7-10 AM local time) CO vertical profiles, with corresponding airport codes. 69

4.3 The locations of the afternoon CO vertical profiles, with corresponding airport codes. 70

4.4 Map of locations of some major cities in the Mid-Atlantic (a), the place marker represent locations of CO surface monitoring sites. . . . 71

4.5 Observed CO vertical profiles at six airports on July 8, 2002. On this day, most of the Mid-Atlantic was affected by a plume of biomass burning emissions that originated in Quebec. These results were first published in Taubman, et al., (2004). 72

4.6 Comparison of modeled and observed (triangles, gray bars) surface CO diurnal variation for sites shown in Figure 4-2. The bars represent the 25th and 75th percentiles, and the markers correspond to the median hourly concentration. The blue bars and circles correspond to modeled CO, and the yellow bars and squares correspond to modeled CO with the deposition velocity set to zero. 73

4.7 Comparison of observed (red) and modeled morning CO vertical profiles paired in time and space. The solid lines are the medians, and the shaded areas represent the 25th and 75th quartiles of the data. The blue line corresponds to modeled CO with the deposition velocity calculated in MCIP v3.4.1, and the green line corresponds to modeled CO with the deposition velocity set to zero. The total CO column below 1000 m is closer to observations when the CO deposition velocity is set to zero, but the shape of the vertical profile does not change. 75

4.8 Comparison of observed (red) and modeled afternoon CO vertical profiles paired in time and space. The solid lines are the medians, and the shaded areas represent the quartiles of the data. The blue line corresponds to model CO with the deposition velocity calculated in MCIP v3.4.1, and the green line corresponds to modeled CO with the deposition velocity set to zero. 76

4.9 Map of the locations of profiles with poorly mixed air near the surface (left; 51 spirals), and profiles with well mixed air throughout the boundary layer (right; 21 spirals), with corresponding airport codes. . 77

4.10 Comparison of observed (red) and modeled afternoon CO vertical profiles when air near the surface is poorly mixed. The solid lines are the medians, and the shaded areas represent the quartiles of the data. The blue line corresponds to model CO with the deposition velocity calculated in MCIP v3.4.1, and the green line corresponds to modeled CO with the deposition velocity set to zero. 78

4.11 Comparison of observed (red) and modeled afternoon CO vertical profiles when the boundary layer is well mixed throughout. The solid lines are the medians, and the shaded areas represent the quartiles of the data. The blue line corresponds to model CO with the deposition velocity calculated in MCIP v3.4.1, and the green line corresponds to modeled CO with the deposition velocity set to zero. 79

4.12 Comparison of the average observed (black) and modeled CO total column for all flights, morning flights (AM Flights), and afternoon flights (PM Flights). The afternoon flights are further subdivided into two groups based on the shape of the observed CO vertical profile: profiles with CO rich air near the surface (PM Stratified group), and 2) profiles with a well-mixed boundary layer (PM Well-mixed group). The light gray corresponds to the modeled CO total column with the deposition velocity calculated in MCIP v3.4.1, and the dark gray bar corresponds to the modeled CO with the deposition velocity set to zero. 82

4.13 Modeled daily average CO deposition velocity in cm/s. 84

5.1 Map of surface AQS (red) and CASTNET (white) O_3 monitoring locations. 93

5.2 Map of surface AQS NO_X monitoring locations. 94

5.3 Medians (black markers) and quartiles (shaded boxes) of observed (gray, squares) and modeled hourly ozone. The red boxes and black circles correspond to the 0.5 $K_Z$min case and the blue boxes and black triangles correspond to the 0.1 $K_Z$min case. Significant improvement in morning model performance occurs when mixing is slowed down. . 97

5.4 Timeseries of the observed (black) and modeled (green, 0.5 $K_Z$min; red, 0.1 $K_Z$min) median O_3 concentrations at all AQS and CASTNET monitoring sites for one week. Results are typical for the length of the simulation. 98

5.5 Medians (black markers) and quartiles (shaded boxes) of hourly ozone (top) and NO_X (bottom) bias at rural monitoring sites for the 0.5 $K_Z$min (red; circles) and 0.1 $K_Z$min cases (blue; triangles). 99

5.6 Medians (markers) and quartiles (boxes) of observed and modeled hourly NO (top) and NO_X (bottom) in rural areas. 100

5.7 Medians (black markers) and quartiles (shaded boxes) of hourly ozone (top) and NO_X (bottom) bias at urban monitoring sites for the 0.5 $K_Z$min (red; circles) and 0.1 $K_Z$min cases (blue; triangles). 102

5.8 Medians (black markers) and quartiles (shaded boxes) of hourly NO bias at urban monitoring sites for the 0.5 $K_Z$min (red; circles) and 0.1 $K_Z$min cases (blue; triangles). 103

5.9 Medians (black markers) and quartiles (shaded boxes) of observed (gray, squares) and modeled hourly NO (top) and NO_X (bottom) concentration in urban areas. 104

5.10 Average relative change in nighttime NO (top) and NO_2 (bottom) dry deposition between the 0.5 $K_Z$min and 0.1 $K_Z$min cases. 106

5.11 Medians (black markers) and quartiles (shaded boxes) of the hourly CO bias at AQS surface monitoring sites for the 0.5 $K_Z$min (red; circles) and 0.1 $K_Z$min cases (blue; triangles). 107

5.12 Comparison of observed (red) and modeled morning CO vertical profiles. The solid lines are the medians, and the shaded areas represent the quartiles of the data. The blue line corresponds to 0.5 $K_Z$min case, and the orange line corresponds to the 0.1 $K_Z$min case. 108

5.13 Comparison of modeled morning CO vertical profiles at 5 AM. The solid lines are the medians, and the shaded areas represent the quartiles of the data. 109

5.14 Comparison of observed (red) and modeled morning ozone vertical profiles. The solid lines are the medians, and the shaded areas represent the quartiles of the data. The blue line corresponds to 0.5 $K_Z$min case, and the orange line corresponds to the 0.1 $K_Z$min case. 110

5.15 Comparison of modeled ozone vertical profiles at 5 AM. The solid lines are the medians, and the shaded areas represent the quartiles of the data. 111

6.1 A schematic diagram of the CRDS apparatus used to measure NO_2. Pressure in the optical chamber is maintained 170 torr (227 hPa). The mirrors, 30 cm apart, reflect 99.95% of the radiation from the 407.38 nm laser resulting in an effective path length approaching 1000 m. 118

6.2 Comparison of NO_2 measured by CRDS to NO_2 concentrations calculated from a known concentration of NO in excess ozone (filled circles) and from the decrease in ozone concentration (open circles) monitored with an ozone detector based on UV absorption. The least squares fit to the data generated from the change in ozone concentration (solid line) has a slope of 1.02 ± 0.02, an intercept of -1.8 ± 1.5 ppbv; R= 0.999. The least squares fit to the data generated from the standard dilution (broken line) has a slope of 0.95 ± 0.01, an intercept of 0.9 ± 0.6 ppbv; R= 0.999. The error bars for each point are the same size or smaller than the circles. 125

6.3 Ambient NO (a) and NO_2 measurements by chemiluminescence (b) and CRDS (c) from January 5, 2009 to January 16, 2009 in a suburban Maryland setting. 127

6.4 Scatter plots of ambient NO_2 measured by CRDS and chemiluminescence on January 5-9, 2009 (a) and January 10-16, 2009 (b). The slope, intercept, and R of the linear least squares fit to the January 5-9, 2009 data are 0.960 ± 0.002, 0.28 ± 0.03ppbv, and 0.995, respectively. The slope, intercept, and R of the linear least squares fit to the January 10-16, 2009 data are 0.932 ± 0.002, -0.61 ± 0.04 ppbv, and 0.982, respectively. The dashed line represents a one to one fit. . 128

6.5 Scatter plot of NO concentrations measured by the NO and dark NO_X channels of the chemiluminescence device on January 5-9, 2009 (open circles) and January 10-16, 2009 (closed circles). The slope drifted from 1.025 ± 0.004 on January 5-9 to 0.949 ± 0.004 on January 10-16. On January 5-9, the two channels of the instrument give consistent measurements of NO over the concentration range observed. After January 10^{th}, the sensitivity of both channels drifted dynamically. . 130

6.6 Diel cycle of ambient NO (a) and NO_2 (b) measurements by chemiluminescence and NO_2 (c) measured by CRDS. The markers are the median hourly concentrations, and the error bars are the 25th and 75th percentiles. High concentrations of NO_2 are seen at night because the temperature inversion inhibits vertical mixing and high concentrations of NO are seen during the daylight hours because solar UV radiation photolyzes NO_2 to NO. 131

List of Abbreviations

α	alpha
β	beta
8HRMAX	daily 8-hour maximum ozone concentration
AQM	air quality model
AQS	Air Quality System
CASTNET	Clean Air Status and Trends Network
CBIV	carbon bond IV
CEM	continuous emissions monitor
CENRAP	Central Regional Air Planning Association
CMAQ	Communit Multiscale Air Quality Model
CRDS	Cavity Ring-Down Spectroscopy
EBI	Euler backward iterative
EI	emissions inventory
EPA	United States Environmental Protection Agency
FE	fractional error
IMPROVE	Interagency Monitoring of Protected Visual Environments
km	kilometer
MANE-VU	Mid-Atlantic/Northeast Visibility Union
MCIP	Meteorology-Chemistry Interface Processor
MM5	Mesoscale Model 5
MRPO	Mid-West Regional Planning Organization
NAAQS	National Ambient Air Quality Standards
NEI	National Emissions Inventory
NO_x	oxides of nitrogen
NMB	normalized mean bias
OTR	Ozone Transport Region
SIP	state implementation plan
SMOKE	Sparse Matrix Operator Kernel Emissions
STN	Speciation Trends Network
USA	United States of America
VISTAS	Visibility Improvement State and Tribal Association of the Southeast
VOC	volatile organic compound

Chapter 1

Introduction

1.1 Overview

Ozone is a recalcitrant problem in most major cities in the United States. It is a secondary pollutant formed from a complex set of photochemical reactions involving nitrogen oxides (NO_X) and volatile organic compounds (VOCs). Because ozone is a strong oxidant, acute short-term exposure and moderate long-term exposure can pose a risk to human health.

Ambient measurements and air quality modeling of ozone and its precursors are important tools for decision support, regulatory attainment analysis, creation of emissions control strategies, analysis of regional atmospheric chemistry and transport, and for basic insight into the chemistry and physics of the atmosphere. In this work, analysis of the Community Multiscale Air Quality (CMAQ) model will be discussed, followed by modification and evaluation of a new commercially-available Cavity Ring-Down Spectroscopy (CRDS) NO_2 detector for ambient monitoring in polluted environments.

Chapter 2 will include background information related to ozone chemistry, meteorological conditions associated with high ozone and pollutant transport, and air quality modeling formulations. In Chapter 3, the sensitivity of ozone simulated by CMAQ to the temporal variation of area, point, mobile, and non-road emissions

sectors will be investigated. Hourly emissions fluxes that are air quality model inputs are less variable than corresponding measurements would imply. Before going to the expense of creating inventories that represent real world variability, we would like to know how sensitive the model is to the temporal variability of emissions. These results have appeared in Castellanos et al. (2009a). In Chapter 4, a CO model performance evaluation in CMAQ will be presented using aircraft observations taken for the Regional Atmospheric Measurement, Modeling and Prediction Program (RAMMPP) in the summer of 2002, and high precision surface observations. An evaluation of CO in CMAQ is needed in order to use the model as a tool for investigating the role of pollutant transport in ozone formation. Chapter 5 contains an analysis of a sensitivity case where nighttime vertical mixing in CMAQ is slowed down. Turbulent mixing in the model, represented with K-theory, appears to be overestimated. A minimum K_Z that scales with fractional urban land use is imposed in order to account for subgrid scale obstacles in urban areas and the urban heat island effect. Micrometeorological observations suggest the minimum K_Z used in the model is somewhat high. The results of a sensitivity case where the minimum K_Z was reduced from 0.5 m^2/s to 0.1 m^2/s are presented. The impact of overestimated vertical mixing on the model's ability to simulate long-range transprot is discussed. In Chapter 6, results from the modification of a commercial Cavity Ring-Down Spectroscopy (CRDS) NO_2 detector and an ambient intercomparison with an ozone chemiluminescence device with photolytic conversion of NO_2 to NO are presented. These results have appeared in Castellanos et al. (2009b). This is followed by a summary of results and conclusions, and recommendations for future

work in Chapter 7.

Chapter 2

Background

2.1 Ground-level Ozone

The generation of ozone, a secondary pollutant formed from a complex set of photochemical reactions involving nitrogen oxides (NO_X) and volatile organic compounds (VOCs), is driven by high temperatures and sunlight (Crutzen, 1973, Seinfeld and Pandis, 2006). In the stratosphere ozone acts as a shield from harmful ultraviolet rays, but in the troposphere, ozone is a strong oxidant that irritates membranes such as eyes and lungs and can damage plants (vanLoon, 2000). Increases in mortality, morbidity, hospital admissions, and reduced lung function in children have been associated with exposure to high ozone concentrations (Burnett, et al., 1994, White, et al., 1994, Frischer T, et al., 1999, Buchdahl, et al., 2000, Wong, et al., 2001, Gauderman, et al., 2002, Ruidavets, et al., 2005, Ayres, et al., 2006). Both acute short-term exposure and moderate long-term exposure to ozone pose a risk to human health. For this reason, the U.S. Environmental Agency (EPA) limits ozone concentrations averaged over 8-hours with the National Ambient Air Quality Standards (NAAQS).

Ozone concentrations exceeding the 1997 NAAQS of 0.08 parts per million by volume (ppmv) averaged over 8-hours are a longstanding problem in many Northeast urban/suburban areas despite a decreasing trend in emissions of ozone precursors

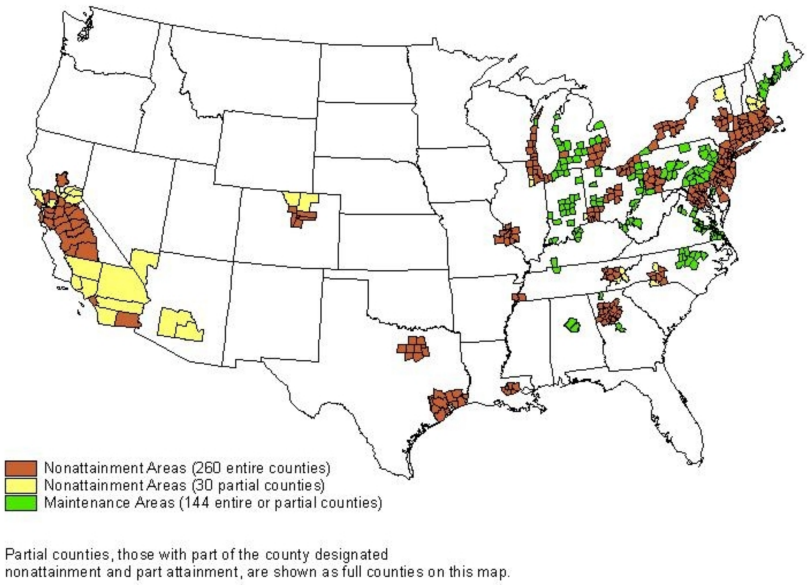

Figure 2.1: Counties in the U.S. out of compliance with the NAAQS as of June 2009. Figure obtained from www.epa.gov/oar/oaqps/greenbk.

at the national level (Figure 2.1) (U.S. EPA, 2004). In 2008, the 0.075 ppmv 8-hour average NAAQS was put forth, and in 2009 the EPA Administrator agreed to consider even tighter standards, putting additional pressure on policy makers to create effective emissions control strategies on a local and regional level. Ozone concentrations at the level of the new standard are close to the background level of 35 parts per billion by volume (ppbv), which is dependent on large-scale processes, making the region of influence for a nonattainment area larger. A collective emissions control effort involving a larger geographic area, and understanding the role of regional transport on daily ozone concentrations will be needed (Fiore, et al., 2002, Civerolo, et al., 2003, Williams, et al., 2009).

2.2 Ozone Chemistry

In the presence of NO_2 and light, ozone is produced by the following reactions:

$$NO_2 + h\nu(\lambda < 424nm) \rightarrow NO + O \tag{2.1}$$

$$O + O_2 + M \rightarrow O_3 + M \tag{2.2}$$

However, ozone readily reacts with the NO produced in 2.1 to form a steady state between ozone and NO_2.

$$O_3 + NO \rightarrow NO_2 + O_2 \tag{2.3}$$

A second pathway involving VOCs and a hydroxyl radical that converts NO to NO_2 without destroying ozone drives ozone formation beyond this steady state resulting in net accumulation (RH is any reactive hydrocarbon).

$$RH + OH\cdot \rightarrow R\cdot + H_2O \tag{2.4}$$

$$R\cdot + O_2 + M \rightarrow RO_2\cdot + M \tag{2.5}$$

$$RO_2\cdot + NO \rightarrow RO\cdot + NO_2 \tag{2.6}$$

$$RO\cdot + O_2 \rightarrow RCHO + HO_2\cdot \tag{2.7}$$

$$HO_2\cdot + NO \rightarrow OH\cdot + NO_2 \tag{2.8}$$

$$2(NO_2 + h\nu \rightarrow NO + O) \tag{2.9}$$

$$\underline{2(O + O_2 + M \rightarrow O_3 + M)} \tag{2.10}$$

$$RH + 4O_2 + 2h\nu \rightarrow RCHO + 2O_3 + H_2O \tag{2.11}$$

A third pathway involving attack of OH on CO will also produce an HO_2 radical. However, because the rate of this reaction is slow (the lifetime of CO is on the order of weeks), CO plays a minor role in daily ozone formation. This makes CO an excellent tracer for tracking regional pollution.

Sources of hydroxyl radicals include photodissociation of ozone (2.12 & 2.13), nitrous acid (HONO), and hydrogen peroxide (H_2O_2).

$$O_3 + h\nu(\lambda < 340nm) \rightarrow O(^1D) + O_2 \tag{2.12}$$

$$O(^1D) + H_2O \rightarrow 2OH \tag{2.13}$$

The ozone formation reaction cycle is terminated by the loss of HO_X (HO + HO_2) radicals by self-reaction or by oxidation of NO_2 at high NO_X concentrations.

$$HO_2 + HO_2 \rightarrow H_2O_2 + O_2 \tag{2.14}$$

$$NO_2 + OH + M \rightarrow HNO_3 + M \tag{2.15}$$

The predominant sources of NO_X are anthropogenic high temperature combustion processes such as the burning of fossil fuels in cars and power plants. Natural sources of NO_X include NO emissions from soil, natural fires, lightning, and the oxidation of NH_3 by photochemical processes in oceans and terrestrial plants (Finlayson-Pitts, 1999).

Biogenic emissions are the main source of VOCs in the Northeast. Plants emit thousands of organic compounds (Seinfeld and Pandis, 2006). The most abundant class of compounds is terpenes, made up of isoprene (C_5H_8) and various isoprene polymers called monoterpenes (two isoprenes), sesquiterpenes (three isoprenes), etc.

These are highly photochemically reactive compounds that play a significant role in ozone and aerosol formation. Anthropogenic sources of VOCs are solvent utilization, architectural coatings, chemical manufacturing, and exhaust and evaporation from cars.

2.3 The Planetary Boundary Layer

The planetary boundary layer (PBL) describes the lowest layer of the atmosphere affected by the surface (Figure 2.2). Flow in the PBL is turbulent and in fair weather has a distinct diurnal variation driven by solar radiation. Above the PBL is the free troposphere where winds are approximately geostrophic and laminar.

The lowest layer of the PBL, which is affected by the no slip condition at the surface, is called the surface layer. The height of the surface layer is approximately 10% of the total PBL height. Radiative cooling at night forms a shallow thermal inversion above the surface layer called the nocturnal boundary layer (usually $\sim$200 m above ground level, AGL). The layer of air above the nocturnal boundary layer is called the residual layer. At sunrise, thermal fluctuations mix air from the residual layer with air trapped below the nocturnal inversion.

During the daytime, the PBL is capped by a nocturnal or subsidence temperature inversion 1-2 km AGL. Subsidence inversions are usually associated with high-pressure systems where air aloft sinks gradually and is warmed adiabatically. The base of cumulus convective clouds can also mark the height of the boundary layer. Cumulus convective clouds form when water vapor condenses in rapidly ris-

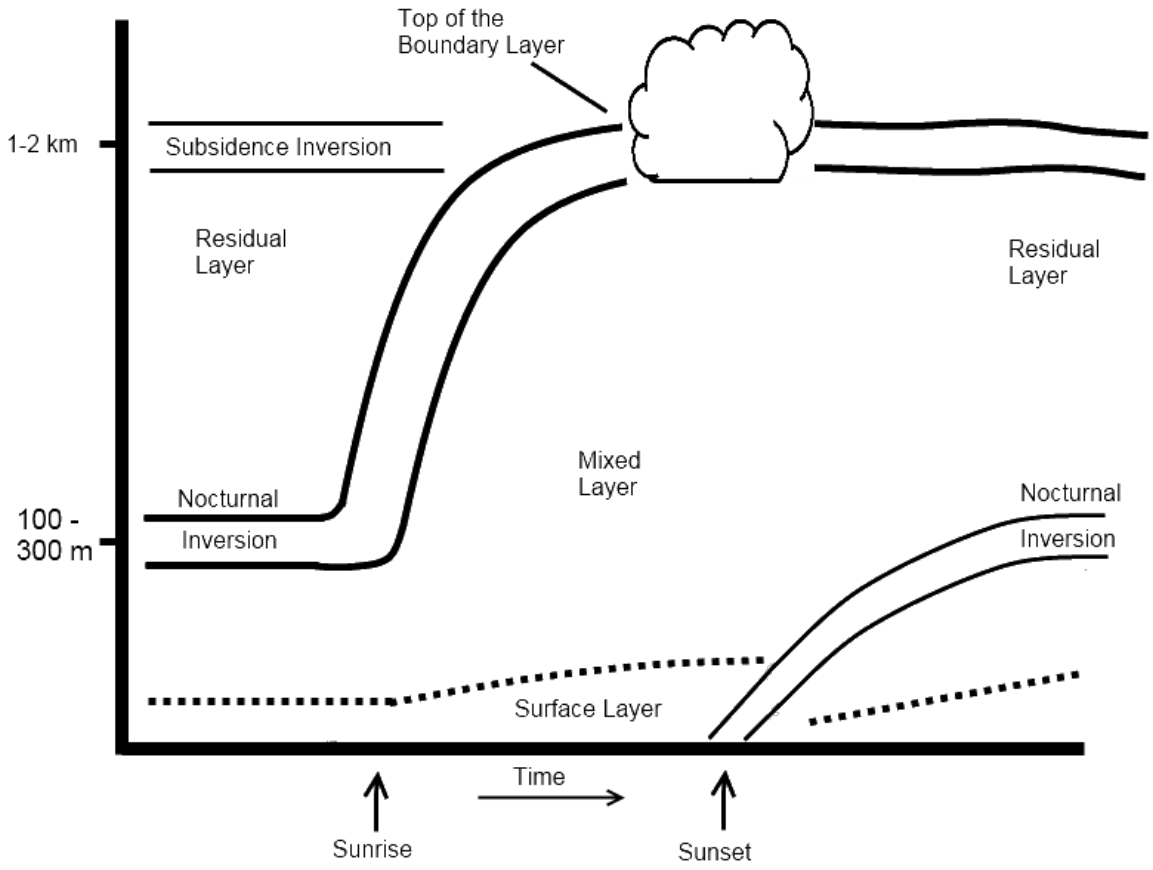

Figure 2.2: Diagram of the diurnal variation of the planetary boundary layer.

ing air that expands adiabatically. Deep updrafts that continue through the cloud base as a result of warming from the latent heat of condensation can transport pollutants from the boundary layer into the free troposphere. Because convective thermals and mechanical turbulence cause the air between the surface layer and the boundary layer to be well mixed, this area is called the mixed layer. At sunset the mixed layer collapses, leaving air from the mixed layer trapped in the residual layer where it can be transported long distances on the prevailing winds unaffected by the surface.

2.4 Meteorological Conditions Associated with Ozone

When pollutants present in the daytime mixed layer are trapped in the residual layer, they can be transported long distances on the prevailing winds unaffected by surface removal processes, increasing the lifetime of ozone and its precursors, which are generally short lived. In the morning when the surface begins to warm, convective thermals break up the nocturnal boundary layer and the transported pollutants are mixed down with the local pollution. This morning injection of ozone and precursors plays a significant role in causing high surface ozone concentrations later in the day, and makes ozone a regional pollutant that is a function of a mixture of local and regional precursor sources (Baumann, et al., 2000, Schichtel and Husar, 2001, Vukovich and Scarborough, 2005). Because of they emit at high altitudes, upwind industrial sources located in the Ohio River Valley (where many of the regions largest power plants are located) emit into the residual layer. Consequently, they have the potential to directly affect air quality in the Northeastern U.S.

Given that ozone is driven by photochemistry, high temperatures and clear skies are generally associated with high ozone concentrations (Jacob, 1999, Vukovich and Sherwell, 2003, U.S. Environmental Protection Agency (USEPA), 2006, Bloomer, et al., 2009). In the Mid-Atlantic, high pressure systems located to the West or Northwest are correlated with multi-day high ozone events (Vukovich, 1994, Ryan, et al., 1998, Kleinman, et al., 2004, Taubman, et al., 2004). This synoptic condition inhibits cloud formation and leads to subsidence, which causes stagnant conditions and a low level inversion that allows pollutants to accumulate at the surface (Figure

2.2). High-pressure systems to the West or Northwest are also conducive to westerly transport of pollutants from the Ohio River Valley to the Northeast.

2.5 Air Quality Models

Air quality models (AQMs) that simulate chemistry, transport and diffusion, and atmospheric removal processes of multiple pollutants including trace gases and aerosols, are important tools for studying ozone. They are used for decision support, regulatory attainment analysis, creation of emissions control strategies, analysis of regional atmospheric chemistry and transport, and for basic insight into the chemistry and physics of the atmosphere.

Government agencies and university scientists have developed a system of models to create realistic simulations of emissions, meteorology, and atmospheric chemistry and transport. The models used in this study are the Sparse Matrix Operator Kernel Emissions (SMOKE) model (UNC, 2008), the Mesoscale Model 5 (MM5) (Grell, et al., 1994), and the Community Multiscale Air Quality (CMAQ) model (Byun and Schere, 2006). Together these models comprise the EPA Models3 system that provides the initial conditions, boundary conditions, chemical reactivity, and transport parameters needed to solve an atmospheric chemistry and diffusion problem (Figure 2.3).

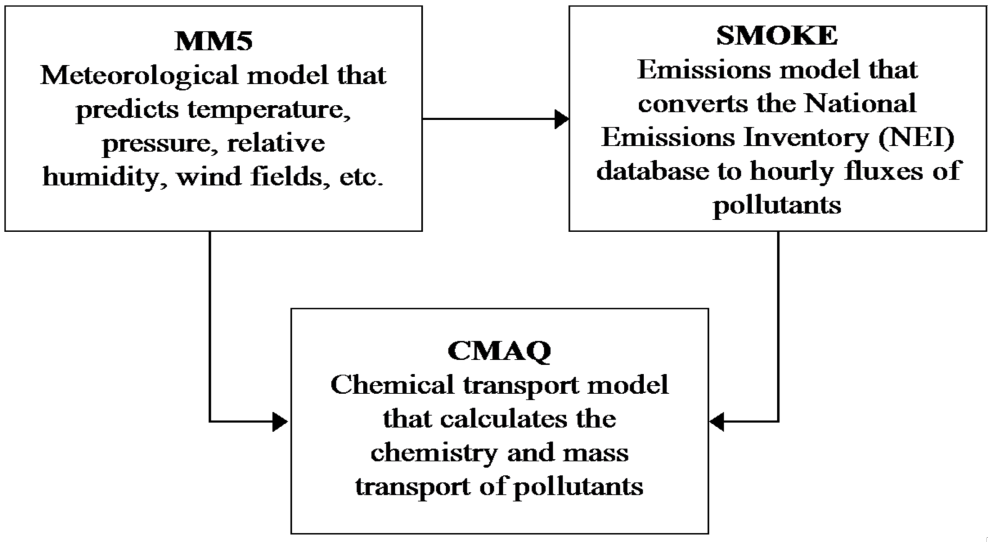

Figure 2.3: Flow diagram of the EPA Models3 modeling system. The outputs of the SMOKE and MM5 models are used as inputs to CMAQ. Some MM5 outputs are used in SMOKE processing of biogenic, mobile, and point source emissions, which are a function of atmospheric dynamics.

2.5.1 Emissions Modeling: Primary Pollutants, Emissions Inventories, and SMOKE

The EPA requires every state to keep a database of CO, NO_X, SO_2, VOC, NH_3, PM2.5 (particles less than 2.5 μm in diameter), and PM10 (particles less than 10 μm in diameter) emissions from various types of sources because these pollutants play a direct role in the formation of ozone and atmospheric aerosols, and are regulated by primary health standards. The state-level databases are combined and formatted to produce the National Emissions Inventory (NEI). The NEI is split into five emissions sectors: area, point, non-road mobile, on-road mobile, and biogenic according to source characteristics. Area sources are surface-level emitters that cover a broad area, such as solvent utilization, crop and livestock production, landfills and incinerators, and residential fuel combustion. Point sources are large, individual surface level or elevated emitters. Typically emissions from power plants and chemical, food, mineral, wood, and plastic production belong to this sector. Non-road mobile sources are similar to area sources in that they are broad surface-level emissions, but they are comprised exclusively of exhaust from hydrocarbon combustion by internal combustion engines and evaporative emissions. Examples of non-road mobile sources are off-highway vehicles (recreational, agricultural, and commercial), aircrafts, railways, and recreational and commercial boating and shipping.

On-road mobile sources differ from non-road sources in the way they are reported and spatially allocated. On-road sources are a combination of area and line sources because the emissions are distributed in order to follow roadways. The data

are reported as vehicle miles traveled (VMT), not yearly emissions in tons like the other sectors. Emissions are calculated within EPA's Mobile6 model using a special emissions factor that takes into account speed, road class, fleet data, surface temperature, pressure, and relative humidity.

Emissions factors for Mobile6 are developed through laboratory exhaust studies like the Federal Test Procedure, dynamometer tests, and the idle test, as well as data from inspection and maintenance programs. As a result of the inherent limitations of laboratory testing, the Mobile6 emissions factors may not represent real world driving behavior and vehicle maintenance (Bishop and Stedman, 1996). Comparisons of Mobile6 emissions factors to fuel-based emissions inventories and roadside remote sensing of motor vehicle exhaust have found that CO emissions factors may be overestimated by 50% for gasoline powered vehicles, and underestimated by 50% for diesel vehicles. Emissions factors of NO may be overestimated by 50% for vehicles older than 7 years (Kuhns, et al., 2004, Pollack, et al., 2004, Parrish, 2006). These uncertainties must be taken into account when analyzing model results in areas affected by motor vehicles emissions.

The biogenic portion of the emissions inventory takes into account the release of CO, NO, and VOCs from crops, plants, trees, and soil. Emissions from biogenic sources make up more than half of the total national VOC emissions. The Biogenic Emissions Inventory System (BEIS) 3.12 developed by EPA uses gridded fractional land use data, surface temperature, pressure, radiation, and rainfall to calculate emissions factors from these sources. Like area sources, these are surface level emissions that cover a broad area.

(a)	CO	NO_X	SO_2	VOC	NH_3	PM10	PM2.5
Area	$1.8x10^{10}$	$1.3x10^{9}$	$9.0x10^{8}$	$1.0x10^{10}$	$3.4x10^{9}$	$1.7x10^{10}$	$3.0x10^{9}$
Point	$3.2x10^{9}$	$6.5x10^{9}$	$1.2x10^{10}$	$9.9x10^{8}$	$6.6x10^{7}$	$9.8x10^{8}$	$7.1x10^{8}$
Onroad Mobile	$5.7x10^{10}$	$7.4x10^{9}$	$2.3x10^{8}$	$4.2x10^{9}$	$2.6x10^{8}$	$1.8x10^{8}$	$1.3x10^{8}$
Nonroad Mobile	$2.0x10^{10}$	$4.1x10^{9}$	$4.7x10^{8}$	$2.4x10^{9}$	1.3x107	$3.0x10^{8}$	$2.7x10^{8}$
Biogenic	$5.3x10^{9}$	$9.6x10^{8}$		$4.4x10^{10}$			
National Total	$1.0x10^{11}$	$2.0x10^{10}$	$1.3x10^{10}$	$6.2x10^{10}$	$3.7x10^{9}$	$1.9x10^{10}$	$4.1x10^{9}$

(b)	CO	NO_X	SO_2	VOC	NH_3	PM10	PM2.5
Area	$1.7x10^{9}$	$2.8x10^{8}$	$3.0x10^{8}$	$1.5x10^{9}$	$2.7x10^{8}$	$8.2x10^{8}$	$2.7x10^{8}$
Point	$34.7x10^{8}$	$7.4x10^{8}$	$2.0x10^{9}$	$1.3x10^{8}$	$8.5x10^{6}$	$9.5x10^{7}$	6.1x107
Onroad Mobile	$1.2x10^{10}$	$1.4x10^{9}$	$4.2x10^{7}$	$9.1x10^{8}$	$5.5x10^{7}$	$3.2x10^{7}$	$2.2x10^{7}$
Nonroad Mobile	$4.2x10^{9}$	$4.4x10^{8}$	$6.0x10^{7}$	$5.7x10^{8}$	$3.0x10^{5}$	$4.4x10^{7}$	$4.0x10^{7}$
Biogenic	$3.2x10^{8}$	$3.1x10^{7}$		$4.3x10^{9}$			
Northeast Total	$1.4x10^{10}$	$2.5x10^{9}$	$2.4x10^{9}$	$6.9x10^{9}$	$3.3x10^{8}$	$9.9x10^{8}$	$4.0x10^{8}$

Table 2.1: 2002 National (a) and Northeast (b) emissions by category in kilograms per year.

Table 2.1 and Figure 2.4 show the absolute and relative contributions of the five sectors of emissions to the 2002 NEI and to the total emissions in the Northeast region (comprised of Maryland, Delaware, District of Columbia, New Jersey, New York, Connecticut, Maine, Rhode Island, New Hampshire, Massachusetts, Pennsylvania, Virginia, and Vermont). On-road mobile sources are the dominant NO_X and CO emitters. Point sources are the second largest source of NO_X and are the only significant source of SO_2. In the Northeast, VOC emissions are roughly 60% biogenic, while nationally, biogenic emissions make up 70% of the total. Area and mobile sources contribute the greatest to the anthropogenic portion of VOCs. Area sources also dominate NH_3, PM2.5, and PM10 emissions.

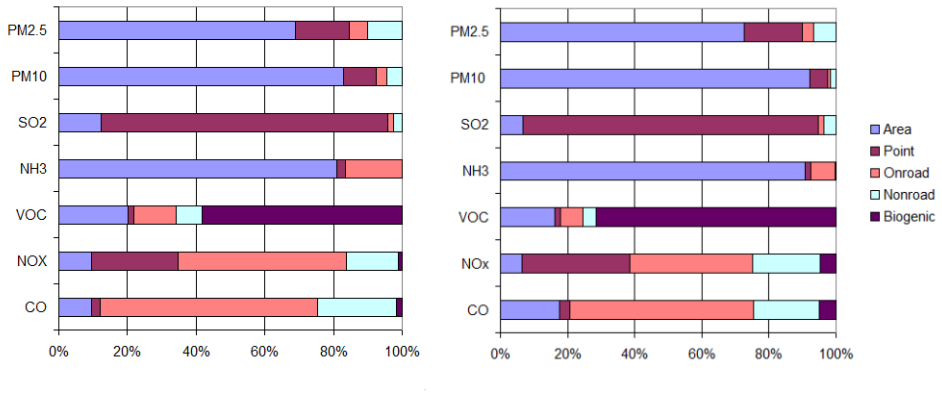

Figure 2.4: Relative contributions of the five source categories to the 2002 National Emissions Inventory (right) and 2002 Emisisons in the Northeast (left).

SMOKE is an emissions model developed by the EPA that converts aggregated yearly emissions estimates reported in the NEI into arrays that are more readily used by chemical transport models (CTMs). The EPA, in conjunction with regional air planning groups, utilizes consumer use, economic, and census information to calculate emissions of primary pollutants on a national, state, and county level. This is called the "bottom up" approach to emissions inventory development. Likewise, detailed chemical mechanisms in a CTM require gridded and hourly emissions flux fields of many compounds as inputs. Emissions models are the link between the aggregated inventories and CTMs.

In order to perform the inventory-to-array calculation, SMOKE requires several inputs that describe the spatial, temporal, and chemical nature of an emissions source. Because the exact hourly emission of every source at every location is not

known representative spatial surrogates and temporal profiles are used. A spatial surrogate, for example, describes how the emissions should be divided up among the grid cells intersecting the county where a source is located. The surrogates obtained from a temporal profile are used to calculate how emissions are distributed by month, day of week, and hour of day. By creating cross-reference files that link together sources with similar spatial, temporal, and speciation surrogates, SMOKE can efficiently calculate gridded hourly arrays using sparse matrix algebra.

2.5.2 Meteorological Modeling: MM5

MM5 is a fifth generation mesoscale and regional scale atmospheric circulation model developed by Pennsylvania State University and the National Center for Atmospheric Research (NCAR) (Grell, et al., 1994). It is used to derive meteorological inputs for emissions and chemical transport models. The CTMs use temperature, pressure, wind and other parameters derived by MM5 as inputs to the transport, photochemical, and thermodynamic equations. SMOKE uses these data in the calculations for temperature-sensitive emissions, such as evaporation from vehicles and biogenic emissions.

MM5 can be run in hydrostatic or nonhydrostatic mode and uses a terrain following sigma coordinate for the vertical. Model predictions are nudged back to National Weather Service surface and rawinsonde observations over the domain using four dimensional data assimilation. MM5 calculates wind speeds, temperature, pressure, relative humidity, planetary boundary layer (PBL) height, and radiation.

MM5 also provides land use, surface roughness, surface wetness, and leaf area index data required for the dry deposition algorithms. In this work, year-long meteorological simulations conducted by Prof. Da-Lin Zhang, Department of Atmospheric and Oceanic Science, with MM5 were used (Zhang and Zheng, 2004).

2.5.3 Meteorology-Chemistry Interface Processor (MCIP)

The Meteorology-Chemistry Interface Processor (MCIP) is a processor program used to convert MM5 outputs into a format usable by CMAQ, and to calculate species-specific depositions velocities. The MCIP dry deposition scheme M3Dry models deposition velocity (Vd, ms^{-1}) as the inverse sum of a series of resistances in units of sm^{-1}: R_a (aerodynamic resistance), R_b (sublayer resistance), and R_s (surface resistance).

$$N_i = V_{d,i} C_i \tag{2.16}$$

$$V_{d,i} = \frac{1}{R_a + R_b + R_s} \tag{2.17}$$

where N_i is the surface flux, and C_i is the gas concentration at some reference height.

The surface layer resistance depends on the physical, chemical, and biological interactions with the ground and/or vegetation. The sublayer resistance is the resistance to molecular diffusion and depends on the gas diffusion coefficient and air temperature, pressure, and viscosity. The aerodynamic resistance is a property of turbulent transfer from the reference height to the sublayer and depends on atmospheric stability.

2.5.4 Chemical Transport Modeling: CMAQ

The underlying function of a CTM is to solve the species conservation equation describing formation, transport, and removal of pollutants

$$\frac{\partial c_i}{\partial t} + \nabla \cdot \bar{U} c_i = \nabla \rho D_i \nabla \frac{c_i}{\rho} + R_i(c_1, c_2, ...c_n, T, t) + S_i(\bar{x}, t) \tag{2.18}$$

where c_i, D_i, R_i, and S_i are the concentration, diffusivity, reaction rate, and sources or sinks at position of species respectively. $\bar{U}$ is the mean wind velocity, and ρ is the density of air. This set of coupled nonlinear differential equations is impossible to solve analytically for a full domain. Therefore, in Eulerian models, like CMAQ, the approach is to divide the modeling domain horizontally and vertically into grid boxes, which interact with each other. Within each box a finite approximation to the species conservation equation is solved. One method used to solve the governing equations is the operator splitting technique. The idea is to break the equation down into the various transport processes and solve the pieces independently. Thus the species conservation equation takes on the following form:

$$\frac{\partial c_i}{\partial t} = \left(\frac{\partial c_i}{\partial t}\right)_{HADV} + \left(\frac{\partial c_i}{\partial t}\right)_{VADV} + \left(\frac{\partial c_i}{\partial t}\right)_{S} \tag{2.19}$$

$$\left(\frac{\partial c_i}{\partial t}\right)_{HADV} = \nabla_H \rho D_i \nabla_H \frac{c_i}{\rho} - \nabla_H \cdot \bar{U} c_i \tag{2.20}$$

$$\left(\frac{\partial c_i}{\partial t}\right)_{VADV} = \frac{\partial}{\partial z} \rho D_i \frac{\partial c_i/\rho}{\partial x} - \frac{\partial w c_i}{\partial z} \tag{2.21}$$

$$\left(\frac{\partial c_i}{\partial t}\right)_{S} = R_i(c_1, c_2, ...c_n, T, t) + S(i) \tag{2.22}$$

where the total rate of change of c_i is equal to the sum of the changes due to horizontal advection, vertical advection, as well as sources (emissions) and sinks

such as cloud processes, wet deposition, dry deposition, and aerosol processes (gas to particle transition). This is more efficient and accurate because specific numerical algorithms can be used on each part.

For aerosols the formation and growth of particles must be solved for in the aerosol general dynamic equation (GDE):

$$\frac{\partial n}{\partial t} + \nabla \cdot \bar{U} n + \frac{\partial I}{\partial v} = \frac{1}{2} \int_0^v \beta(\bar{v}, v - \bar{v}) n(\bar{v}) n(v - \bar{v}) d\bar{v} + \int_0^\infty \beta(\bar{v}, v) n(\bar{v}) n(v) d\bar{v} + \nabla \cdot C n \tag{2.23}$$

where n is the particle size distribution function, I describes particle growth and nucleation due to gas to particle conversion, v is particle volume, β describes particle coagulation, and C is sedimentation velocity (Friedlander, 2000). Because solving the full GDE is computationally intensive, CMAQ uses a modal approach to characterize the aerosol size distribution. Aerosols are divided into fine and coarse mode particles, which have bimodal and unimodal lognormal size distributions, respectively. Furthermore, the model assumes that fine and coarse particles do not interact, and fine particles are in thermodynamic equilibrium with the gas phase. The size distribution of fine particles is effected by coagulation between particles, condensation, new particle formation from the vapor phase, transport, and direct emissions of new particles. The other major aerosol processes are size dependent dry deposition, wet deposition, and aerosol-cloud droplet interaction (Byun and Schere, 2006, Levy, 2007).

AQMs use chemical reaction mechanisms to parameterize atmospheric chemical processes such that most compounds and reactions are included while maintain-

ing computational efficiency. In general, chemical mechanisms group species into chemical classes and collapse fast multi-step reactions into a single step.

Most atmospheric chemical mechanisms represent atmospheric inorganic chemistry explicitly, but differ in the parameterization of organic molecules. The two main organic molecule parameterizations are: 1) the lumped molecule approach that represents similar organic species with a particular or generalized species, and 2) the lumped structure approach where organic molecules are represented as a collection of functional groups. For example, in the lumped molecule approach, all mono-substituted aromatic compounds are represented by one species. In the lumped structure approach, four single-bonded one-carbon-atom surrogates represent n-butane. The most commonly used lumped molecule mechanism is the [California] Statewide Air Pollution Research Center (SAPRC) mechanism (Carter 1990). The other most commonly used chemical mechanism is the Carbon Bond (CB) mechanism (Gery, et al., 1989), which uses both the lumped structure and lumped molecule approaches. The two mechanisms are consistently updated to incorporate new experimental findings. The versions of SAPRC and CB discussed here are SAPRC99 and CB-IV.

In general, the two mechanisms agree to within 10% for predictions of ozone in urban areas even though SAPRC99 has three times more organic species than CB-IV (Faraji, et al., 2008). However, at high VOC to NO_X ratios, SAPRC99 consistently predicts higher ozone concentrations. The main differences between the two mechanisms that lead to higher ozone in SAPRCC99 are: 1) The ring opening products of mono-substituted aromatics in SAPRC99 are more reactive than those

of CB-IV. 2) The balance of radical production and termination in SAPRC99 leads to higher radical concentrations than CB-IV. 3) The production of high molecular weight aldehydes is greater in the SAPRC99 mechanism than in the CB-IV mechanism as a result of a more detailed representation of aldehydes in SAPRC99.

Another significant difference between CB-IV and SAPRCC99 is the mechanisms' treatment of organic nitrate. The minor (4-14%) reaction product for 2.6 is a stable organic nitrate, $RONO_2$ (2.24) (Chen, et al., 1998, Sprengnether, et al., 2002, Patchen, et al., 2007). R equal to isoprene is the main organic precursor in the Eastern U.S. (Perring, et al., 2009).

$$RO_2 \cdot + NO \rightarrow RONO_2 \tag{2.24}$$

Formation of organic nitrates is a way of sequestering, recycling, and eliminating ($RONO_2$ dry deposits quickly, and can photolyze, be rained out, and become incorporated into aerosols) NO_X that is not well understood, and is still a subject of active research (Horowitz, et al., 2007, Ito, et al., 2009). The yields of R1-16 and the photolysis rates and oxidation products of $RONO_2$, which produce NO_X, are highly uncertain (Perring, et al., 2009). Because organic nitrates could have a high but uncertain NO_X recycling efficiency, they may also play a role in the fate of NO_X over multiple days. Observations have shown that organic nitrates can have as much as a 10% effect on ozone, and affects how ozone responds to changes in isoprene emissions (Wu, et al., 2007). The SAPRC and CB-IV mechanisms both include pathways for organic nitrate formation. However, only SAPRC includes $RONO_2$ photolysis to recycle NO_2. Neither mechanism takes into account organic

nitrate oxidation.

The CB-IV mechanism was used in this work to remain consistent with and be able to compare to previous state regulatory modeling without the ambiguity of two different chemical mechanisms. A brief description of the details of the CB-IV mechanism follows.

The CB-IV mechanism used in CMAQ has 46 species and 96 gas-phase, aerosol, and aqueous reactions. The mechanism considers three types of species groups: 1) organics that are chemically unique or significant in the atmosphere such as PAN, isoprene, and formaldehyde, 2) organic species represented by a combination of chemical surrogates, and 3) inorganic species. The inorganic reactions for ozone, NO_X, and HO_X are treated explicitly in the model. The other chemical surrogates are 1) OLE, used to represent carbon-carbon double bonds; 2) ALD2, used in place of the C-CHO group found in aldehydes; 3) TOL, a monoalkyl benzene structure, and 4) XYL, used for diaklyl and trialkyl benzene structures (Gery, et al., 1989).

2.5.5 Air Quality Monitoring

Under the provisions of the Clean Air Act, the EPA is required to monitor pollutant concentrations that are regulated by primary health standards. The Air Quality System (AQS), a network of air pollution monitors across the U.S., was put in place to monitor the state and progress of CO, O_3, NO_2, SO_2, PM10, PM2.5, and lead ambient concentrations. AQS sites also collect meteorological data, and some sites measure other ozone precursors as well. The AQS is the largest of the

monitoring networks with thousands of sites, and is used to designate attainment status with respect to current regulations, and to make recommendations for future regulations.

Photochemical Assessment Monitoring Stations (PAMS) are more comprehensive ozone monitoring sites, and are located in and around areas with persistent high ozone (mostly large cities). These sites monitor ozone, NO_X, and an extensive number of VOCs. Usually several PAMS sites are located in and around a city in order to characterize the local and regional properties of air pollution, and guide effective remediation. One site is placed upwind to establish a background. A second site is placed within the area of maximum emissions to monitor the types of precursors and their magnitudes. Two more sites are placed downwind to monitor the effects of the precursors, and pollutants that are transported from the area. Areas that are subject to PAMS monitoring in the Eastern U. S. are Milwaukee, Chicago, Atlanta, Baltimore, Washington, Philadelphia, New York, Springfield, Providence, Boston, and Portsmouth.

The Clean Air Status and Trends Network (CASTNET) monitors acid deposition and rural levels of ozone. Ambient concentrations and estimates of the deposition velocity and flux of O_3, SO_2, and HNO_3 are reported. This network has some of the longest continuously running air quality monitoring sites (15 years), and is a valuable tool for analyzing trends in ambient pollutant concentrations, and the effectiveness of emissions controls. There are 86 sites located in or near rural areas and sensitive ecosystems. Detailed descriptions of AQS, PAMS, and CASTNET sites can be found at http://www.epa.gov/ttn/airs/airsaqs/, http://www.epa.gov/oar/oaqps/pams/,

and http://www.epa.gov/castnet/site.html, respectively.

Data from the AQS, PAMS, and CASTNET sites are a valuable tool for model development and performance evaluations, as well as analyzing ambient trends. These networks only provide surface level information. Vertical profiles of pollutant concentrations are essential for evaluating long-range transport and vertical mixing in air quality models. The total mass of pollutants in the lower troposphere, used to evaluate emissions inventories, can also be calculated from vertical profiles.

Satellite remote sensing of trace gas concentrations can provide vertical profile and total column data over a large geographical area, but the data are still uncertain in the lower troposphere. Satellite data are also only available on a one snapshot per day basis, and are subject to interference from clouds.

Observations taken from an aircraft are a means of obtaining pollutant vertical profiles in the lowest layers of the atmosphere at a high temporal resolution. However, in contrast with satellite data, an aircraft vertical profile is only representative of a specific location. Because of the expense, aircraft observations are usually limited to intensive field campaigns.

The Regional Atmospheric Measurement, Modeling and Prediction Program (RAMMPP) is an on-going aircraft observation and air quality modeling program at the University of Maryland where O_3, SO_2, CO, and size distribution, number concentrations and optical properties of particles are measured in and around the Northeast U.S. Typically, observations are taken on days when high ozone concentrations are forecasted. The flight plans are designed such that in the morning vertical profiles are measured mostly upwind of major cities, and in the afternoon

the vertical profiles are measured downwind of major cities. Thus it is possible to analyze the transport of pollutants into the region, and the effects of pollutants generated within the region. This dataset is useful for analyzing model performance and the nature of the ozone problem in the Northeast.

2.6 AQM Sensitivity to Temporal Distribution of Emissions

Although in many instances AQMs satisfactorily replicate ozone when compared to surface observations the simulations are subject to uncertainty resulting from parameterizations and approximations embedded in the model algorithms and chemical mechanisms, as well as inaccuracies in the meteorological and emissions inputs (Hanna, et al., 1998, Placet, et al., 2000, Bey, et al., 2001, Fine, et al., 2003, Brunner, et al., 2005, Arnold and Dennis, 2006, Eder and Yu, 2006, Mallet and Sportisse, 2006, Appel, et al., 2007, Gego, et al., 2008, Godowitch, et al., 2008). Models sometimes obtain the right ozone concentration for the wrong reasons.

Specifically, emissions inventories, reported as annual or daily average values, must be broken up into the hourly fluxes required by AQMs using generalized temporal distributions. The resulting estimates of hourly emissions that are AQM inputs are less variable than corresponding measurements from continuous emissions monitors (CEM) and field campaigns would imply (Placet, et al., 2000, Hanna, et al., 1998, Marr, et al., 2002, Murphy and Allen, 2005). Before going to the expense of creating inventories that represent real world variability, we would like to know how sensitive the model is to the temporal variability of emissions.

In Chapter 3, I will analyze the sensitivity of the Community Multiscale Air Quality Model (CMAQ) to altered temporal distributions of emissions, focusing on the Eastern U.S. and using a 12 km grid to capture urban effects. The results, which have been presented in Castellanos et al. (2009a), will show the model's response to changing the temporal distribution individually of the four major source categories of anthropogenic emissions (area, point, on-road mobile, and non-road mobile sources) as an initial look at the sensitivity in the model to similar emissions sources.

2.7 CMAQ Model Performance of CO

CO is an ideal tracer for analyzing pollutant transport in AQMs because the atmospheric lifetime, on the order of weeks, is longer than the timescale of boundary layer mixing. The atmospheric chemistry of CO is well known and implemented in the model in a straightforward manner. However, the sources and sinks of CO are less certain. Thus, an evaluation of CO in CMAQ is needed in order to use the model as a tool for investigating the role of pollutant transport in ozone formation.

The precision of surface CO monitoring in the national monitoring networks is generally low; often only one significant figure is reported. Datasets from intensive field campaigns or select research surface sites must be used to evaluate CO model performance. In Chapter 4, I will compare CMAQ to CO vertical profiles taken at various locations throughout the Northeast by the Regional Atmospheric Measurement, Modeling and Prediction Program (RAMMPP), and high precision surface observations at select monitoring sites.

2.8 Analysis of Vertical Turbulent Mixing in CMAQ

Capturing the morning buildup of pollutants in the shallow nocturnal boundary layer is important for replicating the morning burst of ozone and nighttime surface removal processes. Model performance studies have shown that CMAQ consistently over predicts the nighttime/early morning ozone minimum (e.g. Appel, et al., 2007). At night and in the early morning, the dominant vertical dynamical mechanism is turbulent mixing. If this mixing process occurs too quickly, NO_X concentrations will be diluted at the surface. This inhibits the loss of ozone, which occurs through titration with NO.

In CMAQ, K-theory is used to represent vertical turbulent mixing in the surface layer and the mixed layer. K-theory models turbulent transport with an eddy diffusion coefficient (K_Z, m^2/s), analogous to molecular diffusivity.

$$\left.\frac{\partial c_i}{\partial t}\right|_{VDIFF} = \frac{\partial}{\partial z} K_z \frac{\partial c_i}{\partial z} \tag{2.25}$$

K_Z is calculated using PBL similarity theory based on the formulations in Businger (1971) and Hass (1991). However, a minimum K_Z is established in CMAQ, which artificially increases mixing, especially in the stable nocturnal boundary layer. In Chapter 5, I will present improvements in the model performance of CMAQ from adjusting the minimum K_Z from 0.5 m^2/s (currently implemented in CMAQ), to 0.1 m^2/s, a value more consistent with observations (Wesely, et al., 1985, Gallagher, et al., 2002 and references therein, Constant, et al., 2008).

2.9 Measurement of NO_2 Using Cavity Ring-Down Spectroscopy

In polluted atmospheres where high ozone concentrations are a problem, monitoring of NO_2 is necessary to understand the effects of control strategies, to monitor progress for compliance with standards, understand the formation and loss of ozone, and for model validation.

A variety of methods exist for measuring NO_2, ranging from relatively inexpensive off-the-shelf commercial analyzers to research grade, highly sensitive techniques. In the AQS monitoring network, NO_2 observations for compliance with EPA's NO_2 NAAQS is usually accomplished with reduction of NO_2 to NO followed by reaction with ozone and chemiluminescence (EPA, 2006); the concentration of NO_2 is determined from the difference between NO_X (the sum of NO and NO_2) and NO measured directly. The most common method for conversion of NO_2 to NO, (passage over 375°C Mo) also converts a variety of other species (including peroxy acetyl nitrate and HNO_3) to NO. While this technique is adequate for demonstrating compliance with the NO_2 standard, it can overestimate NO_2 substantially.

In light of new findings linking respiratory illnesses with short-term exposure to high NO_2 concentrations, the EPA has proposed tougher NO_2 standards and a comprehensive NO_2 monitoring system near roadways, where the highest levels of NO_2 are often found. To meet the monitoring demands put forth by this new legislation and to address the various scientific needs previously discussed, a specific, reliable, fast, economical method for monitoring NO_2 in rural and urban environments will be needed. In Chapter 5, I will present results, which have appeared in

Castellanos, et al. (2009b), from the implementation of a new technique to measure ambient NO_2 in a polluted environment with Cavity Ring-Down Spectroscopy (CRDS).

Chapter 3

Sensitivity to Temporal Distribution of Emissions

3.1 Introduction

Although in many instances AQMs satisfactorily replicate ozone when compared to surface observations the simulations are subject to uncertainty resulting from parameterizations and approximations embedded in the model algorithms and chemical mechanisms, as well as inaccuracies in the meteorological and emissions inputs (Hanna, et al., 1998, Placet, et al., 2000, Bey, et al., 2001, Fine, et al., 2003, Brunner, et al., 2005, Arnold and Dennis, 2006, Eder and Yu, 2006, Mallet and Sportisse, 2006, Appel, et al., 2007, Gego, et al., 2008, Godowitch, et al., 2008).

Specifically, emissions inventories, reported as annual or daily average values, must be broken up into the hourly fluxes required by AQMs using generalized temporal distributions. The resulting estimate of hourly emissions that are AQM inputs are less variable than corresponding measurements from continuous emissions monitors (CEM) and field campaigns would imply (Placet, et al., 2000, Hanna, et al., 1998, Marr, et al., 2002, Murphy and Allen, 2005). Emission rates from peaking units, for instance, are currently not well represented in the model. Before going to the expense of creating inventories that represent real world variability, we would like to know how sensitive the model is to the temporal variability of emissions. This will give us an idea of the magnitude of results to expect from implementing

detailed emissions control strategies that target time of day.

Webster, et al., (2007) created a stochastic emissions inventory of industrial VOC emissions to better represent major emissions events in the Houston-Galveston area. Using a fine grid (1 km) over the Houston-Galveston area, they compared the stochastic inventory to an inventory with constant industrial emissions and found that increased variability created changes in hourly ozone concentration in the range of 10-52 parts per billion by volume (ppbv). Nam, et al. (2008), demonstrated that applying controls to the stochastic emissions inventory is more effective at reducing the highest ozone concentrations than controlling constant emissions.

Tao et al. (2004), compared a simulation with constant anthropogenic emissions (uniform temporal profiles) to a simulation where anthropogenic emissions varied according to temporal profiles included in the National Emissions Inventory (NEI). They found that, when uniform temporal profiles are used on a regional scale (with 90 km resolution), the change in the weeklong average hourly ozone concentration from the time-varying emissions case over the U.S. was small during the day. Regression and frequency distribution analysis showed that the two simulations agreed well for higher ozone concentrations, but not for lower ozone concentrations. While altering all anthropogenic emissions is warranted for analyzing the overall usefulness of an inventory, this does not result in information helpful for developing emissions control strategies. Rarely are controls applied to every category of emissions. Instead regulators begin by analyzing source categories that have similar properties and then work down to specific industries or polluting processes.

In this chapter I will further analyze the sensitivity of the Community Mul-

tiscale Air Quality Model (CMAQ) to altered temporal distributions of emissions, focusing on the Eastern U.S. and using a 12 km grid to capture urban effects. The results, which have been presented in Castellanos, et al. (2009a), will show the model's response to changing the temporal distribution individually of the four major source categories of anthropogenic emissions (area, point, on-road mobile, and non-road mobile sources) as an initial look at the sensitivity in the model to similar emissions sources.

3.2 Emissions Scenarios

We modeled three daily temporal profiles of emissions from area, point, on-road mobile (referred to as mobile), and non-road mobile (referred to as non-road) sources: a "uniform" temporal profile in which the emissions were the same from hour to hour, a "base" temporal profile, which utilized the temporal distribution provided in the inventories, and an "increased variability" temporal profile in which 50% of nighttime emissions were added to the daytime in order to increase the relative peak during the day and the magnitude of the daily fluctuation in emissions. The uniform and increased variability scenarios were chosen to test the limits of the models sensitivity, and are not meant to represent realistic control strategies. Biogenic emissions were not altered because known sensitivities to temperature, radiation, and relative humidity drive the diurnal variation. In total, nine simulations were conducted with different combinations of source group temporal profiles listed in Table 3.1 The emissions in each grid cell at any hour may be different in each

Run Name	Run Code	Area Temporal Profile	Point Temporal Profile	Non-road Temporal Profile	Mobile Temporal Profile
Base Case	BC	Base	Base	Base	Base
Area Uniform	AU	Uniform	Base	Base	Base
Point Uniform	PU	Base	Uniform	Base	Base
Non-road Uniform	NU	Base	Base	Uniform	Base
Mobile Uniform	MU	Base	Base	Base	Uniform
Area Increased Variability	AI	Increased Variability	Base	Base	Base
Point Increased Variability	PI	Base	Increased Variability	Base	Base
Non-road Increased Variability	NI	Base	Base	Increased Variability	Base
Mobile Increased Variability	MI	Base	Base	Base	Increased Variability

Table 3.1: List of simulations and emissions combinations.

simulation, but the total emissions integrated over the length of the simulation remained the same.

A 2002 emissions inventory (EI) provided by the following four regional planning organizations was processed with the Sparse Matrix Operator Kernel Emissions (SMOKE) v2.2 processor (UNC, 2008): (1) Mid-Atlantic/Northeast Visibility Union (MANE-VU), (2) Mid-West Regional Planning Organization (MRPO), (3) Visibility Improvement State and Tribal Association of the Southeast (VISTAS), and (4) Central Regional Air Planning Association (CENRAP). The 2002 EI was developed to support the 8-hour ozone NAAQS attainment demonstration State Implementation Plans (SIP) in the eastern U.S. Details of the inventory and emissions processing can be found in NYSDEC (2006a, 2007) and PECHAN (2006).

3.3 Modeling Domain

The modeling domain had 12 km grid resolution and covered the eastern half of the U.S. It was nested within a 36 km grid that covered the continental U.S. and provided the boundary conditions for the finer grid. The 36 km simulation was conducted only once, with boundary conditions provided by a global simulation with the GEOS-CHEM model (Jacob, 2005). Thus each 12 km simulation had the same boundary conditions. A Lambert Conformal grid projection centered at 40N and 97W with the lower left corner located at 264 km west and 888 km south of the center defined the 12 km grid, which contained 172 x172 grid cells. A terrain following σ coordinate defined 22 layers from the surface to roughly 30 km. The top of the first layer was roughly 20 m from the surface, and the first twelve layers fell within the bottom 1.5 km of the atmosphere.

3.4 Meteorology

The meteorological fields were generated for the domain with the Penn State/NCAR 5^{th} Generation Mesoscale Model 5 (MM5) v3.6 (Grell, et al., 1994) by the University of Maryland in support of the 8-hour ozone SIPs. Details and analysis of the simulation can be found in NYSDEC (2006b). Briefly, MM5 was run using a modified Blackadar planetary boundary layer scheme (Zhang and Zheng, 2004), and K-theory was used to calculate vertical diffusion coefficients. The model predictions were nudged back to National Weather Service observations using four-dimensional data assimilation. The relevant variables were extracted to the domain for use

in the emissions and air quality models with the Meteorology-Chemistry Interface Processor (MCIP) v2.3.

3.5 Modeling

The emissions and meteorology were used as inputs for CMAQ v4.5 (Byun and Schere, 2006). CMAQ, a three-dimensional Eulerian grid model, simulates atmospheric chemistry, aerosol formation and dynamics, transport and diffusion of pollutants, and pollutant removal wet and dry processes. In this implementation, the carbon bond IV (CB-IV) gas-phase chemical mechanism (Gery, et al., 1989) and the AE3/ISOROPPIA aerosol reaction scheme were used along with the Euler backward iterative (EBI) solver. Daily photolysis rate constant lookup tables were generated with the JPROC processor program included in CMAQ. The Piecewise Parabolic Method was used as the horizontal advection algorithm. The simulation began on May 1^{st} with clean initial conditions and ended on September 15^{th}. The seasonal simulation allows us to evaluate the model over different time scales and meteorological conditions (Hogrefe, et al., 2000). The first 15 days were taken as spin up, and not used in the analysis.

3.6 Observational Data and Model Performance Evaluation

A model performance evaluation was carried out on the base case simulation during the 8-hour NAAQS attainment demonstration SIP using a comprehensive set of measurements at the surface and aloft. Details of the assessment and a list

of the various national and regional measurement networks can be found in NYSDEC (2006c). Simulated concentrations of the following species in Virginia and the Ozone Transport Region (comprised of Connecticut, Delaware, Maine, Maryland, Massachusetts, New Hampshire, New Jersey, New York, Pennsylvania, Rhode Island, Vermont, Northern Virginia, and the District of Columbia) were analyzed: O_3, PM2.5, CO, NO_X, SO_2, and non-methane hydrocarbons, as well as wet deposition rates of SO_4^{2-}, NH_4^+, and NO_3^-. The threshold statistics listed in Table 3.2 suggested by the EPA (USEPA, 1996) for model performance evaluation were calculated for ozone when model and measurement data were paired in time and space (without interpolation). The data from July 6-9 were excluded because the model did not account for long-range transport of pollutants from forest fires in Quebec. A summary of the results from this study and the model performance evaluation conducted by Eder and Yu (2006) for the continental U.S. will be briefly discussed.

2002 base case; Ozone Transport Region	Eder et al. (2006);2001 Continental US
Fractional Error (FE) $\frac{2}{N}\sum\left\lvert\frac{P_i-O_i}{P_i+O_1}\right\rvert \times 100$	Normalized Mean Error (NME) $\frac{\sum\lvert P_i-O_i\rvert}{\sum O_i} \times 100$
Mean Fractionalized Bias (MB) $\frac{2}{N}\sum\left[\frac{P_i-O_i}{P_i+O_1}\right] \times 100$	Normalized Mean Bias (NMB) $\frac{\sum[P_i-O_i]}{\sum O_i} \times 100$

Table 3.2: Model Performance Evaluation Statistics. N is the sample size, O_i is the observed daily maximum 8-hour concentration, and P_i is the predicted daily maximum 8-hour concentration

In the OTR, the fractional error (FE) fell within 9-40% with a median of 15% when observed ozone exceeded 60 ppbv. The range of mean fractionalized bias was -40% to +22% with a median of -12%. Additionally, time series plots show that, on average, modeled and observed ozone values follow the same temporal trend,

except for significant under prediction by the model in August. Also, on average the diurnal variation follows observations, but CMAQ tends to predict the maximum daily ozone concentration one hour earlier than the observed maximum, and over predict ozone at night. Spatially, model performance was better in urban areas and along the Northeast urban corridor than in rural areas.

Eder et al. (2006) evaluated the performance of a previous release of CMAQ (v4.4) over the continental U.S. with the 2001 NEI. Measurement data from four national networks (also used in the analysis discussed in the main text) - the Interagency Monitoring of Protected Visual Environments (IMPROVE) network, Speciation Trends Network (STN), Clean Air Status and Trends Network (CASTNET), and Air Quality System (AQS) - were used in the evaluation of a 36 km resolution yearlong simulation. A correlation of R 0.7 for 1-hr and 8-hour daily maximum ozone was found. In general, the normalized mean bias (NMB) was less than 10%, but in coastal areas NMB values greater than 15% were calculated. Similarly, the normalized mean error was relatively small, less than 20%, on average, but was greater than 40% on the coast.

3.7 Results

3.7.1 Emissions

Typical day (August 21, 2002) domain total hourly NO_X emissions are shown in Figure 3.1 for the nine simulations. In Figure 3.1(a), changing the diurnal variation of mobile sources to uniform (MU) has the greatest change on the domain total

NO_X diurnal variation. MU case nighttime emissions increased by up to 50% and daytime emissions decreased by 10-20%. In the area uniform (AU), point uniform (PU), and non-road uniform (NU) emissions cases NO_X emissions increased by up to 10% at night and decreased by up to 4% during the day. This is expected because mobile source emissions contain the most temporal variability in the NO_X base case inventory (Figure 3.2). In Figure 3.1(b), increasing the temporal variation of point sources (PI) has the greatest change from the base case because point sources make up the largest fraction of the NO_X base case inventory at night (Figure 3.2). The PI case has an up to 25% decrease in NO_X emissions at night, and an up to 13% increase in NO_X emissions during the day. The NO_X emissions in the other three increased variability simulations decrease by up to 8% at night and increase by up to 6% during the day. There is very little change in the domain total VOC emissions' diurnal variation when the temporal variation of the four emissions sectors are altered because biogenic emissions, which were not altered, make up 74% and 84% of the total base case VOC emissions inventory during the nighttime and daytime, respectively (Figure 3.2).

3.7.2 Regional Sensitivities to Uniform Temporal Distributions

Deviations from the base case in the daily 8-hour maximum ozone concentration (8HRMAX) by the AU, PU, MU, and NU simulations are taken to be measures of sensitivity in the model predictions to variations in the temporal distributions of the emissions sectors, assuming that the base case is a best estimate of emissions.

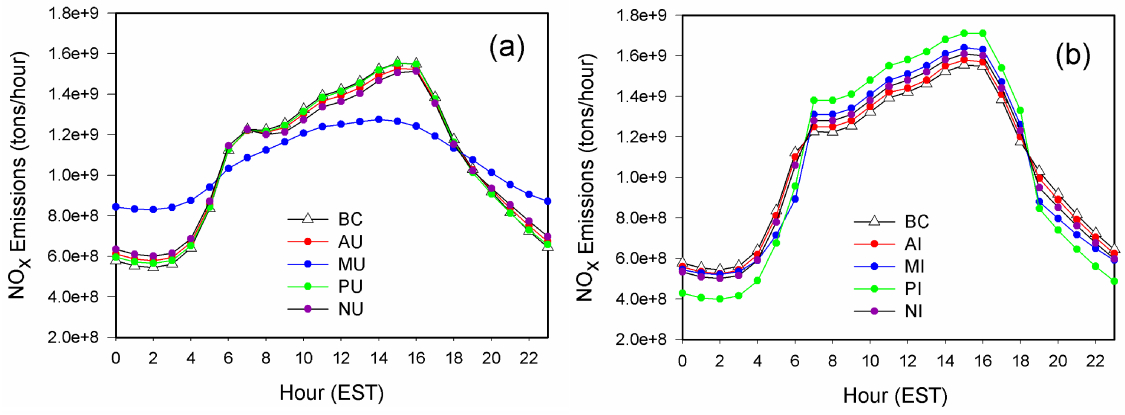

Figure 3.1: The August 21, 2002 domain total hourly NO_X emissions for the (a) Base Case (BC), Area Uniform (AU), Mobile Uniform (MU), Point Uniform (PU), and Non-road Uniform (NU) simulations, and the (b) Base Case (BC), Area Increased Variability (AI), Mobile Increased Variability (MI), Point Increased Variability (PI), and Non-road Increased Variability (NI) sensitivity simulations.

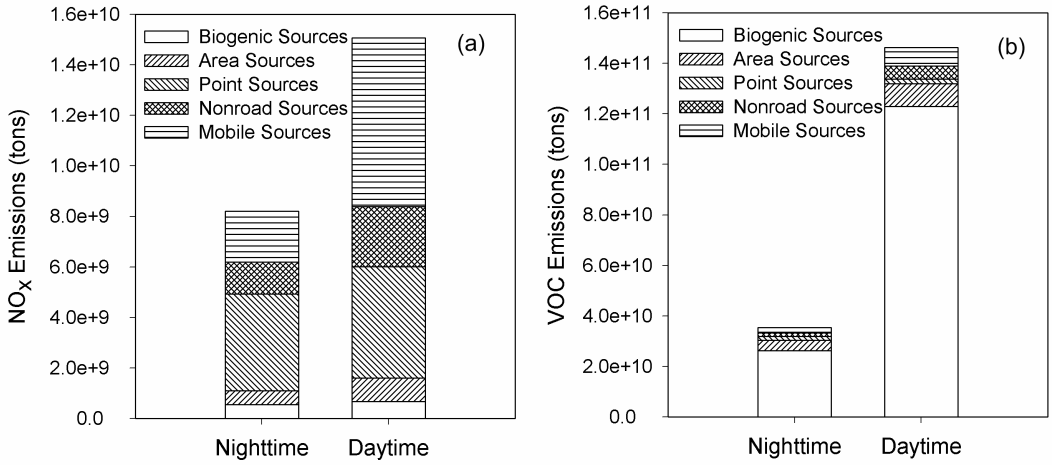

Figure 3.2: The base case domain total nighttime (12:00 am - 7:00 am EST and 7:00 pm - 12:00 pm EST) and daytime (7:00 am - 7:00 pm EST) NO_X (left) and VOC (right) emissions by emissions sector on August 21, 2002.

The sensitivities are averaged over the duration of the simulation, and the largest occur when the mobile emissions' temporal distributions are made uniform (Figure 3.3). The domain wide average and standard deviation of the MU sensitivities were -0.4 ± 0.4 ppbv, while the AU, PU, and NU sensitivities were 0.1 ± 0.1 ppbv, -0.1 ± 0.09 ppbv, and -0.2 ± 0.2 ppbv, respectively. The sensitivities in the MU simulation have a larger area of influence than the AU, PU, and NU cases because of the spatial distribution of area, point, and non-road sources varies, while motor vehicles are ubiquitous.

The average sensitivity of the 8HRMAX was also calculated for two subsets of conditions: 1) when an 8HRMAX of 50-80 ppbv occurred (moderate ozone days), and 2) when greater than 80 ppbv occurred (high ozone days) in the base case (Figure 3.4). The largest sensitivities occur in the latter case. In the MU simulation, on high ozone days there is a -7 ppbv (-6%) change in urban/suburban areas in the South, and a -3 to -4 ppbv change over most of the region. Offshore the sensitivities are +2-7 ppbv (+6%) in the North Atlantic. However, in the major city centers (e.g.; Chicago, Pittsburgh, New York City, Baltimore, Columbus, Detroit, and Indianapolis, etc.), where conditions may be VOC limited, on high ozone days a 1-2 ppb increase in the average 8HRMAX occurs because of decreased NO titration. Where the sensitivities are negative the number of days (out of the 123 day simulation) that the 8HRMAX exceeds 80 ppbv decreases by 5-8 days from 20-30 days in the base case (Figure 3.5 (d)). Where the sensitivities are positive, the number of 80 ppbv exceedance days increases by 0-2 days.

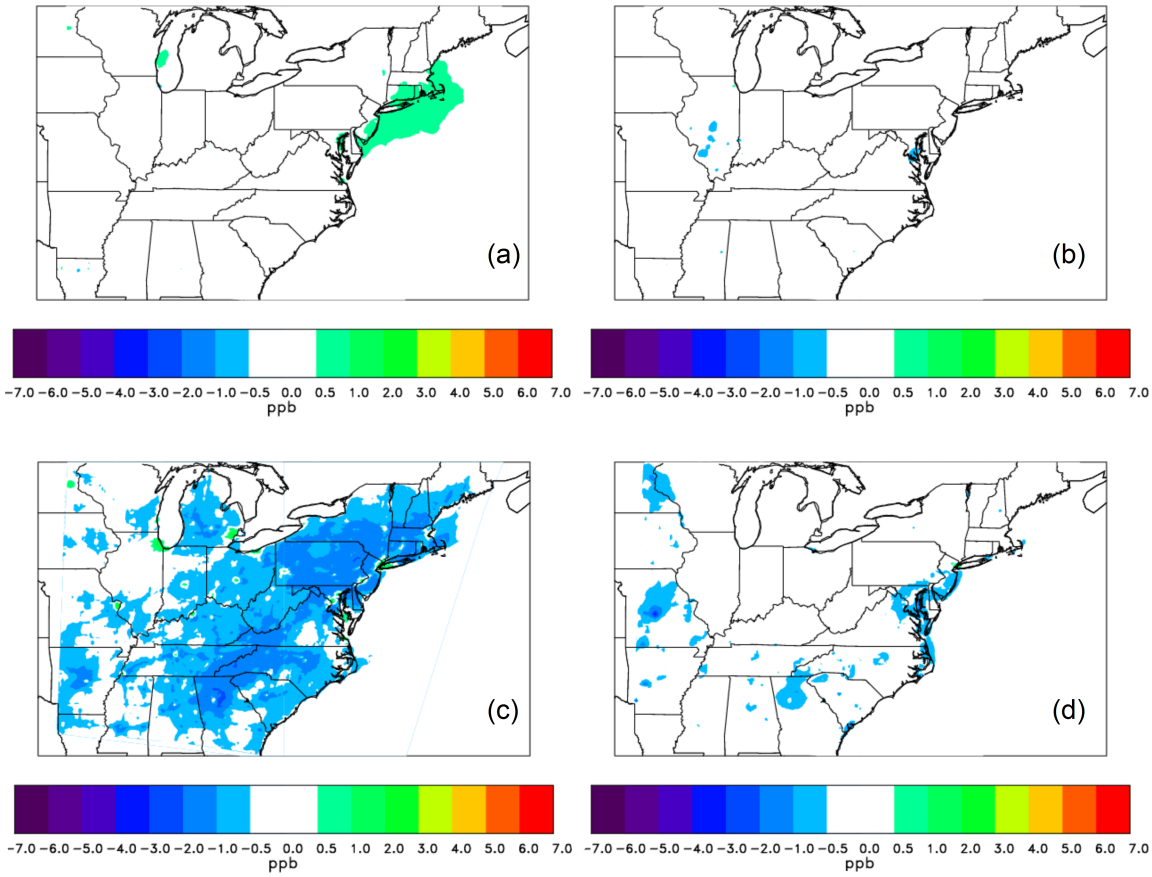

Figure 3.3: The mean bias $\left(\frac{1}{N}\sum \text{Uniform case - base case}\right)$ between the AU (a), PU (b), MU (c), and NU (d) case and the base case in the daily 8HRMAX in each grid cell from May 15 to September 15.

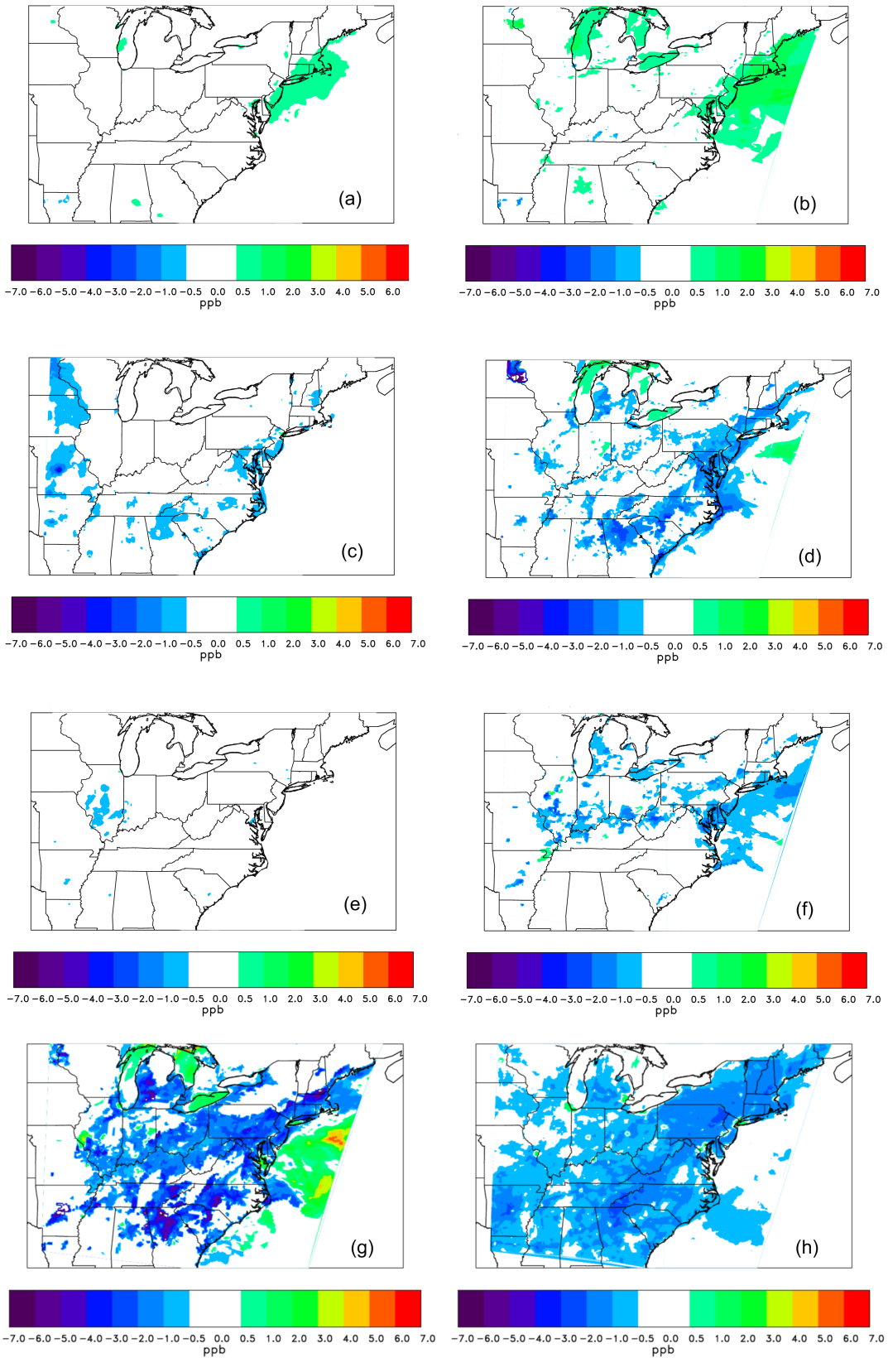

Figure 3.4: The mean bias between the AU (a, b), NU (c, d), PU (e, f),

and MU (g, h) simulation and the base case in the daily 8HRMAX in each grid cell from May 15 to September 15 when between 50 and 80 ppbv ozone (left column) and greater than 80 ppbv ozone (right column) occurs in the base case.

Non-road sources had the second largest area of influence. In the NU case, over most of the East Coast, the average 8HRMAX decreases by 2-4 ppbv on high ozone days resulting in a 1-4 day decrease in 80 ppbv exceedances (Figure 3.4 (c, d) & Figure 3.5 (b)).

In the AU case, along the I-95 corridor from Northern Virginia to Portland, ME, and in Alabama a 1-2 ppbv increase in the average 8HRMAX occurs on high ozone days (Figure 3.4 (a, b)). In Chicago and the middle of Kentucky, on high ozone days the 8HRMAX decreases by 1-2 ppbv, but practically no other areas in the region are affected. In the affected areas, the positive sensitivities result in 3-4 more days of 80 ppbv exceedances, and the negative sensitivities results in 1 less day of 80 ppbv exceedance (Figure 3.5 (a)).

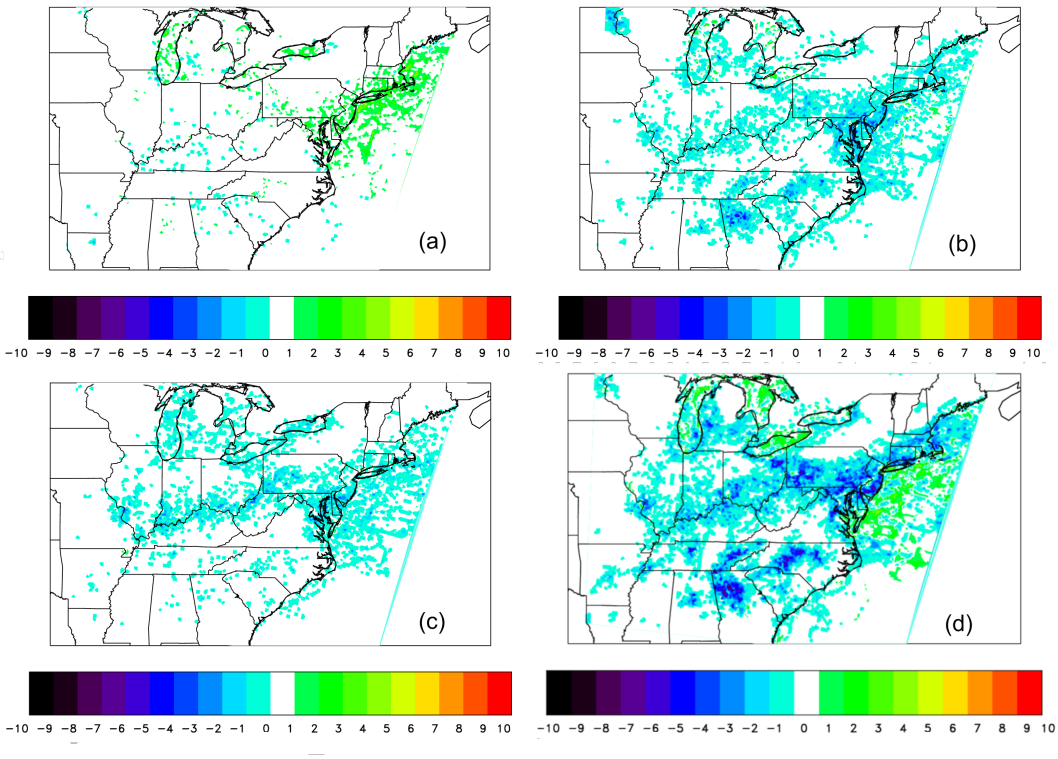

Figure 3.5: The difference between the AU (a), NU (b), PU (c), and MU (d) case and the base case in the number of days that the 8HRMAX exceeds 80 ppbv from May 15 to September 15.In areas where the base case predicted 20-30 days of exceedances, the MU case predicts 5-8 less days.

In the PU case, along the northern border of Kentucky, in the Midwest, Maryland, Delaware, and New Jersey the average 8HRMAX on high ozone days decreases by 1-3 ppbv (Figure 3.4 (e, f)). In Illinois, Missouri, Arkansas, Ohio, Pennsylvania, and Kentucky there are small areas where average 8HRMAX increases by 1-2 ppbv. The positive sensitivities occur adjacent to the negative sensitivities that are located near large point sources. Because the PU case shifts more point source emissions to the nighttime, we would expect an increase in ozone downwind of the point sources where the pollutants emitted above the nocturnal boundary layer mix

down to the surface. However, the effect of downward mixing seems to only occur close to the point source. The negative sensitivities result in 1-4 less days of 80 ppbv exceedances, and the positive sensitivities result in 0-2 more days of 80 ppbv exceedances (Figure 3.5 (c)).

In order to gauge the effect of the source category temporal distributions on urban areas in the region, where high ozone is a problem, we compare the 8HRMAX frequency distribution of the base case in urban and rural areas to the sensitivity runs. In this analysis, urban areas were defined as grid cells with population greater than 193 people per km^2, or 500 people per square mile, according to the year 2000 census data. The 8HRMAX frequency distributions of the AU, PU, and NU cases do not change with respect to the base case, because the sensitivity effects are too localized. In the MU case, the frequency distribution for rural areas remains similar to the base case, while in urban areas the fraction of 70-95 ppbv 8HRMAX concentrations decreases, and the fraction of 40-60 ppbv 8HRMAX concentrations in the MU simulation increases from the base case, indicating an overall downward shift in urban ozone concentrations in the region (Figure 3.6).

3.7.3 Regional Sensitivity to Increased Variation in Temporal Distributions.

When the diurnal variation of area (AI), point (PI), non-road (NI), and mobile (MI) emissions is increased, smaller sensitivities than the uniform cases are observed (Figure 3.7). The increased temporal variability of area sources has very little effect;

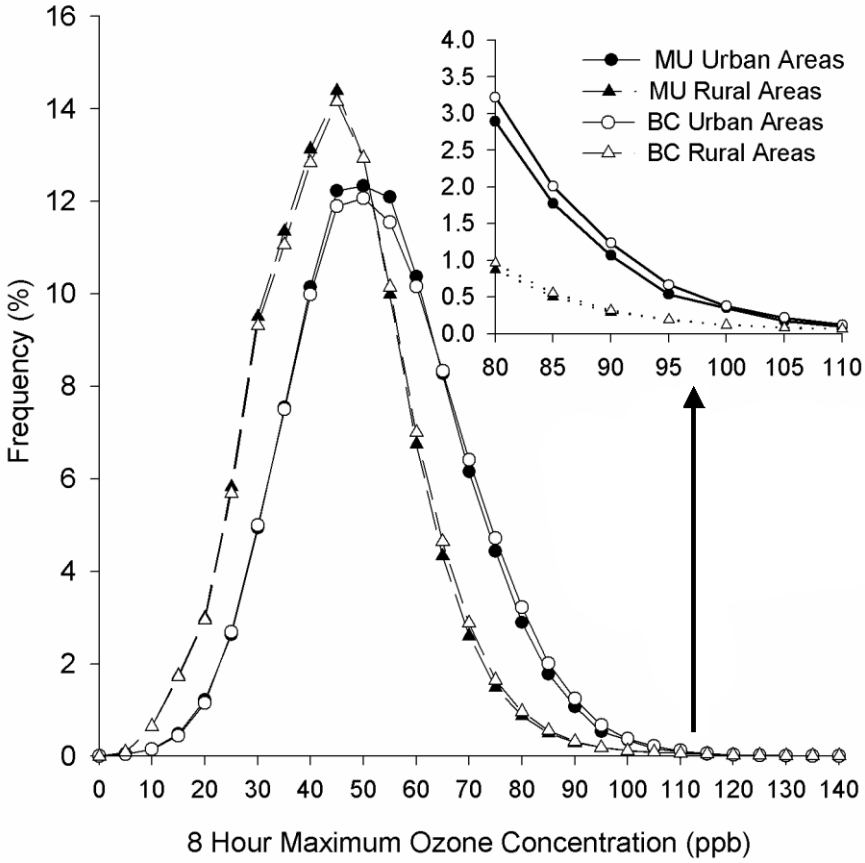

Figure 3.6: The frequency distribution of the 8HRMAX in urban (circles) and rural (triangles) areas in the base case (open markers) and MU case (filled markers). The top right corner inset is an enlargement of the right tail of the frequency distribution. In urban areas the fraction of 70-95 ppbv 8HRMAX concentrations decrease, and the fraction of 40-60 ppbv 8HRMAX concentrations in the MU simulation increases from the base case.

the map of sensitivities shows less than 1 ppbv change throughout the domain (Figure 3.7; (a) & Figure 3.8 (a, b)).

In the (NI) case the domain wide average 8HRMAX sensitivity is 0.06 ± 0.1 ppbv. However, in the Ohio River Valley, West Virginia, and Kentucky the average 8HRMAX decreases by 2-3 ppbv on high ozone days (Figure 3.8 (d)). In the south, the 8HRMAX increases by 1-2 ppbv on high ozone days. These sensitivities result in 1-3 less and 1-2 more 80 ppbv exceedances, respectively (Figure 3.9 (b)).

In the MI case, the domain wide average 8HRMAX sensitivity is 0.09 ± 0.2 ppbv. Throughout the domain, the average 8HRMAX increases by 1-2 ppbv on high ozone days, and up to 5 more exceedances than the base case of 80 ppbv occur (Figure 3.8 (h) & Figure 3.9 (d)). However, the rural and urban frequency distributions of the 8HRMAX for the MI case do not significantly change from the base case.

Increasing the temporal variation of point source (PI) emissions also results in small domain wide sensitivities: 0.04 ± 0.3 ppbv. Larger localized sensitivities on high ozone days on the order of +6 ppbv occur near Atlanta, Birmingham, Knoxville, and Nashville (Figure 3.8 (f)). In the Ohio River Valley, Indiana, Illinois, Tennessee, and Kentucky, small areas of positive 1-6 ppbv and negative 1-5 ppbv sensitivity occur adjacent to each other, suggesting that, similar to the PU case, the effects of changes in emissions from the large point sources located in this region for the most part remain close to the source. Because the PI case increases point source emissions during the daytime, one might expect that ozone would decrease at the location of the large point sources because of NO_X titration. However, in these areas

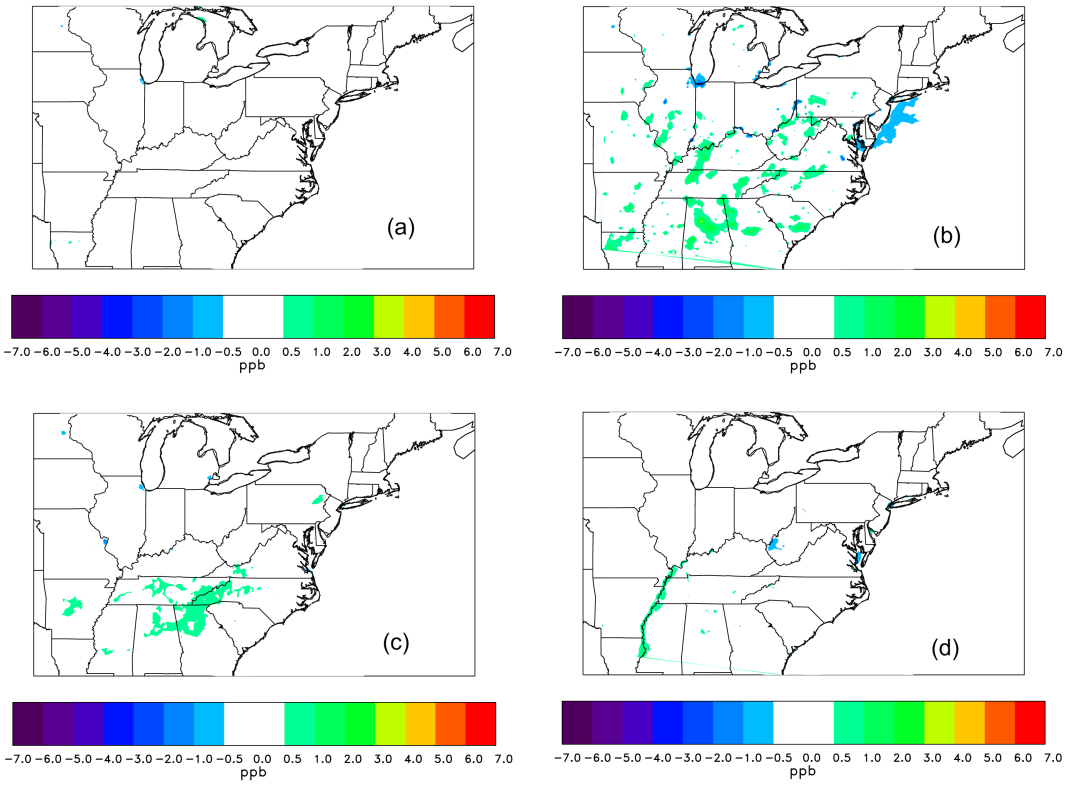

Figure 3.7: The mean bias between the AI (a), PI (b), MI (c), and NI (d) case and the base case in the daily 8HRMAX in each grid cell from May 15 to September 15.

there is enough isoprene such that conditions are NO_X limited (Figure 3.10).

This result, along with the PU case, is in agreement with the spatial correlation analysis conducted by Gilliland, et al., (2008). They found that when point source emissions are changed according to measurements before and after the NOx SIP Call, the subsequent changes in model ozone concentrations are a result of changes in emissions sources that are close by rather than transported emissions. However, a comparison of CMAQ to ground observations shows that CMAQ underestimates the ozone e-folding distance; the observed effects of the point source emissions changes

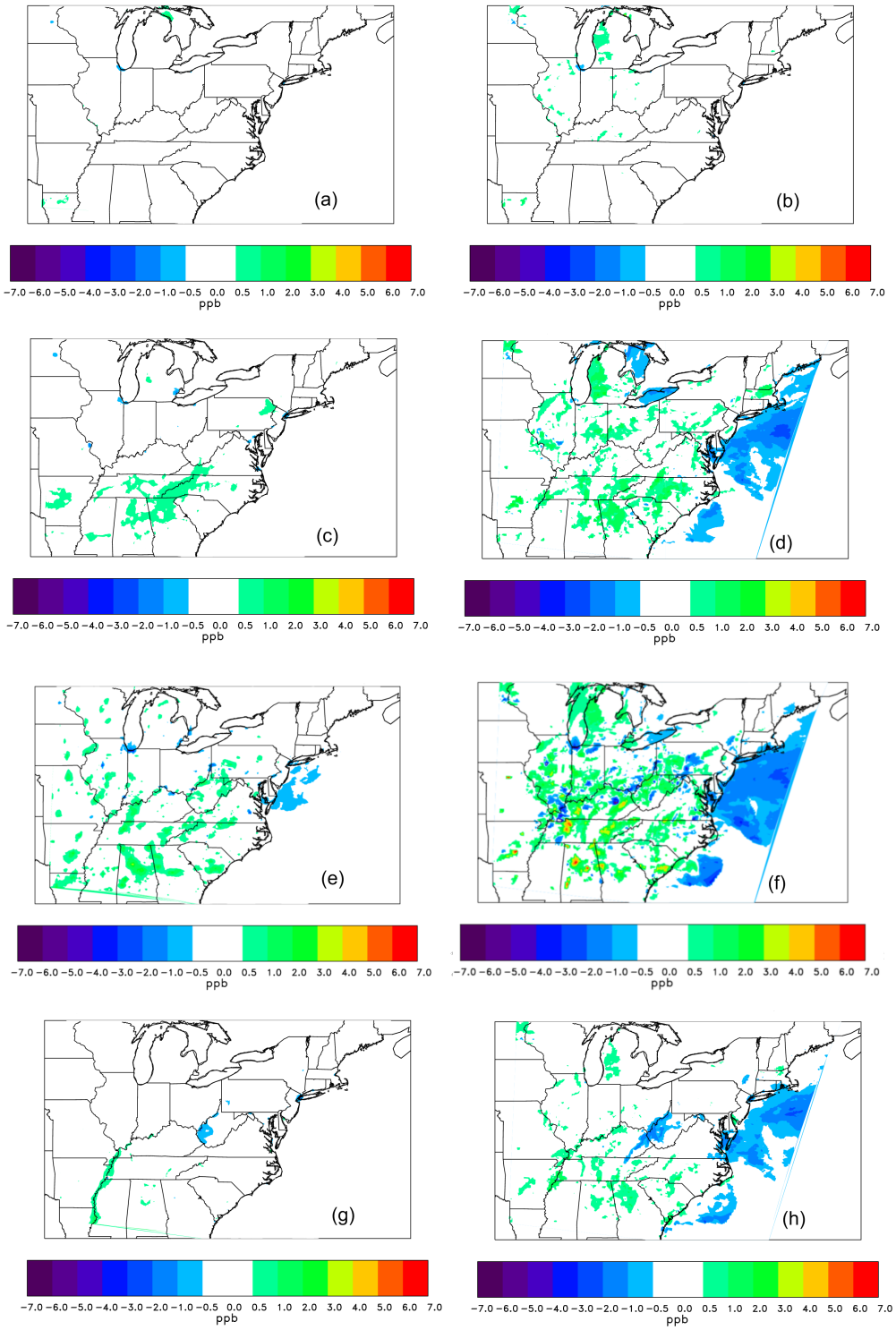

Figure 3.8: The mean bias between the AI (a, b), NI (c, d), PI (e, f), and MI (g, h) simulation and the base case in the daily 8HRMAX in each grid cell from May 15 to September 15 when between 50 and 80 ppbv ozone (left column) and greater than 80 ppbv ozone (right column) occurs in the base case.

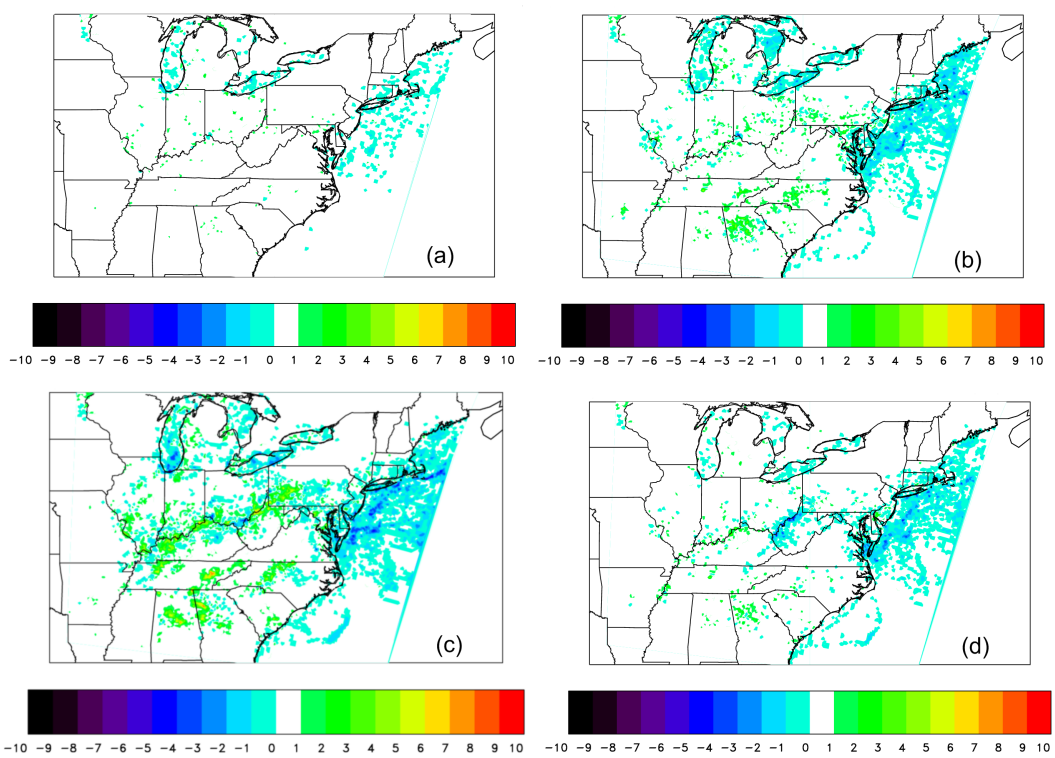

Figure 3.9: The difference between the AI (a), NI (b), PI (c), and MI (d) case and the base case in the number of days that the 8HRMAX exceeds 80 ppbv from May 15 to September 15.

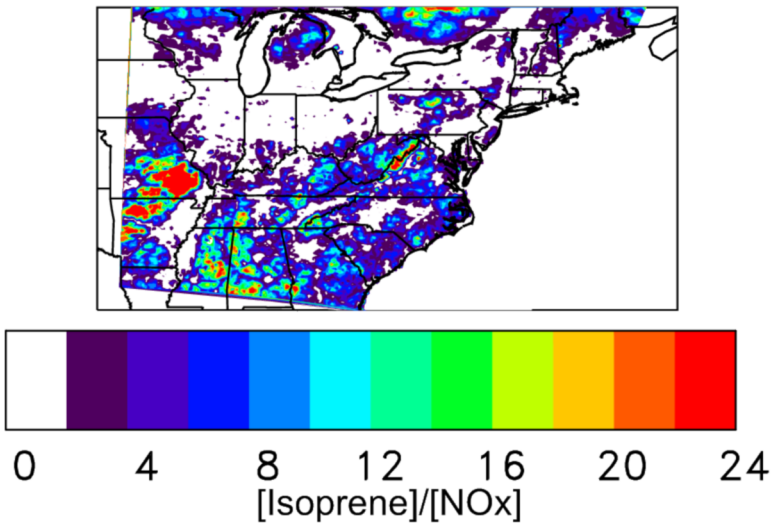

Figure 3.10: The ratio of the average concentration of daytime (7:00 am - 7:00 pm EST) isoprene to NO_X averaged over the summer. In the Ohio River Valley, West Virginia, and areas throughout Georgia and Louisiana there is enough isoprene such that conditions are NO_X limited. Thus, more ozone is generated close to the large point sources when NO_X emissions increase during the day in the PI case.

were more wide spread than the model predicts. This corroborates similar finding by Bloomer, et al. (2009), Hains, et al. (2008), Kim, et al. (2006) and suggests that if the model were able to simulate pollutant transport as seen in the observations, the area and magnitude of the sensitivities in the PI and PU simulations would be larger.

3.7.4 Local Sensitivities

Baltimore and Atlanta were selected for further analysis based on the results of the regional sensitivities. Average hourly ozone measurements at three monitoring sites near each of the cities were compared to each of the sensitivity simulations: two monitoring sites within the Photochemical Assessment Monitoring Stations (PAMS) network, and one within the Clean Air Status and Trends Network (CASTNET). The CASTNET sites, Arendtsville (site id: ARE128) near Baltimore and Sand Mountain (site id: SND152) near Atlanta, provide data on rural ozone levels. The PAMS monitoring stations are located within and downwind of polluted areas where emissions of precursors and their effects can be observed. Essex (site id: 24-005-3001) and Tucker (site id: 13-089-3001) are the PAMS type 2 sites for Baltimore and Atlanta, respectively, and are located within the area of maximum emissions levels. Aldino (site id: 24-025-9001) and Conyers (site id: 13-247-0001) are the PAMS type 3 sites, and lie predominantly downwind of Baltimore and Atlanta, respectively. A map of the locations of the six selected sites is shown in Figure 3.11. Site descriptions can be found at http://www.epa.gov/oar/oaqps/pams/ and

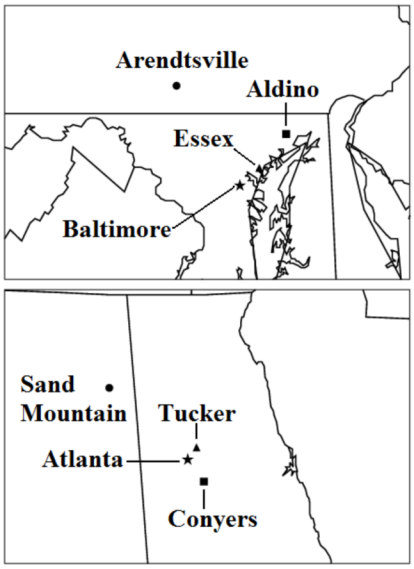

Figure 3.11: The location of the PAMS type 2 (triangles), PAMS type 3 (squares), and CASTNET (circles) monitoring sites used for local sensitivity analysis in Baltimore (top) and Atlanta (bottom).

http://www.epa.gov/castnet/site.html.

Overall, the largest effect on the modeled hourly ozone values at the selected monitoring sites occurs at night when mobile emissions are temporally uniform. The increased nighttime emissions from the mobile source group, which are rich in NO_X, in the MU case, build up locally during typically stagnant conditions and destroy ozone via NO_X titration. Thus, at the Essex and Tucker sites, the MU simulation causes hourly ozone values at night to decrease from the base case by up to 10 ppbv. Yet, compared to observations, the MU simulation has better model performance at night than the base case (Figure 3.12 (a, c)). Conversely, when mobile source temporal variations are increased and NO_X emissions decrease at night, at these sites, the MI simulation nighttime ozone values are slightly higher than the base

case (Figure 3.12 (b, d)).

At the Aldino site, the nighttime hourly ozone values predicted in the base case are close to measurements. Thus, increasing NO_X emissions at night in the MU simulation results in underestimated ozone. Also, the model predicts the ozone maximum one hour earlier than the measurements at this site. When the diurnal variation of the emissions is changed in the sensitivity simulations, there is no change in when the peak ozone values occurs (Figure 3.13 (a, b)). At the Conyers site, similar to the Tucker site, the model reproduces the diurnal variation of ozone, but overestimates ozone at night. Likewise, the MU simulation lowers the nighttime ozone concentrations from the base case at this site, although ozone predictions remain 10 ppbv greater than observations (Figure 3.13 (c)).

In order for the AQM to capture the diurnal variation of observed ozone, especially the nighttime minimum, first the meteorological model must reproduce the diurnal variation of the planetary boundary layer (PBL). Unfortunately, few temporally and spatially detailed boundary layer observation datasets exist that can be used to validate model results. However, Rao, et al. (2003) were able to evaluate the mixing height from a 1995 MM5 simulation using the Blackadar PBL scheme with sounding data from the North American Research Strategy for Tropospheric Ozone-Northeast (NARSTO-NE) (Berman, et al., 1999) field program and found good agreement at night. Additionally, it has been shown that the modified Blackadar scheme used in this work is best suited for simulating diurnal cycles of surface wind speed in relation to surface temperature (Zhang and Zheng, 2004). Although the Rao, et al. (2003) comparison is for a different model year than this study,

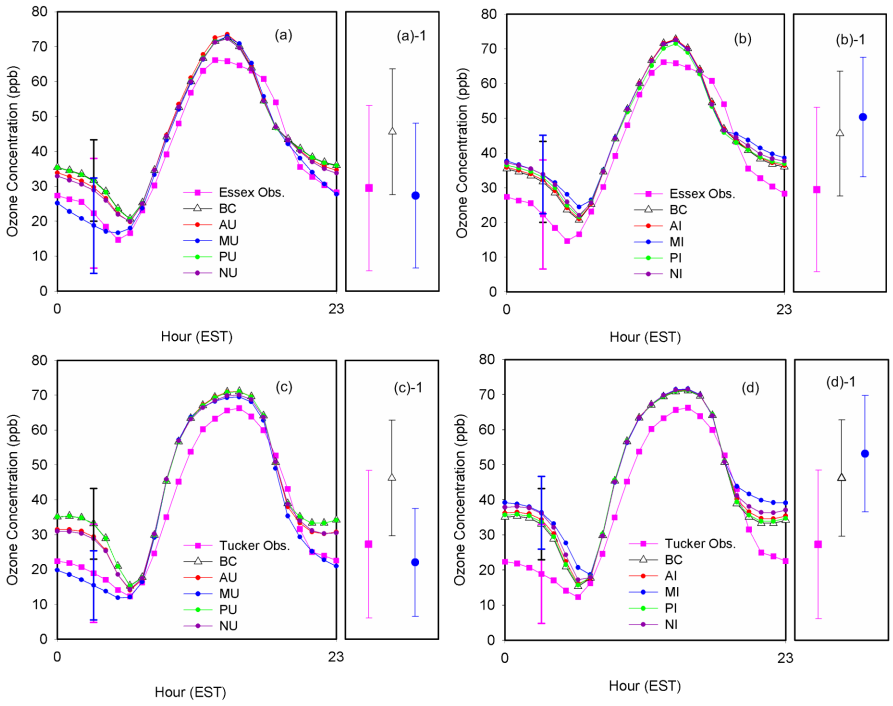

Figure 3.12: The hourly ozone concentrations averaged in time that were observed (pink squares) and modeled at the Essex (a, b) and Tucker (c, d) monitoring sites. The modeled average hourly ozone concentration plots are separated into uniform (left column) and increased variability (right column) groups. The base case (open triangles) is plotted with both groups. The error bars on the fourth point in each figure correspond to the standard deviation of the observed (pink), base case (black), and mobile case (blue) hourly ozone concentrations, and are typical for all hours. The plot to the right of each diel plot (a-1, b-1, c-1, d-1) is a magnification of these points next to each other to better illustrate the overlapping error bars. At the Essex and Tucker sites, the summer long average decrease from the base case in nocturnal ozone when mobile emissions are uniform is larger than one standard deviation.

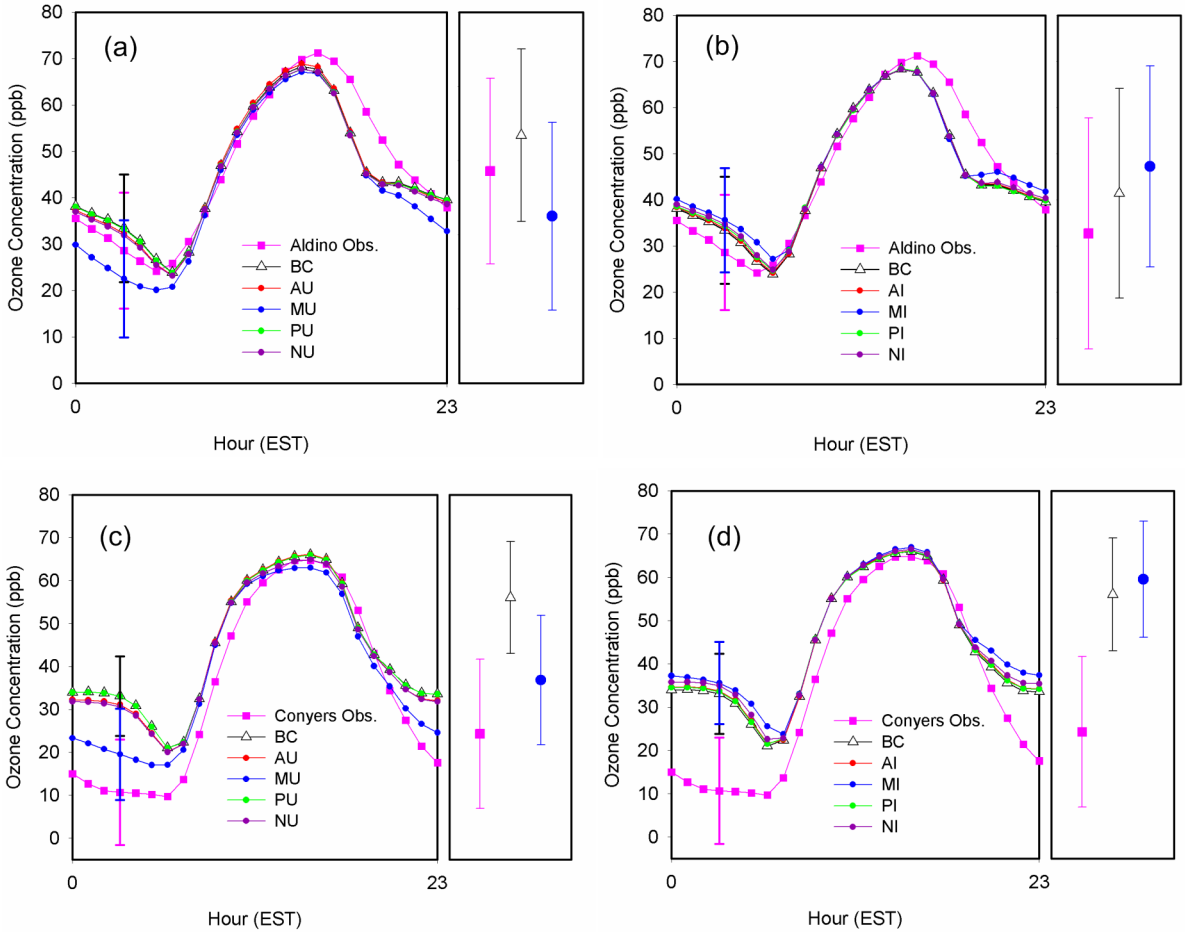

Figure 3.13: The hourly ozone concentrations averaged in time that were observed (pink squares) and modeled at the Aldino (a, b) and Conyers (c, d) monitoring sites. The modeled average hourly ozone concentration plots are separated into uniform (left column) and increased variability (right column) groups. The base case (open triangles) is plotted with both groups. The error bars on the fourth point in each figure correspond to the standard deviation of the observed (pink), base case (black), and mobile case (blue) hourly ozone concentration, and are typical for all hours. The plot to the right of each diel plot is a magnification of this point.

because MM5 has acceptable model performance for the other observed meteorological variables in this work, we will assume our simulation does a reasonable job at reproducing nocturnal mixing heights. It follows that the overestimation of nighttime ozone by the base case at the PAMS type 2 sites may be the result of another weakness in the model.

One cause of some of the overestimation of nocturnal ozone by the model may be the strong gradient in ozone concentration near the surface. The model value represents the concentration at the mid-layer height (10 m), while the observations are made at 5 m. The lower nighttime ozone values at the Essex and Tucker sites in the temporally uniform simulations, especially the MU case, suggest that underestimated NO_X emissions and/or overestimated losses of NO_X at night may also play a role in the nighttime over prediction of ozone by CMAQ in urban areas. This reasoning seems appropriate for the Essex site where the NO_X model performance improves in the MU case. The base case underestimates observed nighttime NO_X concentrations by 38%, while the MU case underestimates nighttime NO_X by 10%. However, at the Tucker site, the base case nighttime NO_X concentrations agree well with observations, except for over predictions from 19:00 to 21:00 local time, while the MU case over predicts nighttime NO_X observations by 95% (Figure 3.14).

At the rural CASTNET sites, Arendtsville and Sand Mountain, the model has a low bias during the day (Figure 3.15). At night, the model underestimates ozone over Arendtsville, and overestimates ozone over Sand Mountain. Regardless, the sensitivity simulations have very little effect on the performance of the model at these rural sites. The low daytime bias may be due to the reaction rate of the

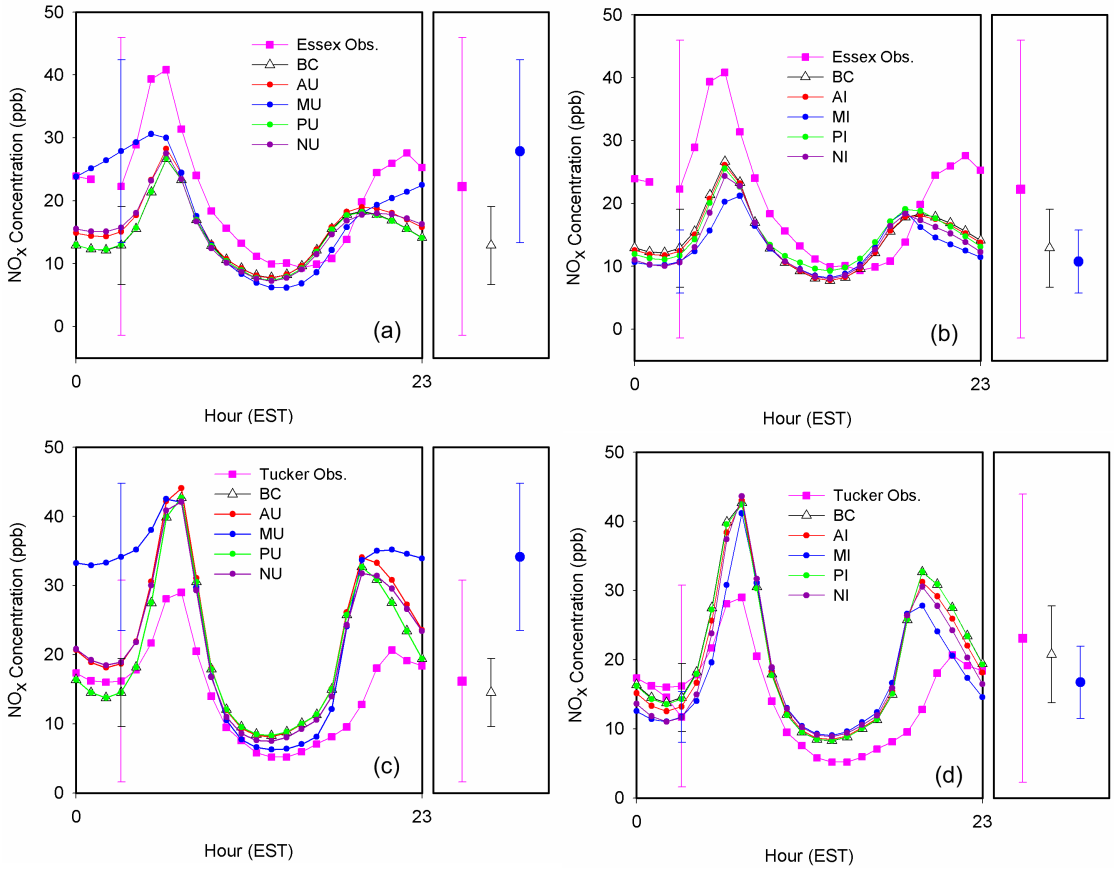

Figure 3.14: The hourly NO_X concentrations averaged in time that were observed (pink squares) and modeled at the Essex (a, b) and Tucker (c, d) monitoring sites. The modeled average hourly ozone concentration plots are separated into uniform (left column) and increased variability (right column) groups. The base case (open triangles) is plotted with both groups. The error bars on the fourth point in each figure correspond to the standard deviation of the observed (pink), base case (black), and mobile case (blue) hourly ozone concentration, and are typical for all hours. The plot to the right of each diel plot is a magnification of this point. At the Essex site, NO_X model performance improves in the MU case.

hydroxyl radical with NO_2 in CB-IV that terminates the hydroxyl radical too quickly during the daytime and inhibits the production of ozone through the oxidation of aldehydes (Faraji, et al., 2008). This mechanism would be important in rural areas where VOCs from biogenic emissions dominate.

3.8 Discussion and Implications

Mobile emissions have the largest temporal variation in the base case emissions inventory. Making the temporal variation of this source group uniform caused the largest effects on the 8HRMAX. Particularly, the 8HRMAX decreased in urban areas on days with high (greater than 80 ppbv) ozone by up to 7 ppbv, resulting in a decrease in the number of 80 ppbv exceedances. This result has significant policy implications in terms of calculating relative reductions for demonstrating attainment with the NAAQS. From a regulatory perspective, the decrease in the number of 80 ppbv exceedances in the MU simulations demonstrates that accurate representation of daily variability of mobile emissions is necessary to simulate ozone correctly. The other emissions source groups also affected the number of 80 ppbv exceedances, but on a more local level. This reinforces the importance of understanding local emissions characteristics in order to compose effective ozone abatement strategies.

The results from the MU case also demonstrate the upper limits of intentionally shifting traffic patterns as an abatement strategy. If traffic emissions occurred more at night and less in the day, there would be fewer ozone events. Such a temporal shift might be accomplished by switching to electric cars charged at night, or increasing

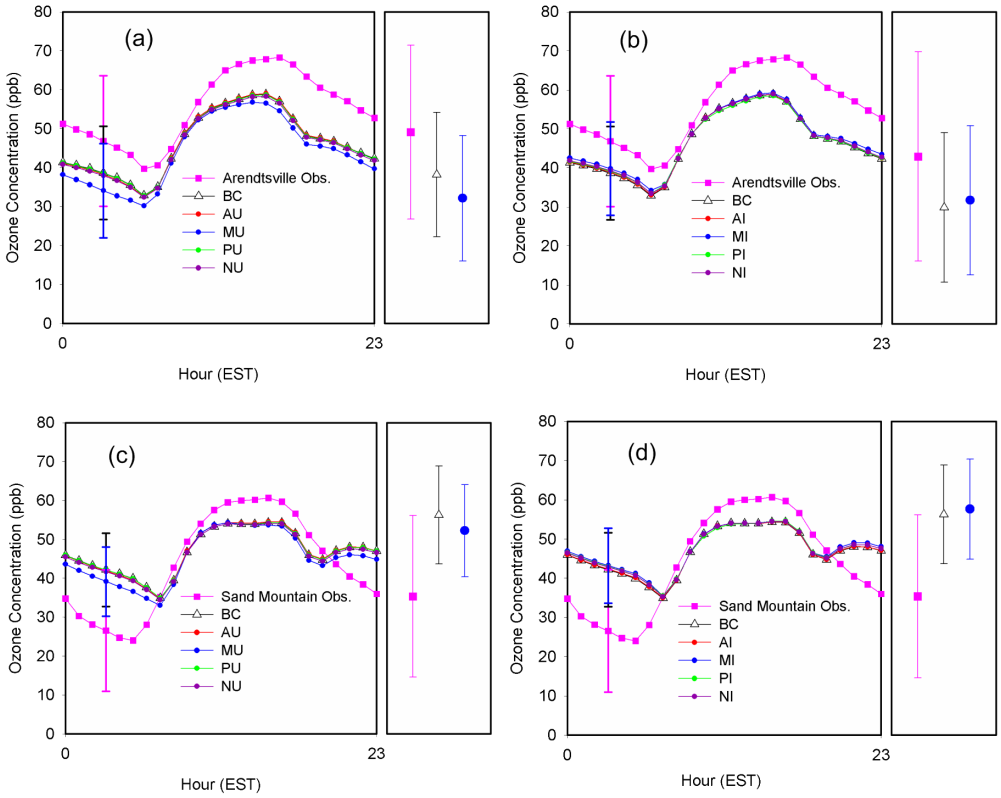

Figure 3.15: The hourly ozone concentrations averaged in time that were observed (pink squares) and modeled at the Arendstville (a, b) and Sand Mountain (c, d) monitoring sites. The modeled average hourly ozone concentration plots are separated into uniform (left column) and increased variability (right column) groups. The base case (open triangles) is plotted with both groups. The error bars on the fourth point in each figure correspond to the standard deviation of the observed (pink), base case (black), and mobile case (blue) hourly ozone concentration, and are typical for all hours. The plot to the right of each diel plot is a magnification of this point.

the number of high occupancy vehicle lanes in a metropolitan region, which would force commuters to drive at off peak hours. In fact, if a larger fraction of the vehicle fleet became electric cars, an even greater decrease in ozone could occur because overall NO_X emissions should decrease (total emissions from power plants are capped, while emissions from cars are limited by the per vehicle miles traveled).

Because point sources are the largest nighttime emitters in the base case emissions inventory, increasing the temporal variation of this source group has the greatest effect. Similar to the result from the PU case, changes in the 8HRMAX and the number of 80 ppbv exceedances mostly occur close to the emissions sources. The patchy result of positive and negative sensitivities close to each other may be due to the weakness of the model at transporting point source emissions, which underestimates the area and magnitude of ozone generated by point source emissions. Because of this weakness the model appears to be able to respond more realistically to emissions control strategies that target the time of day of emissions from mobile, area, and non-road sources, than from point sources.

We find from comparisons at several monitors that the largest differences between the base case and temporal sensitivity simulations occur in the nighttime (similar to Tao, et al. (2004)), especially in urban areas when the mobile emissions temporal distribution is uniform. Model performance is poor at night, but improves in urban areas when mobile emissions are made uniform in time. Correcting model underestimated nighttime NO_X emissions and/or overestimated NO_X losses will enhance the numerical simulation of ozone and our ability to evaluate pollution abatement strategies. Adequate treatment by the model of the night-to-day ozone

accumulation process is essential to photochemical modeling (Rao, et al., 2003), and will become especially important as emissions and ozone concentrations decrease.

Chapter 4

CMAQ Model Performance of CO

4.1 Introduction

CO is an ideal tracer for analyzing pollutant transport in AQMs because its atmospheric lifetime, on the order of a month, is longer than the timescale of boundary layer mixing, but short enough for easily measured gradients. To use CO as a tracer, model performance of CO must be well understood; the sources, sinks, and resulting total CO must be accurate. Although the atmospheric chemistry of CO is well known and implemented in the model in a straightforward manner, the strength of the sources and sinks of CO are less certain.

Until recently, the precision of surface CO monitoring in the national monitoring networks has been low; often only one significant figure was reported (U.S. Environmental Protection Agency, 2009). Only datasets from intensive field campaigns or select research surface sites are available for CO model performance evaluation. Comparison of the Eta-CMAQ air quality forecast model to the dataset from the International Consortium for Atmospheric Research on Transport and Transformation (ICARTT) study (an intensive field campaign that measured trace gases from surface, aircraft, and ships during the summer of 2004) found a 20-30% low bias in modeled CO at all altitudes (Yu, et al., 2007, 2009). This is attributed to a misrepresentation of biomass burning emissions in the model, which occurred in Alaska

and Canada at the time. A comparison of CMAQ to 2000-2001 CO concentrations observed at Southeastern Aerosol Research and Characterization (SEARCH) sites found that modeled CO concentrations have a 36% low bias (Marmum, et al., 2009). However, Parrish (2006) compared the Mobile6 motor vehicle CO emissions inventory to a fuel based inventory, and found that CO emissions from motor vehicles are overestimated by a factor of two. Kuhns, et al., (2004) compared Mobile6 CO emissions factors to those measured by roadside remote sensing of vehicle exhaust. Mobile6 CO emissions factors were 50% too low for diesel vehicles (a minor source overall), but were 50% too high for gasoline-powered vehicles. Bishop and Stedman, (2008) reported that deterioration rates of control technology in motor vehicles was overestimated by a factor of five in Mobile6. Hudman, et al., (2008) and Warneke, et al., (2006) also found that CO anthropogenic emissions are 50-60% too high. However, they compared 2004 observations to the 1999 NEI. An evaluation of CO in CMAQ is needed to use the model as a tool for analyzing vertical mixing in the boundary layer, and the role of pollutant transport in ozone formation.

In this work, I will compare CMAQ to CO vertical profiles taken at various locations throughout the Mid-Atlantic by the Regional Atmospheric Measurement, Modeling and Prediction Program (RAMMPP), and high precision surface observations at select monitoring sites across the Northeast.

4.2 Modeling Set-Up

The modeling domain, meteorology, emissions, and AQM set-up described for the base case in Chapter 3 were used. However, in this work the MM5 outputs were processed with MCIP v3.4.1 wherein the CO mesophyll resistance was updated to correspond with the value predicted by the effective Henry's law constant. This reduces the deposition velocity from ∼0.4 cm/s to ∼0.1 cm/s and increases the modeled lifetime of CO back to a realistic value of weeks.

4.3 Measurement of CO Vertical Profiles and at CO Surface Sites

Vertical profiles of CO at 34 small airports across the Northeast US (Figure 4.1-4.3) were measured for the RAMMPP project from May through August of 2002. Observations were taken on days where high ozone concentrations were forecasted. The flight plans were designed such that in the morning the spirals were located generally upwind of major cities, and in the afternoon the spirals were downwind of major cities. Some locations will be upwind of one city and downwind of another city depending on the synoptic conditions. Out of 115 total vertical profiles, 42 profiles were measured at 19 airports between 7-10 AM local time, before thermal convection creates a high well-mixed boundary layer (Figure 4.2). The other 73 profiles were measured in the afternoon at 27 airports (Figure 4.3).

CO measurements were taken with a modified Thermo Scientific CO infrared filter correlation analyzer (Model 43C, Franklin, MA) (Dickerson and Delany 1988) on a twin engine Piper Aztec airplane. The instrument sampled from a backward

facing inlet on top of the airplane. Trace gas vertical profiles were obtained at a vertical climb rate of 100 m/min between 3 m and ∼3000 m above ground level (AGL). Temperature, pressure, O_3, SO_2, particle number concentration, and particle size were also measured. A full description of the aircraft instrument package can be found in Hains (2007).

CO surface monitoring data were extracted from the EPA Air Quality System (AQS) monitoring network at ten sites shown in Figure 4.3, where CO measurement precision was at the ppbv level. These observations were taken with Monitor Labs (Model 8310, Englewood, CO), Dasibi (Model 3003, Glendale, CA), or Thermo Electron (Model 48, Franklin, MA) infrared filter correlation analyzers.

Observations taken on July 5-8 were excluded from the analysis (three morning and three afternoon spirals) when the Mid-Atlantic region was affected by a plume of CO from several large forest fires in Quebec that caused very high concentrations of CO and PM in the region (Sigler, et al., 2003, Taubman, et al., 2004, Sapkota, et al., 2005). Aircraft observations of this plume show CO concentrations aloft as high as 15 ppm (Figure 4.5). These fire emissions were not included in the model.

4.4 Results and Discussion

4.4.1 Comparison of Modeled and Observed CO Vertical Profiles

The diurnal variation of CO surface observations is shown in Figure 4.6. In all comparisons hereafter the modeled and observed values are paired in time and space, without interpolation. The observed and modeled CO diurnal variations have

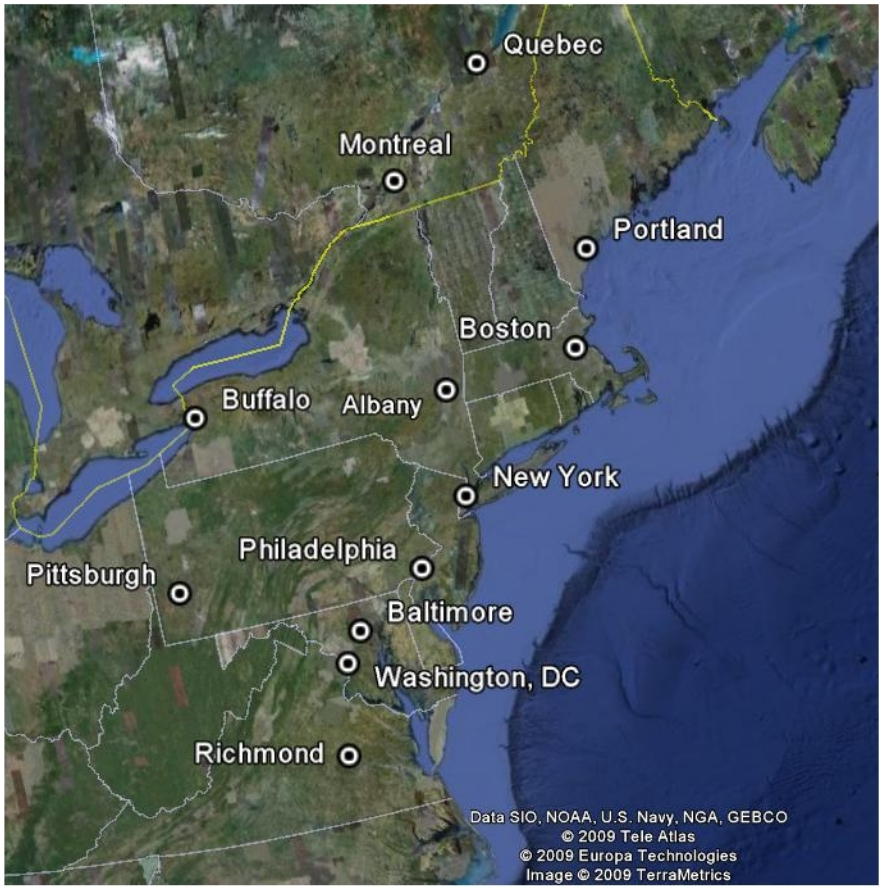

Figure 4.1: The locations of some major cities in the Mid-Atlantic

Figure 4.2: The locations of the morning (7-10 AM local time) CO vertical profiles, with corresponding airport codes.

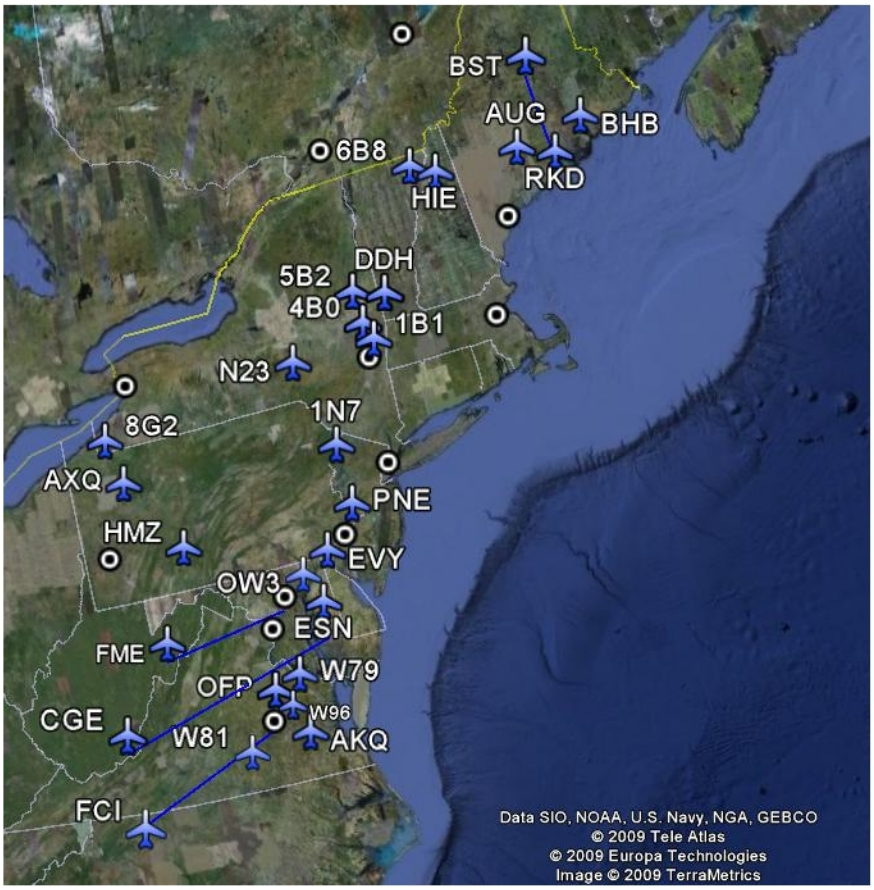

Figure 4.3: The locations of the afternoon CO vertical profiles, with corresponding airport codes.

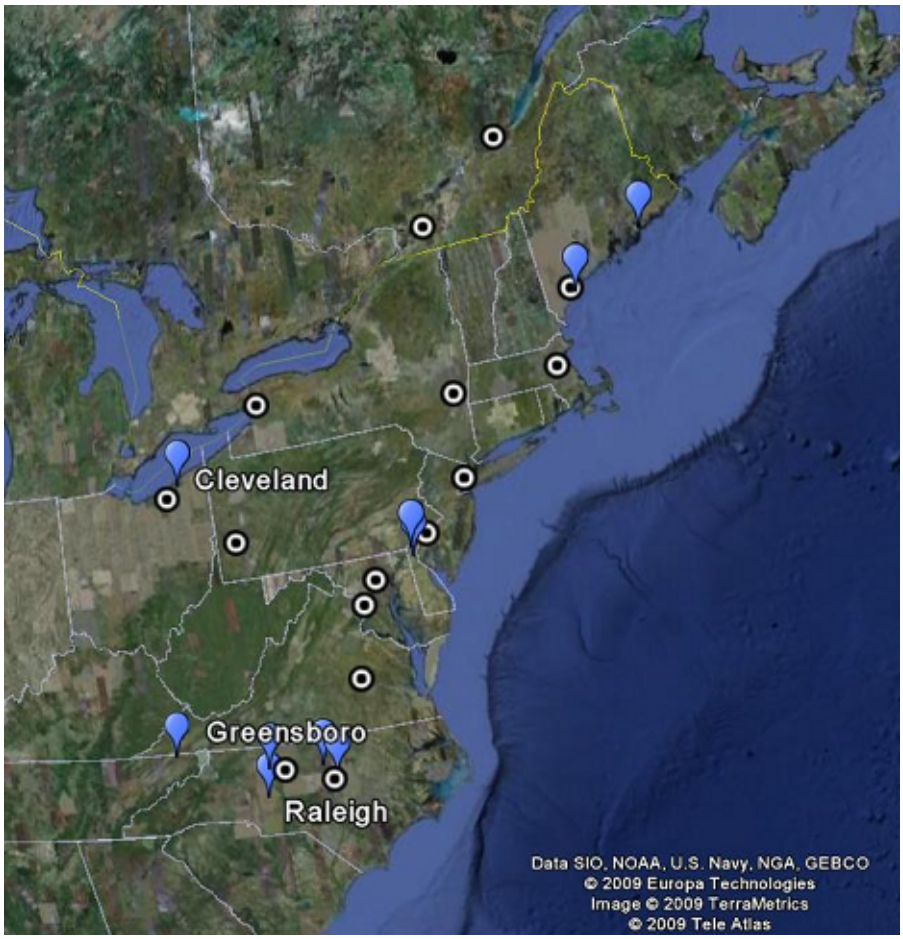

Figure 4.4: Map of locations of some major cities in the Mid-Atlantic (a), the place marker represent locations of CO surface monitoring sites.

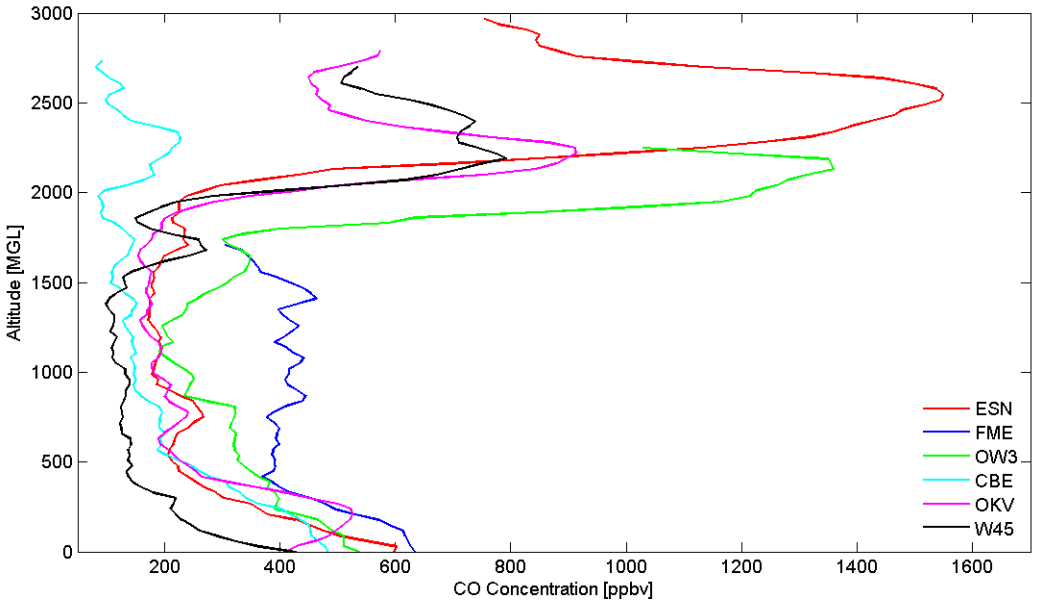

Figure 4.5: Observed CO vertical profiles at six airports on July 8, 2002. On this day, most of the Mid-Atlantic was affected by a plume of biomass burning emissions that originated in Quebec. These results were first published in Taubman, et al., (2004).

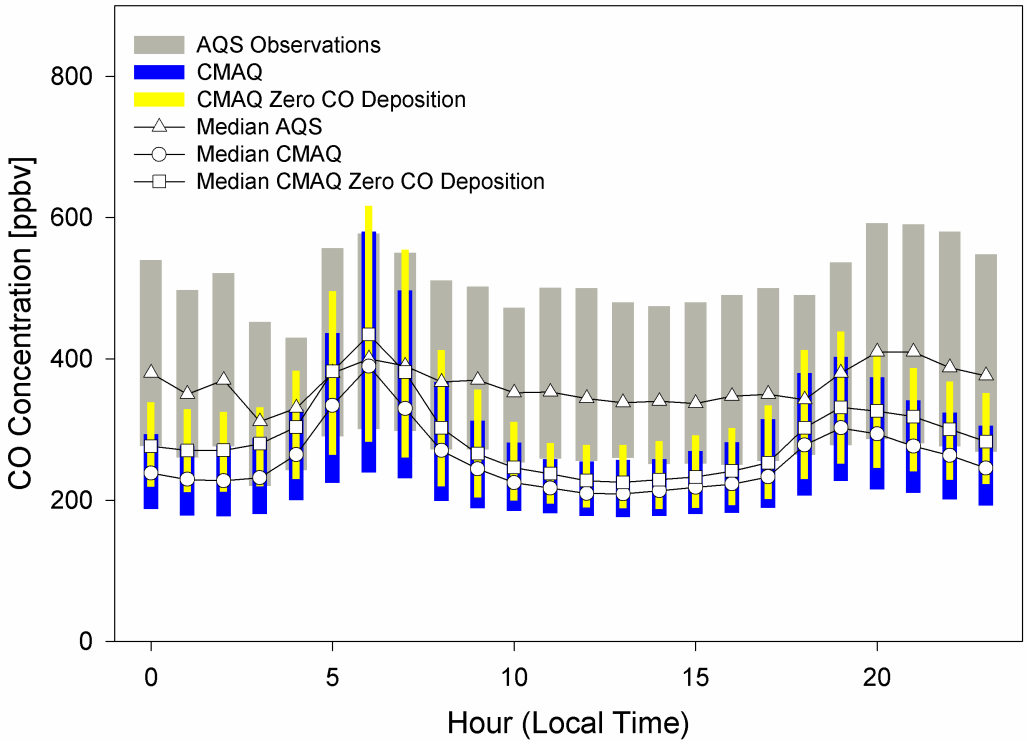

Figure 4.6: Comparison of modeled and observed (triangles, gray bars) surface CO diurnal variation for sites shown in Figure 4-2. The bars represent the 25th and 75th percentiles, and the markers correspond to the median hourly concentration. The blue bars and circles correspond to modeled CO, and the yellow bars and squares correspond to modeled CO with the deposition velocity set to zero.

a distinct local maximum at 6 AM that corresponds with morning rush hour. In the evening there is a second local maximum that corresponds with evening rush hour, and the collapse of the boundary layer. In general, the median observed surface CO concentration is between 350-400 ppbv. At night, the observed CO concentration is slightly higher than afternoon values, reflecting the buildup of pollutants in the nighttime boundary layer. Modeled CO concentrations are ∼40% less than observations, except at 6 AM when measurements and model agree.

The medians and quartiles of observed and modeled morning and afternoon vertical profiles of CO are shown in Figure 4.7 and 4.8. In the morning, when thermal convection is beginning to break up the nocturnal temperature inversion, but the PBL has not vented to its full height (the atmosphere is still stratified below the subsidence inversion), observations show a peak in CO concentration at the surface that decreases at a rate of 0.5 ppb/m up to an altitude of ∼500 m. This is roughly the height of the PBL determined from the observed temperature inversion, but higher than the model prediction. Above 500 m, CO is well mixed and has a median value of ∼150 ppb; close to the continental background value of 140 ppb. The CMAQ vertical profile corresponds well with observations in the well-mixed region, but below 500m, the model underestimates observations by as much as 40%, in agreement with the model comparison to surface observations. The vertical gradient of CO near the surface in CMAQ is much smaller than observations.

In the afternoon, convective mixing transports CO aloft from the surface. The afternoon observed median CO concentration above 500 m increases uniformly by ∼25 ppbv relative to the morning; the observed median concentration at the surface decreases by ∼50 ppbv (Figure 4.8). Although the observed and modeled PBL height (inferred from the observed temperature profiles) is generally ∼1,500 m, observations show that CO is moderately well mixed from 500 to 2400 m, but poorly mixed below 500 m; there is a parcel of CO rich air below 500 m with a concentration of ∼350 ppbv, which agrees with the surface monitors. In general, the aircraft observations are close enough to a CO source (motor vehicle emissions) and the rate of convective mixing is slow enough such that pollutants are not mixed

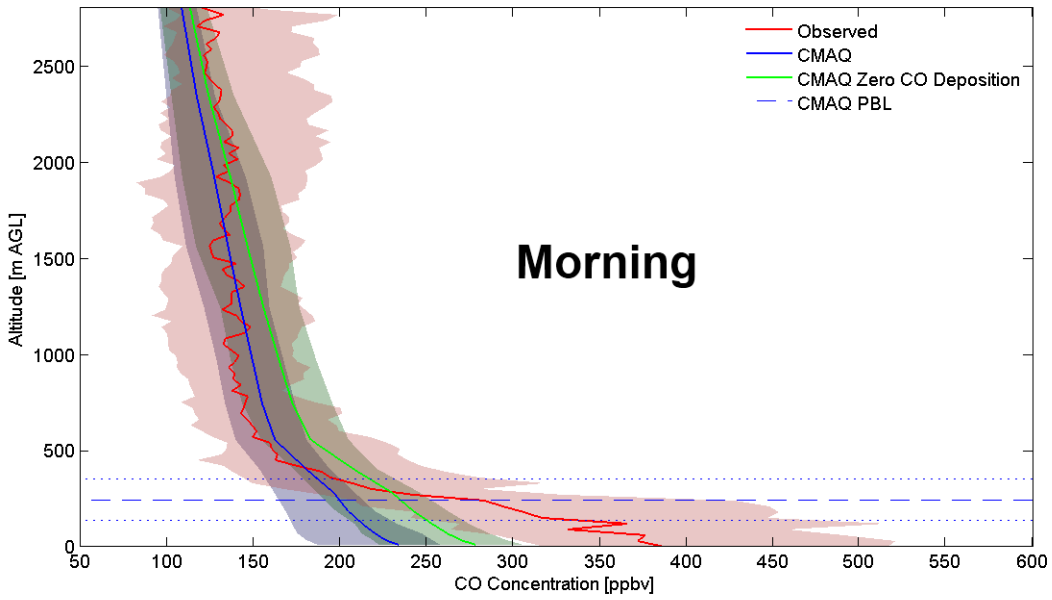

Figure 4.7: Comparison of observed (red) and modeled morning CO vertical profiles paired in time and space. The solid lines are the medians, and the shaded areas represent the 25th and 75th quartiles of the data. The blue line corresponds to modeled CO with the deposition velocity calculated in MCIP v3.4.1, and the green line corresponds to modeled CO with the deposition velocity set to zero. The total CO column below 1000 m is closer to observations when the CO deposition velocity is set to zero, but the shape of the vertical profile does not change.

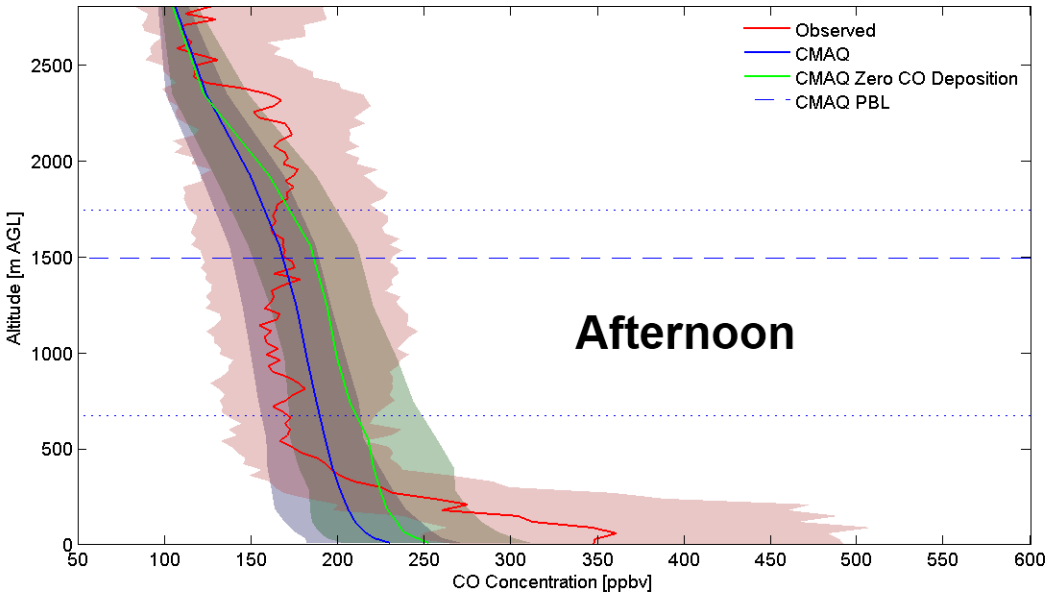

Figure 4.8: Comparison of observed (red) and modeled afternoon CO vertical profiles paired in time and space. The solid lines are the medians, and the shaded areas represent the quartiles of the data. The blue line corresponds to model CO with the deposition velocity calculated in MCIP v3.4.1, and the green line corresponds to modeled CO with the deposition velocity set to zero.

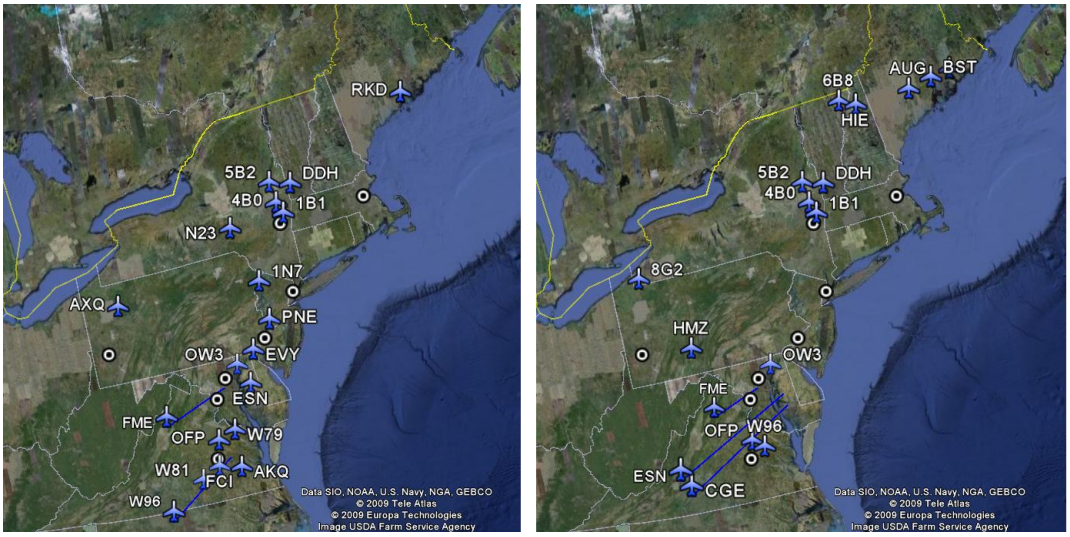

Figure 4.9: Map of the locations of profiles with poorly mixed air near the surface (left; 51 spirals), and profiles with well mixed air throughout the boundary layer (right; 21 spirals), with corresponding airport codes.

throughout the boundary layer. However, this is not true for all of the observations. It is possible to group the afternoon CO profiles based on the ratio of the maximum CO concentration below 500 m and the median CO concentration above 500 m. A ratio of 1.5 describes a profile with poorly mixed air below 500 m, and well mixed air above. A ratio less than 1.5 describes a profile with well mixed air from the surface to the top of the profile. The first group contained 51 profiles, and the second group contained 21 profiles (Figure 4.9 , 4.10 & 4.11).

The locations of the two groups of spirals are shown in Figure 4.9. Each spiral shape is not limited to a specific geographical location. A stratified and a well-mixed spiral can occur at the same location on two consecutive days; the shape of the spiral is dependent on the prevailing dynamic conditions. The model predicts the same profile shape for both groups: CO well mixed throughout the boundary

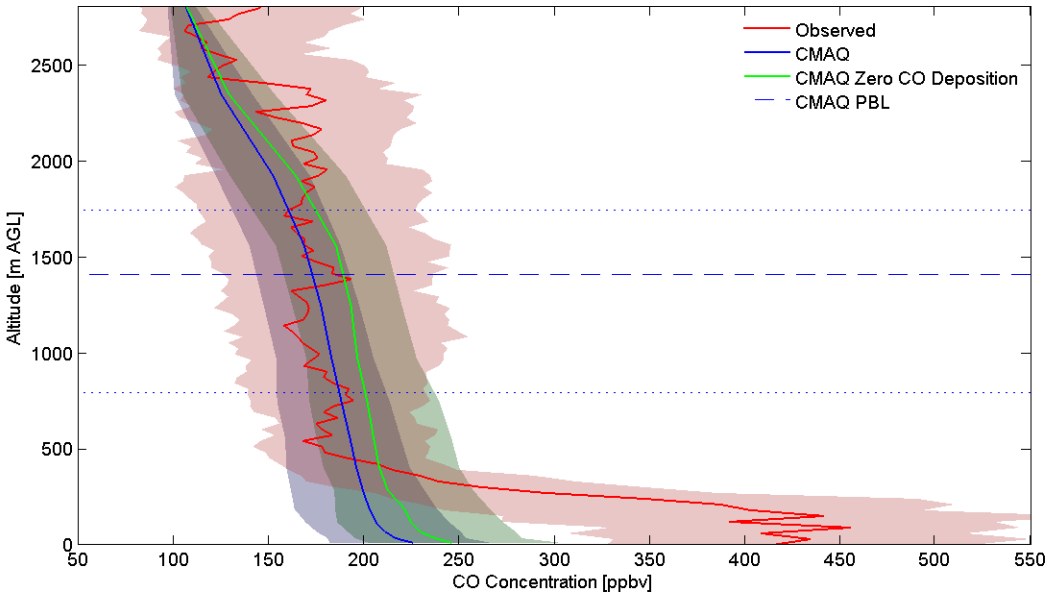

Figure 4.10: Comparison of observed (red) and modeled afternoon CO vertical profiles when air near the surface is poorly mixed. The solid lines are the medians, and the shaded areas represent the quartiles of the data. The blue line corresponds to model CO with the deposition velocity calculated in MCIP v3.4.1, and the green line corresponds to modeled CO with the deposition velocity set to zero.

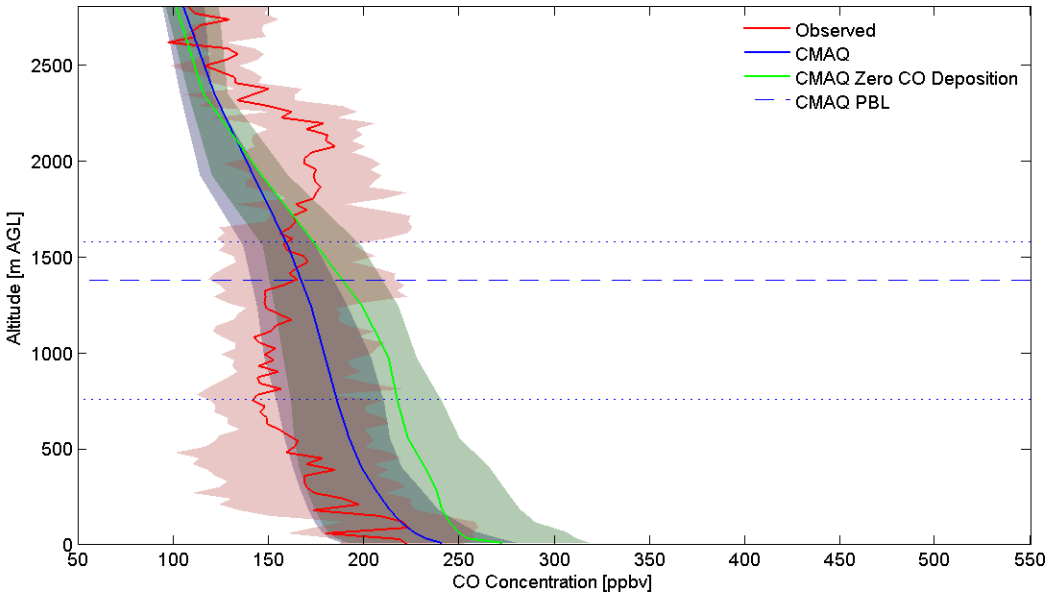

Figure 4.11: Comparison of observed (red) and modeled afternoon CO vertical profiles when the boundary layer is well mixed throughout. The solid lines are the medians, and the shaded areas represent the quartiles of the data. The blue line corresponds to model CO with the deposition velocity calculated in MCIP v3.4.1, and the green line corresponds to modeled CO with the deposition velocity set to zero.

layer. When the observed spiral is stratified, the model tends to underestimate the CO concentration in the CO rich plume below ∼300 m by ∼50%, in agreement with the surface observations (Figure 4.10). In the well mixed region of the profile, between ∼300-1700 m, the model is generally in agreement with observations. When the observed spiral is well mixed throughout the boundary layer, the model overestimates CO by ∼30% from the surface to ∼1,500 m (Figure 4.11). Between ∼1700 m and ∼2400 m, the model underestimates CO by ∼10% when the CO profile is stratified, and ∼20% when the CO profile is well mixed.

The CO total column (the mass of CO integrated over the height of the spiral) of all the flights is underestimated in the model on average by 10% (Figure 4.12). In the morning and afternoon, the average CO total column is underestimated by 15% and 7%, respectively. The bias in the afternoon total column is relatively low because of compensating errors in the two subgroups of spirals. The CO total column of spirals with poorly mixed air near the surface is underestimated by 14%, but for well mixed profiles the CO total column is overestimated by 15%. On these days, the CO emissions inventory may be overestimated. Another possibility that correlates with underestimated CO concentrations between 1700-2400 m, is an underestimated loss of pollutants to the free troposphere from boundary layer venting by convection. High-resolution simulations of dynamics over urban areas have been able to replicate these thermals (Zhang, et al., 2009). Perhaps the horizontal and vertical resolution of this simulation is too coarse to adequately capture these processes.

To further investigate the CO emissions inventory, the CO total column upwind and downwind of cities was compared. Vertical profiles were considered upwind

Date	City	Observed [DU]	MCIP3.4.1 [DU]	CO $v_d = 0$ [DU]
5/24	DC/Baltimore	-0.3	8.9	9.9
6/09	DC/Baltimore	-3.5	7.0	7.3
6/24	DC/Baltimore	18.8	7.6	8.0
6/10	Richmond	3.0	5.4	3.7
6/11	Richmond	8.0	2.7	2.8
7/16	Richmond	18.4	5.6	6.0
8/14	Bangor, Maine	1.4	5.0	6.9

Table 4.1: Comparison of observed and modeled change in total CO between downwind and upwind vertical profiles.

and downwind if the location was in the vicinity of the 12-hour backward and forward trajectories from the city, respectively. Three sets of upwind and downwind profiles were found around both Washington, DC/Baltmore and Richmond. One set of upwind and downwind profiles was found around Bangor, Maine. The differences between the average upwind total CO and downwind total CO are shown in Table 4.1. The model always predicts an increase in total CO between upwind and downwind locations. Thus, when a decrease in total CO is observed, the model disagrees with observations. When an increase in total CO is observed, the model tends to under predict the change in DC/Baltimore and Richmond, but over predicts the change in Bangor. An analysis of several model years may be necessary to make a decisive conclusion with respect to the model performance of the change in upwind and downwind total CO.

In the morning and afternoon when there is CO rich air near the surface, three factors could cause the model to underestimate CO concentrations: 1) the sink for CO (dry deposition) is too fast, 2) the CO boundary conditions are significantly

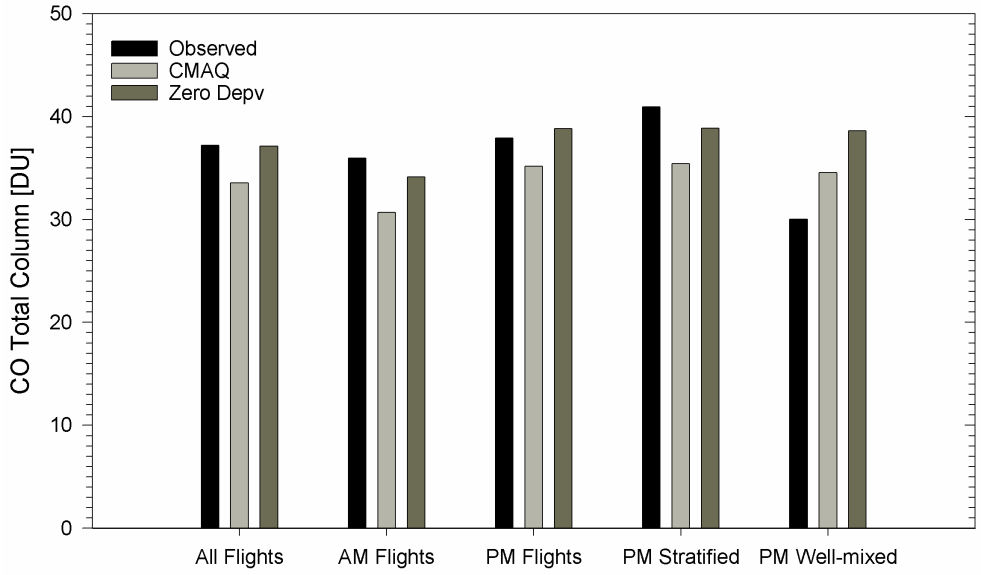

Figure 4.12: Comparison of the average observed (black) and modeled CO total column for all flights, morning flights (AM Flights), and afternoon flights (PM Flights). The afternoon flights are further subdivided into two groups based on the shape of the observed CO vertical profile: profiles with CO rich air near the surface (PM Stratified group), and 2) profiles with a well-mixed boundary layer (PM Well-mixed group). The light gray corresponds to the modeled CO total column with the deposition velocity calculated in MCIP v3.4.1, and the dark gray bar corresponds to the modeled CO with the deposition velocity set to zero.

underestimated, 3) the source of CO at the surface (motor vehicle emissions) is not strong enough, and/or 4) CO is mixed away from the surface too quickly.

In the model, the default daily average deposition velocity is 0.08-0.16 cm/s, while observations of CO deposition velocity are in the range of 0-0.07 cm/s (Figure 4.13 & Table 4.2). Thus, the rate of CO loss to the surface may be overestimated.

Because the CMAQ boundary conditions are extracted by embedding the modeling domain within a larger domain with a coarser grid, the boundary conditions vary in time and space. In general, in the Northwest section of the domain, the CO boundary condition is 100-140 ppbv, close to the continental background level. However, boundary conditions in the Southeast of the domain can fall below 100 ppbv. Underestimated CO boundary conditions will play a role in the low bias of the CO total column, but will not affect the shape of the vertical profile such as to bring it into agreement with observations.

When the surface sink was removed by setting the CO deposition velocity to zero and the model is rerun, the concentration of CO in the morning increases by 20-40 ppbv below 500 m, and 10-15 ppbv above 500 m. The shape of the CO morning vertical profile does not change by much, but the total column increases. The morning CO total column is 5% less than observations. A similar change occurs in the afternoon. The concentration of CO increases by 10-15 ppbv throughout the boundary layer, and the shape of the spiral stays the same. The CO total column for afternoon flights where CO is poorly mixed near the surface is within 5% of observations. The CO total column for well mixed vertical profiles is overestimated by 29%.

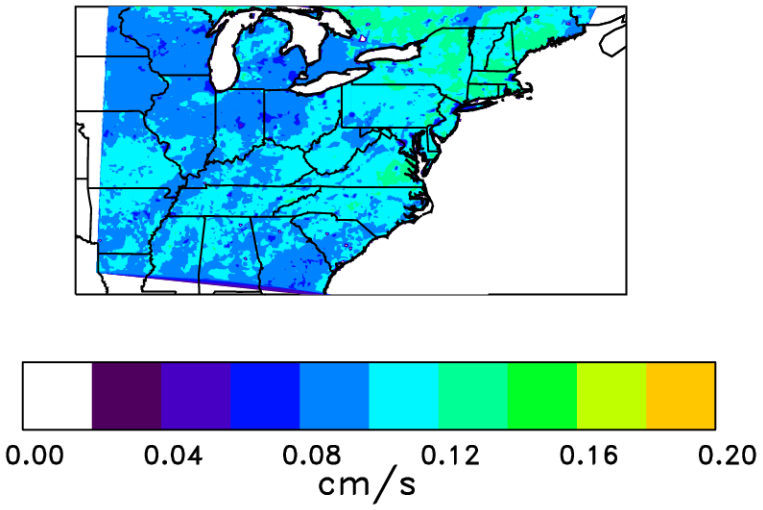

Figure 4.13: Modeled daily average CO deposition velocity in cm/s.

In general, the trend in the modeled CO vertical profiles after changing the CO deposition velocity is similar to the trend in CO concentration at the surface monitoring sites. The median surface CO concentration increases by ∼10% in the morning and at night, but the daytime CO concentration is not significantly affected. During the morning rush hour, the model now overestimates CO.

In order to reconcile the observed CO total column with the model, it appears local CO motor vehicles emissions in the model should be reduced by 10-20%, the CO boundary conditions should be increased by 10-20%, and the CO deposition velocity should be nearly zero.

Site	Vegetation	$v_d(cms^-1)$	Reference
Darmstadt, Germany	deciduous forest	0.027 - 0.038	Sanhueza et al., 1998
Guri, Venezuela	grassland/ savannah	0.02 - 0.03	Scharffe et al., 1990
Transvaal, South Africa	savannah	0.05	Conrad and Seiler, 1985
Andalusia, Spain	unplanted field	0.01 - 0.04	Conrad and Seiler, 1985
Mainz, Germany	grass/small plants	0.03	Conrad and Seiler, 1980, 1985
Bush, Scotland	grassland/arable field/ deciduous forest	0.001 - 0.002	Moxley and Smith, 1998
St. Anicet, Canada	grass/mixed woods	0.00-0.40	Constant, et al., 2008
Tsukuba, Japan	unplanted field/ arable field/ deciduous forest	0.00 - 0.07	Yonemura et al., 1999, 2000

Table 4.2: Summary of published observations of CO deposition velocity over various types of vegetation.

4.5 Conclusions

Modeled and observed CO total columns are generally in agreement within the combined uncertainty. For the majority of the observed vertical profiles, the CO total column is underestimated by ∼10%. For the rest of the observations, the CO total column is overestimated by ∼10%. Comparison of modeled and observed CO deposition velocities show that the surface sink of CO is likely overestimated by as much as a factor of ∼2, and boundary conditions are underestimated by ∼10-20%. There is little evidence that the CO emissions inventory is grossly overestimated, as suggest by Parrish, (2006), Warneke, et al., (2006), and Hudman, et al., (2008). One reason for the disagreement with these studies may be that the observations considered in Parrish, (2006) probably do not include CO emissions enrichment events like cold starts or vehicles traveling under high load.

Under the configuration where CO does not dry deposit, the total column of CO is within 5-6% of observations. CO concentrations continue to be underestimated near the surface because the vertical profile shape remains well mixed. The additional CO at the surface as a result of removing the surface sink is redistributed throughout the column by the model. CMAQ appears to be transporting CO away from the surface more quickly than what is observed. At higher altitudes, above the modeled and observed PBL, the model underestimates CO concentrations by 10-15%, suggesting that boundary layer venting by deep convection is underestimated in the model.

Chapter 5

Analysis of CMAQ Turbulent Vertical Mixing

5.1 Introduction

Capturing the morning buildup of pollutants in the shallow nocturnal boundary layer is important for replicating the morning burst of ozone, and nighttime surface removal processes. However, model performance studies have shown that CMAQ consistently over predicts the nighttime/early morning ozone minimum (e.g., Appel, et al., 2007, Godowitch, et al., 2008). Several factors affect the morning concentration of ozone including the temporal distribution of emissions and nighttime chemistry and dynamics. If these processes do not occur in the model at the correct rates, the imbalance of creation and destruction of ozone leads to model bias.

Nighttime vertical mixing processes also play an important role in the long-range transport of pollutants. In the shallow nocturnal boundary layer, formed by a thermal inversion, surface winds are typically stagnant. The dominant vertical transport mechanism is turbulent mixing as a result of shear stress at the surface. Above the nocturnal boundary layer, winds speeds can be much higher, which horizontally transport pollutants long distances. Because the residual layer is decoupled from the surface by the thermal inversion, ozone and its precursors in this layer are unaffected by surface removal processes, increasing their lifetime.

After sunrise, the boundary layer quickly rises to the full height of the sub-

sidence inversion. Thermal fluctuations mix pollutants throughout the boundary layer, and updrafts below convective clouds can transport pollutants out of the boundary layer. Local pollutants that have built up near the surface mix with the pollutants that have been horizontally transported through the night in the residual layer. This morning injection of ozone and precursors plays a significant role in causing high ozone concentrations later in the day, and makes ozone a regional pollutant that is a function of a mixture of local and regional precursor sources (Baumann, et al., 2000, Schichtel and Husar, 2001, Vukovich and Scarborough, 2005, Ryan, et al., 1998).

CMAQ utilizes two processes to represent boundary layer vertical mixing processes. Large eddy convective mixing is represented by an asymmetric convective mixing scheme, where pollutants can be transported upward non-locally (between non-adjacent layers), while downward mixing is layer-by-layer subsidence. All other vertical mixing processes are represented with K-theory, where turbulent transport is modeled using an eddy diffusion coefficient (K_Z, m^2/s), analogous to molecular diffusivity (5.1).

$$\left.\frac{\partial c_i}{\partial t}\right|_{VDIFF} = \frac{\partial}{\partial z} K_z \frac{\partial c_i}{\partial z} \tag{5.1}$$

K_Z is calculated using PBL similarity theory based on the formulations in Businger, et al. (1971) and Hass, et al. (1991). Similarity theory is a method by which dimensionless groups are fitted to an empirical equation. A generalized expression can be derived for K_Z by considering two-dimensional turbulent flow over a flat surface with mean velocity . The vertical shear stress (τ_z) at the surface can

be written as:

$$\tau_z = \rho K_z \frac{\partial \bar{u}}{\partial z} \tag{5.2}$$

where ρ is the density of air. When similarity theory is applied to the average velocity profile (Middleman, 1998, Jacobson, 2005):

$$\bar{u} = \frac{u_*}{k} ls \left(\frac{z}{z_0} \right) \tag{5.3}$$

where z_0 is the height at which the average velocity extrapolates to zero, u_* is the friction velocity defined as $\sqrt{\frac{\tau_z}{\rho}}$, and k is the empirically-derived Von Karman constant. For atmospheric applications, a value of k equal to 0.40 is used.

In order to account for the production of turbulence as a result of buoyancy, the mean velocity profile is scaled by an empirical profile function ϕ_h that depends on atmospheric stability in the following manner:

$$\phi_h = \begin{cases} 0.97 + 7.8\frac{z}{L} & \text{stable} \\ 0.95(1 - 11.6\frac{z}{L}) & \text{unstable} \\ 0.95 & \text{neutral} \end{cases} \tag{5.4}$$

The constant L is a length scale called the Monin-Obukhov length, and is proportional to the height above the surface at which production of turbulence from buoyancy dominates turbulence as a result of shear.

$$L \propto u_*^2 \frac{\theta(z)}{\theta(z) - \theta(z_0)} \tag{5.5}$$

In Eq. 5., $\theta(z)$ is the average potential temperature, which is the temperature an air parcel at temperature, T, and pressure, p, would acquire if it were dry adiabatically compressed to the surface pressure (p_0).

$$\theta = T \left(\frac{p}{p_0} \right)^{R/C_p} \tag{5.6}$$

Taking the derivative of 5.3, substituting into 5.2, rearranging, and dividing by ϕ_h yields the following expression for K_Z:

$$K_z = \frac{ku_* z}{\phi_h} \tag{5.7}$$

When similarity theory is applied to the mixed layer, K_Z is parameterized by:

$$K_z = \frac{ku_* z\left(1 - \frac{z}{h}\right)^{3/2}}{\phi_h} \tag{5.8}$$

$$K_z = kw_* z\left(1 - \frac{z}{h}\right) \tag{5.9}$$

where h is the height of the PBL and w_* is the convective velocity proportional to the vertical flux in potential temperature (Byun, et al., 1999).

In CMAQ, a minimum K_Z is established in order to maintain a certain amount of mixing. In earlier versions of CMAQ (versions before 4.5.1), the minimum K_Z was set to 1 m^2/s in order to avoid `unrealistically high concentrations of primary speciesin areas of high emissions (e.g., urban areas)" (Community Modeling and Analysis System (CMAS), 2005). In version 4.5.1 of CMAQ, the minimum K_Z is allowed to vary between 0.5 m^2/s and 2 m^2/s according to the following function:

$$K_z min = 0.5(1 - F_{urban}) + 2.0F_{urban} \tag{5.10}$$

where F_{urban} is the fractional urban land use in a grid cell. The $K_Z$min is scaled with F_{urban} in order to account for subgrid scale obstacles in urban areas and the urban heat island effect, which increase turbulence. However, in micrometeorological studies over many rural surface types a minimum K_Z in the range of 0-0.1 m^2/s was observed (Wesely, et al., 1985, Gallagher, et al., 2002 and references therein,

Constant, et al., 2008). The CMAQ $K_Z$min value may be somewhat high. The results presented in Chapter 4 also demonstrate that CMAQ appears to be vertically mixing pollutants too quickly below 1000 m. Several studies comparing K_Z parameterizations have found the schemes that predict smaller K_Z had better skill at reproducing ozone and its precursors at the surface and aloft (Nowacki, et al., 1996, Byun, et al., 2007, Han, et al., 2009).

An overestimation of $K_Z$min will have the greatest effect on vertical mixing at night where conditions are stagnant. If nighttime modeled turbulent vertical mixing occurs too quickly, NO_X concentrations will be diluted at the surface. This reduces the local temporary loss of ozone, which occurs through titration with NO.

In this chapter, I will present a comparison of model performance of a base case simulation with the default $K_Z$min lower limit of 0.5 m^2/s, and a slower turbulent mixing case with a $K_Z$min lower limit of 0.1 m^2/s. By decreasing the $K_Z$min to 0.1 m^2/s, the time required to mix pollutants from the surface to 100 m solely by eddy diffusion increases from 5.5 hours to 28 hours. I will evaluate the simulations with surface observations of CO, O_3, and NO_X at AQS and CASTNET sites, as well as vertical profiles of CO and O_3.

5.2 Modeling Set-up

The modeling domain, meteorology, emissions, and AQM set-up described in Chapter 4 was used. The deposition velocity of CO was set to zero in both cases in order to differentiate between the ambiguity of errors in the loss rate of CO and

changes in CO mixing. The effect the longer CO lifetime on ozone chemistry is small (less that 0.1 ppbv). A sensitivity simulation with the lower limit of $K_Z$min set to 0.1 m^2/s was performed, and compared to the simulation with the default $K_Z$min lower limit of 0.5 m^2/s. The former will be referred to as the 0.1 $K_Z$min case, and the latter the 0.5 $K_Z$min case. A twelve-week episode starting on May 15, 2002 and ending on August 15, 2002 was evaluated. The model was initiated on May 1, 2002, but the first two weeks were taken as spin-up.

5.3 Observed CO and O_3 Vertical Profiles

Model results were compared to 39 observed morning (7-10 AM local time) vertical profiles of CO and O_3 at 19 small airports across the Northeast US (Figure 4.2). The data were measured for the RAMMPP project in the summer of 2002 as described in Chapter 4. The morning profiles were selected because mixing as a result of the eddy diffusion mechanism is more significant in the morning. As the sun rises, thermal convection becomes the dominant mixing mechanism. CO measurements were taken with a modified Thermo Scientific CO infrared filter correlation analyzer (Model 43C, Franklin, MA) (Dickerson and Delany 1988), and O_3 measurements were taken with a Thermo Scientific UV photometric analyzer (Model 49, Franklin, MA).

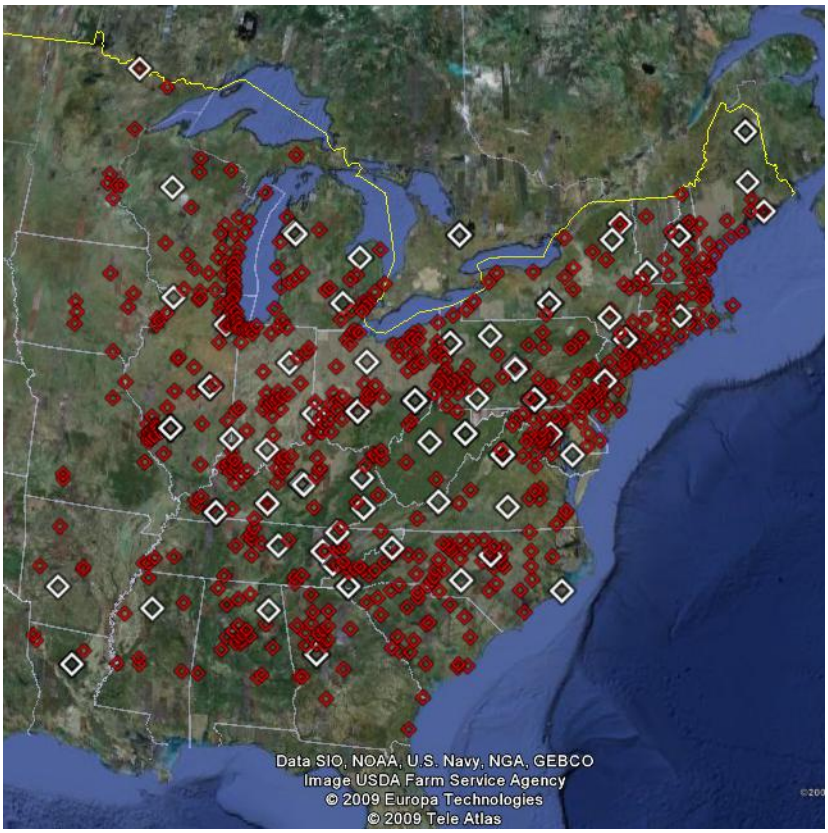

Figure 5.1: Map of surface AQS (red) and CASTNET (white) O_3 monitoring locations.

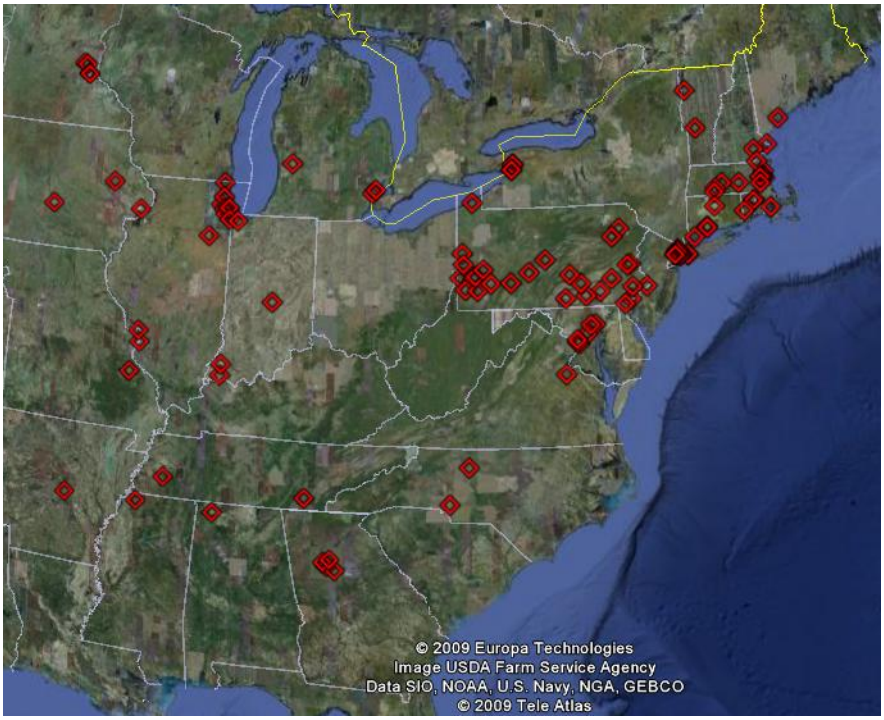

Figure 5.2: Map of surface AQS NO_X monitoring locations.

5.4 Surface Observations of CO, O_3, and NO_X

Ozone surface monitoring data were extracted from the EPA's AQS and CASTNET monitoring network databases at 612 and 85 sites, respectively shown in Figure 5.1. CO surface monitoring data were extracted from the AQS monitoring network database at ten sites discussed in Chapter 4, where CO measurement precision was at the ppbv level (Figure 4.4). NO_X surface monitoring data were extracted from the AQS monitoring network database at 92 sites (Figure 5.2).

5.5 Results and Discussion: CMAQ Model Performance for $K_Z$min = 0.5 m^2/s and 0.1 m^2/s

5.5.1 Model Comparison to AQS and CASNET O_3 Surface Observations

Significant improvement in hourly ozone model performance at AQS and CASTNET monitoring sites occur with the 0.1 $K_Z$min case during the hours of midnight to 6 AM and 9-11 PM local time (Figure 5.3). It consistently captures the daily ozone minimum and subsequent rapid ozone formation (Figure 5.4). Thus, afternoon ozone has a larger component formed as a result of morning chemistry rather than ozone that is conserved from the night before. From 7AM to 8 PM there is no discernable change.

Observations at AQS locations where were split into urban (324 monitors) and rural (288 monitors) groups. A grid cell was considered urban if the population was

	slope	y-intercept	R^2
Rural Monitors 0.5 $K_Z$min	0.50	20.1	0.48
Rural Monitors 0.1 $K_Z$min	0.58	14.2	0.52
Urban Monitors 0.5 $K_Z$min	0.64	13.4	0.53
Rural Monitors 0.1 $K_Z$min	0.69	9.7	0.55

Table 5.1: Linear least squares fit to a scatter plot of observed and modeled ozone at urban and rural monitoring sites.

greater than 114 people/km^2 according to 2000 census date. With slower turbulent mixing the model is better correlated with observations (Table 5.1). The greatest effect was at rural sites, where turbulence is generally lower. The slope of the linear least squares fit to a scatter plot of the data increased from 0.50 to 0.58, and the y-intercept decreased from 20 ppbv to 14 ppbv when $K_Z$min was decreased.

5.5.2 Model Comparison to AQS O_3 and NO_X Surface Observations

Observations were compared to the model at AQS locations where both O_3 and NO_X were monitored, at urban (70 monitors) and rural (20 monitors) locations. At rural sites, the high bias in ozone at night and in the early morning goes down by 5-6 ppbv (Figure 5.5). This is correlated with a 25-35% increase in NO_X concentration, and a decrease in the NO_X negative bias, but no change in the concentration of NO (Figure 5.5 & 5.6). The decrease in ozone concentration at night at these sites is driven by titration with NO. Even with this improvement in the bias of NO_X, the model still significantly underestimates NO_X concentrations at night. Some of this bias may be driven by uncertainties in other processes that regulate the availability

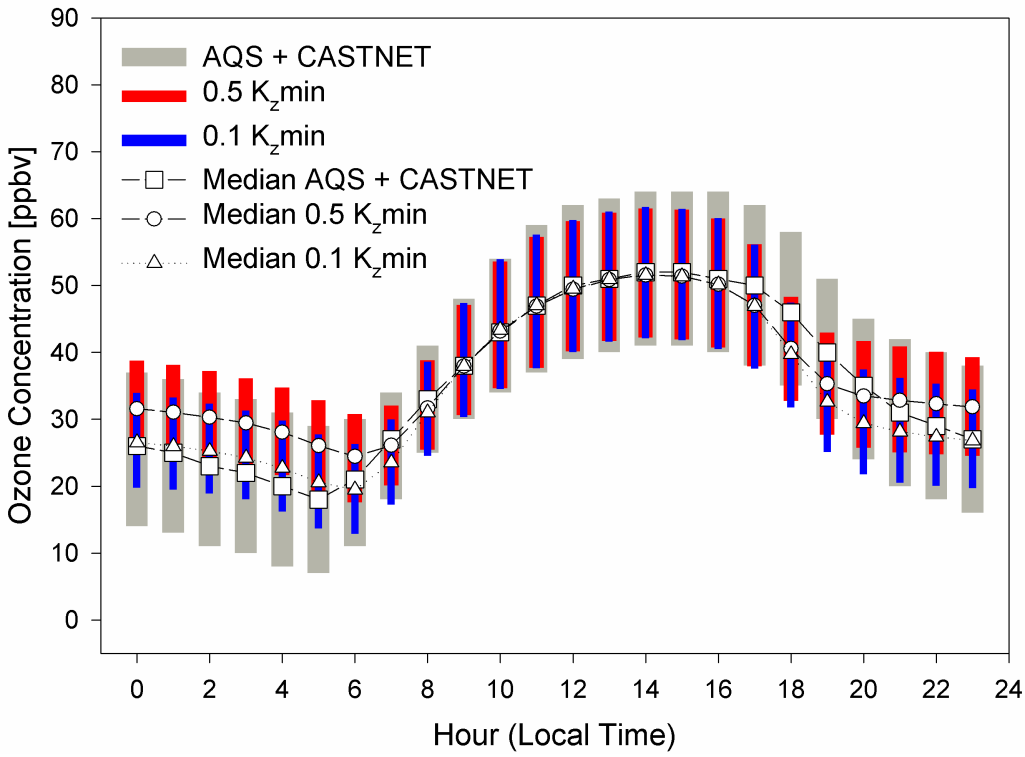

Figure 5.3: Medians (black markers) and quartiles (shaded boxes) of observed (gray, squares) and modeled hourly ozone. The red boxes and black circles correspond to the 0.5 $K_Z$min case and the blue boxes and black triangles correspond to the 0.1 $K_Z$min case. Significant improvement in morning model performance occurs when mixing is slowed down.

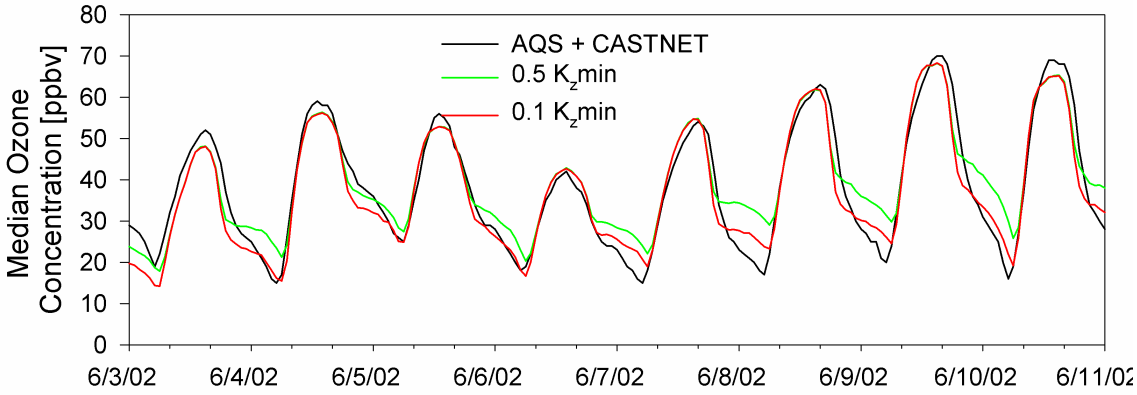

Figure 5.4: Timeseries of the observed (black) and modeled (green, 0.5 $K_Z$min; red, 0.1 $K_Z$min) median O_3 concentrations at all AQS and CASTNET monitoring sites for one week. Results are typical for the length of the simulation.

of NO_X, like the loss of N_2O_5 to aerosols (Brown, et al., 2006, Bertram and Thornton, 2009) .

At urban monitoring sites, the positive bias in ozone from 0-5 AM decreases, but the low bias from 6-7 AM and 5-11 PM increases. The NO_X positive bias in general increases at night and in the early morning (Figure 5.7).

From midnight to 5 AM, when the model performance of ozone improves, the bias in NO is negative and does not change when the $K_Z$min changes (Figure 5.8). Therefore the model overestimates the NO_2 concentration, and underestimates the NO_2 loss rate. Observations of NO, NO_2, and ozone fluxes show that the nighttime NO_2 flux at the surface may scale with the NO_2 concentration squared (Wang, et al., 2003, Horii, et al., 2004). It is speculated that non-linear NO_2 deposition occurs as a result of heterogeneous hydrolysis of NO_2 to HNO_3 and HONO at high NO_2

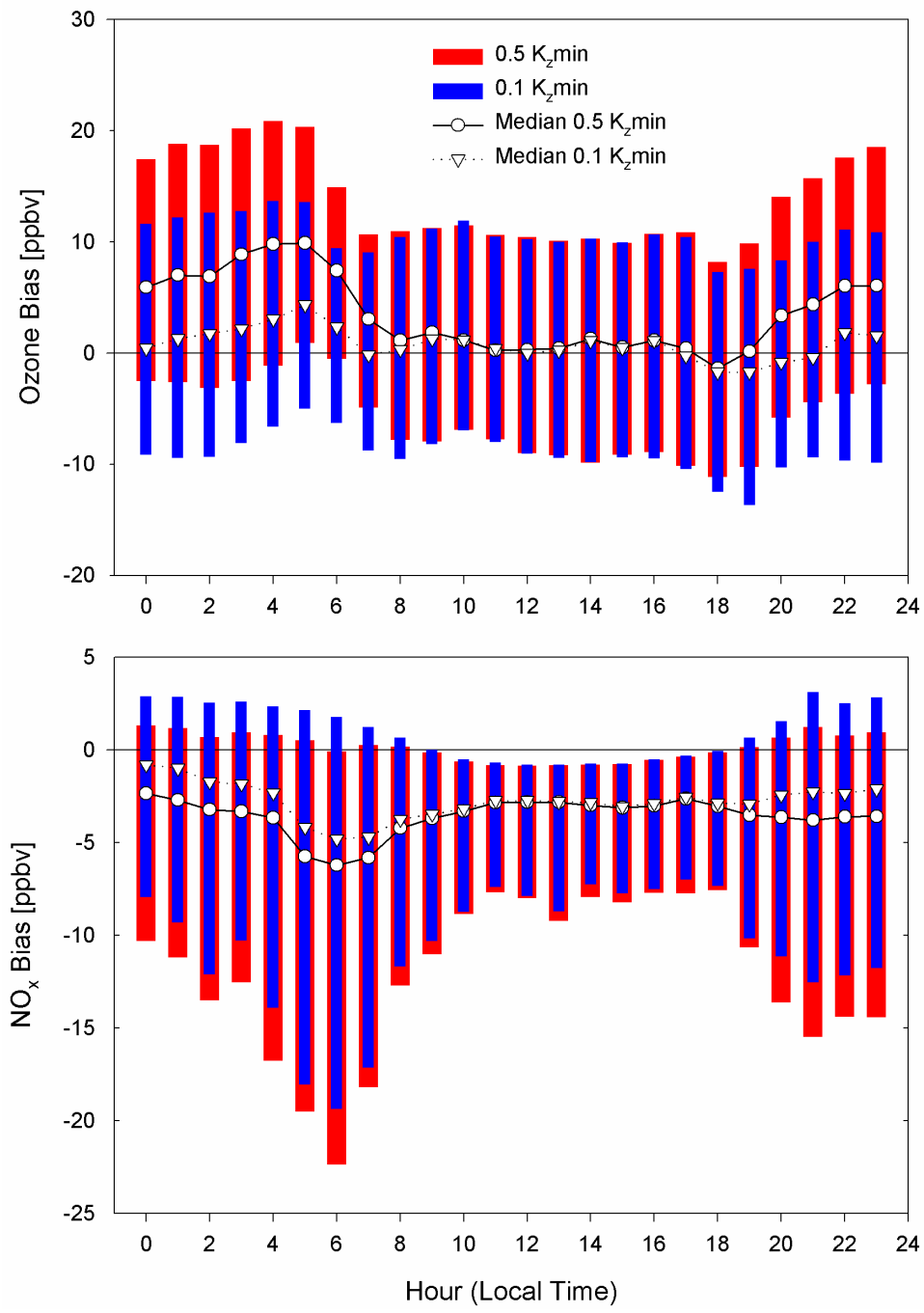

Figure 5.5: Medians (black markers) and quartiles (shaded boxes) of hourly ozone (top) and NO_X (bottom) bias at rural monitoring sites for the 0.5 $K_Z$min (red; circles) and 0.1 $K_Z$min cases (blue; triangles).

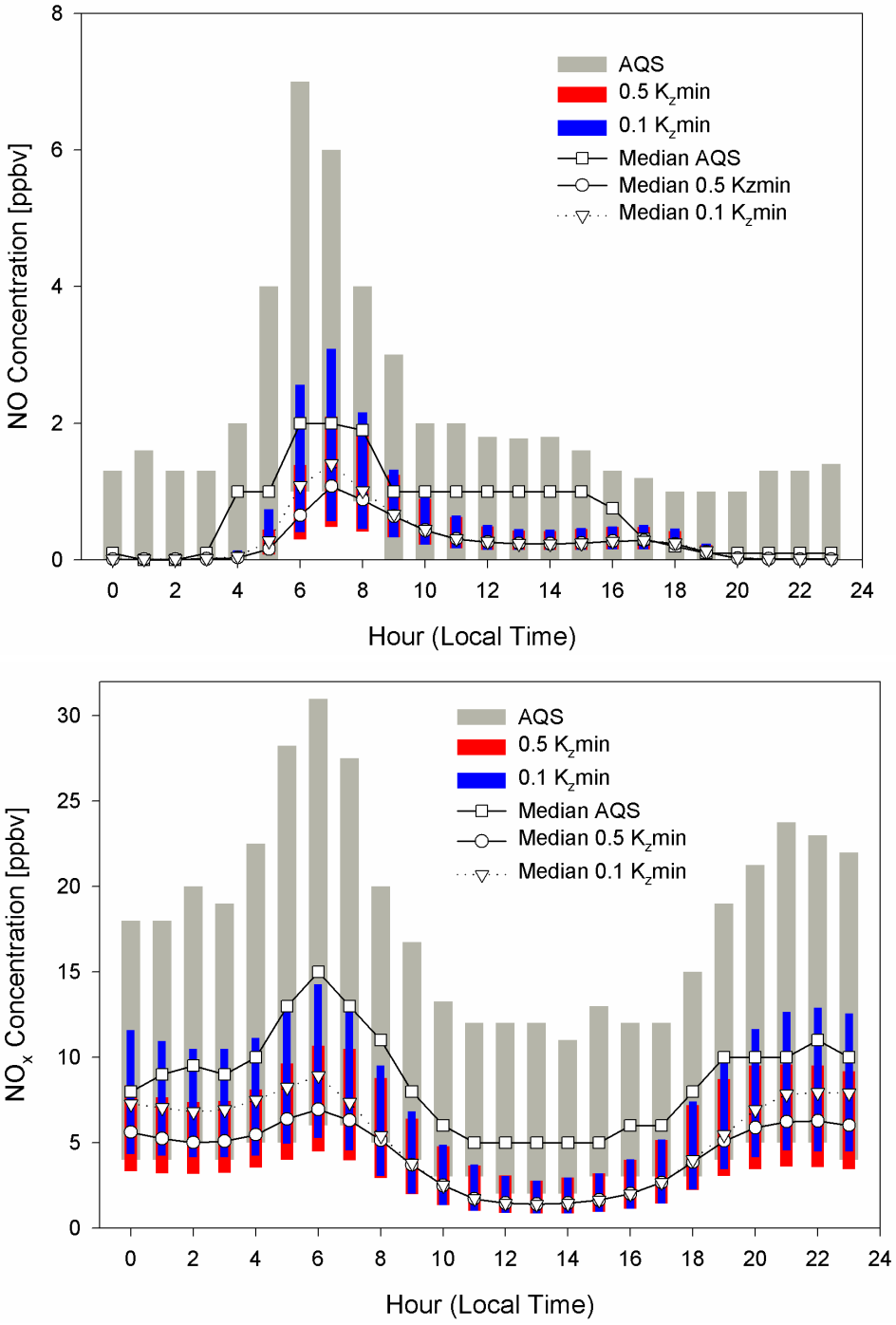

Figure 5.6: Medians (markers) and quartiles (boxes) of observed and modeled hourly NO (top) and NO_X (bottom) in rural areas.

concentrations (>10 ppbv) (5.11). Observations of the nighttime NO_2 deposition velocity varied from 0.2-0.5 cm/s. In the model, the NO_2 deposition velocity at night is less than 0.1 cm/s.

$$2NO_2 + H_2O(Het) \rightarrow HONO + HNO_3 \tag{5.11}$$

An important consequence of this deposition path is that up to half of the nighttime deposited NO_2 would re-emitted to the atmosphere as NO at sunrise, because HONO photolyzes quickly. This nonlinear deposition path is not included in the model, but it may need to be investigated in future updates because the modeled concentration of NO_2 at night exceeds 10 ppbv in both urban and rural areas (Figure 5.6 & 5.9).

In urban areas from 6-7 AM and 5-11 PM local time, the negative bias in ozone in both the 0.5 $K_Z$min and 0.1 $K_Z$min cases is correlated with a positive bias in NO_X (5-10 ppbv) (Figure 5-7). Half of the positive morning bias in NO_X is a result of a positive bias in NO (Figure 5-8). Thus it appears that NO emissions at this time are too high, and excessive loss of ozone through titration with NO has occurred. This agrees with the findings of Kuhns, et al. (2004) and Bishop and Stedman, (2008), which show that NO emissions factors in Mobile6 from light duty gasoline powered vehicles (LDGV) that are between 7-15 years old (36% of the LDGV fleet) are over estimated by 50%.

Concentrating pollutants near the surface with a smaller $K_Z$min has a significant effect on nighttime NO_X dry deposition. Nighttime NO and NO_2 dry deposition

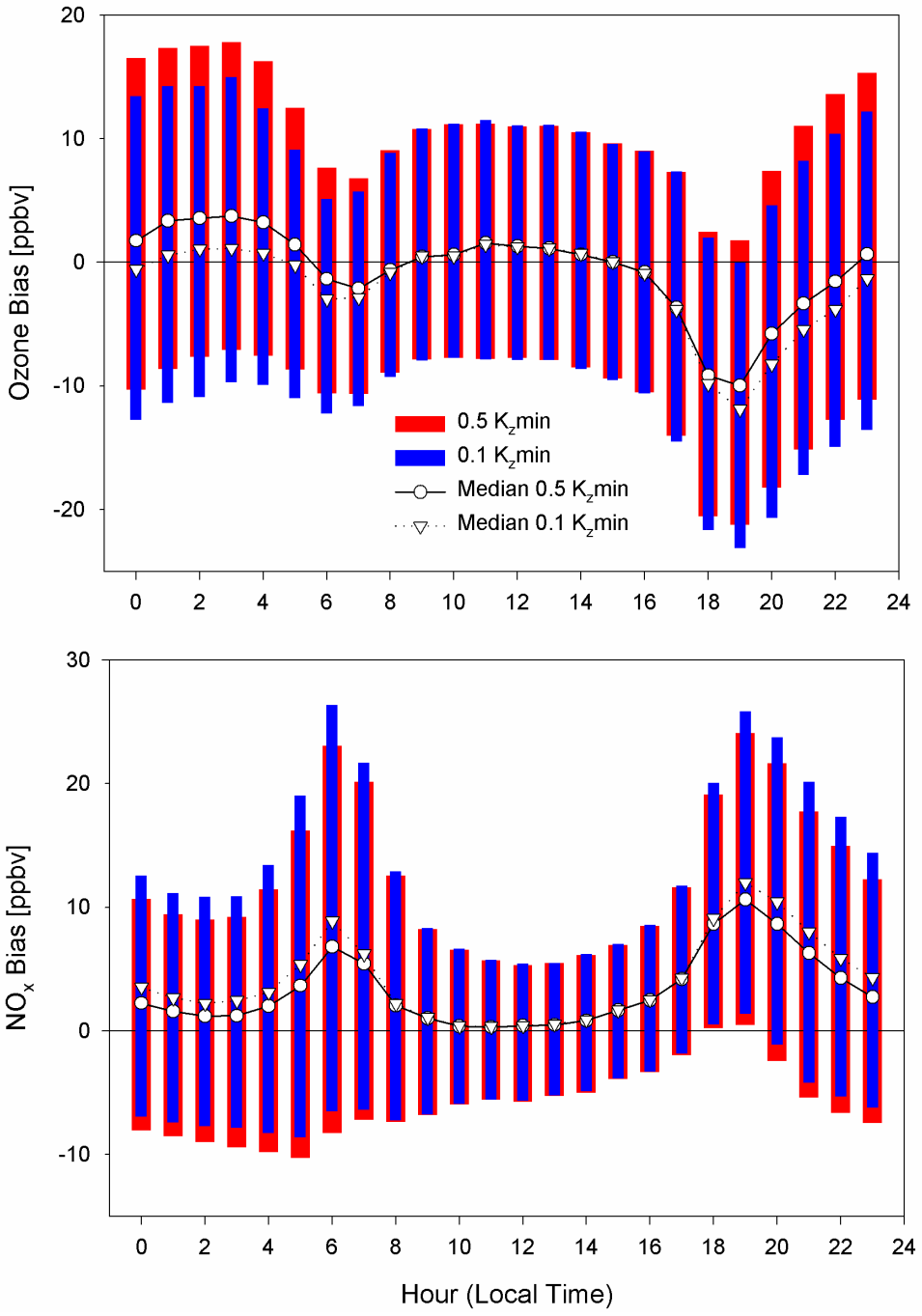

Figure 5.7: Medians (black markers) and quartiles (shaded boxes) of hourly ozone (top) and NO_X (bottom) bias at urban monitoring sites for the 0.5 $K_Z$min (red; circles) and 0.1 $K_Z$min cases (blue; triangles).

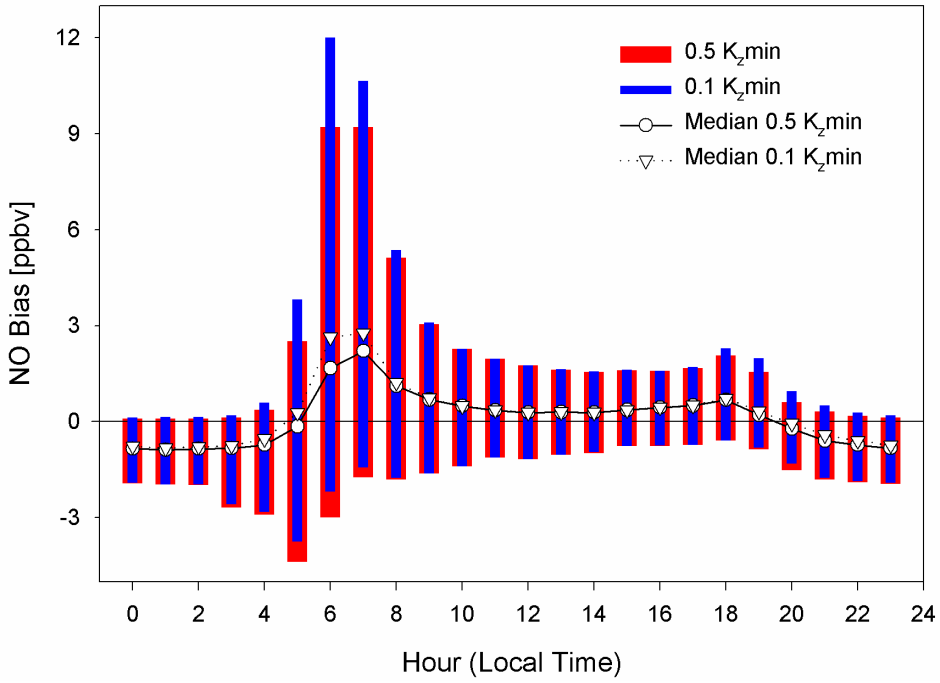

Figure 5.8: Medians (black markers) and quartiles (shaded boxes) of hourly NO bias at urban monitoring sites for the 0.5 $K_Z$min (red; circles) and 0.1 $K_Z$min cases (blue; triangles).

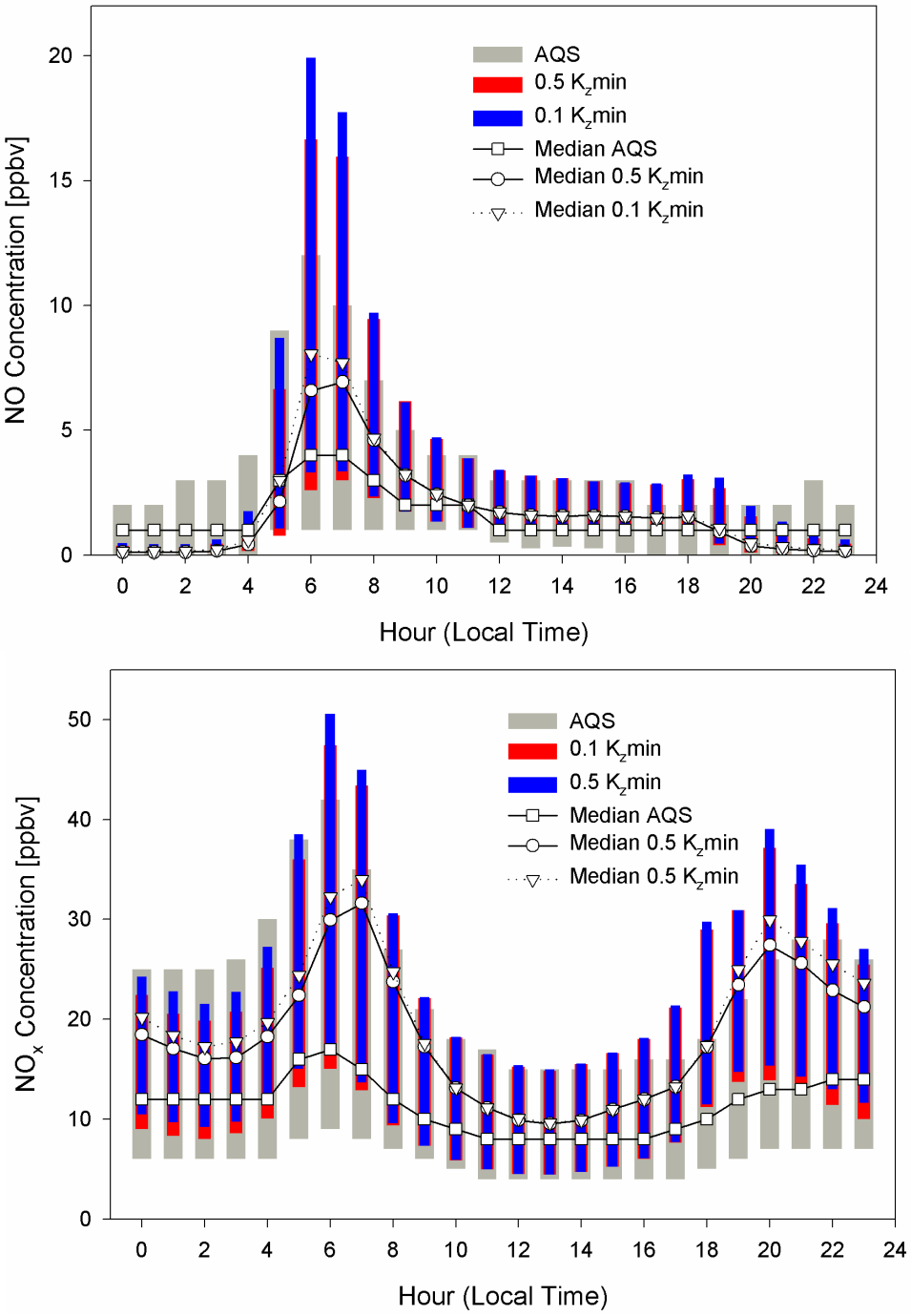

Figure 5.9: Medians (black markers) and quartiles (shaded boxes) of observed (gray, squares) and modeled hourly NO (top) and NO_X (bottom) concentration in urban areas.

increases by 30-70% over most of the domain (Figure 5.10). Reproducing the correct nighttime deposition of NO_X is important for emissions control scenario applications. Because horizontal advection is weak at night, NO_X remaining at the surface will not be transported far away from the source. However, under a slower vertical mixing condition where NO_X deposition increases, fewer NO_X molecules from local sources will be available in the morning to make ozone. NO_X molecules that have been transported from distant sources become more important. If NO_X deposition is underestimated, afternoon ozone will not be apportioned to the correct sources.

5.5.3 Model Comparison to AQS CO Surface Observations

When $K_Z$min is changed to 0.1 m^2/s, the bias in CO concentrations at night and in the early morning generally decreases by 25-40% at night (Figure 5.11). At 6AM, CO concentrations are now over estimated. However, this is expected because, as mentioned in Chapter 4, CO emissions factor for gasoline powered vehicles may overestimated in Mobile6 (Kuhns, et al., 2004, Parrish, 2006, Hudman, et al., 2008).

5.5.4 Model Comparison to Observed CO & O_3 Vertical Profiles

Slowing down vertical turbulent mixing shifts the CO concentration vertical profile in the model closer to observations, but not by enough. The vertical profile shape is not significantly affected by the change in K_Z. Compared to the 0.5 $K_Z$min case, CO concentrations in the 0.1 $K_Z$min case increase by 3% below 250 m (Figure 5.12). These vertical profile observations are taken after sunrise (7-10 AM), when

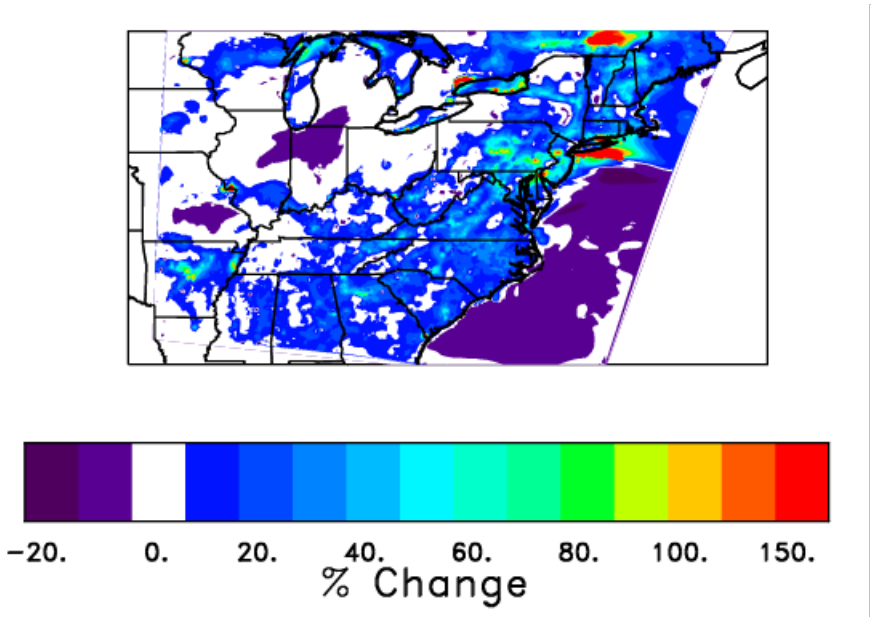

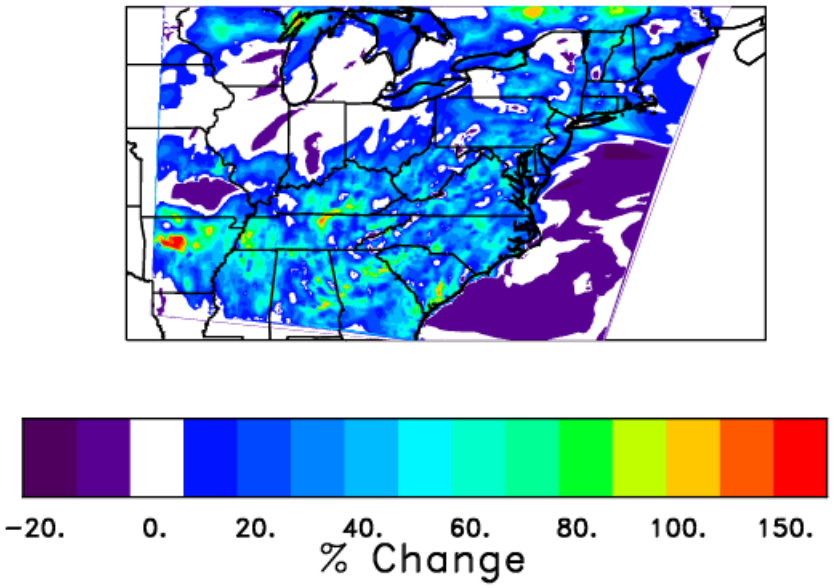

Figure 5.10: Average relative change in nighttime NO (top) and NO_2 (bottom) dry deposition between the 0.5 $K_Z$min and 0.1 $K_Z$min cases.

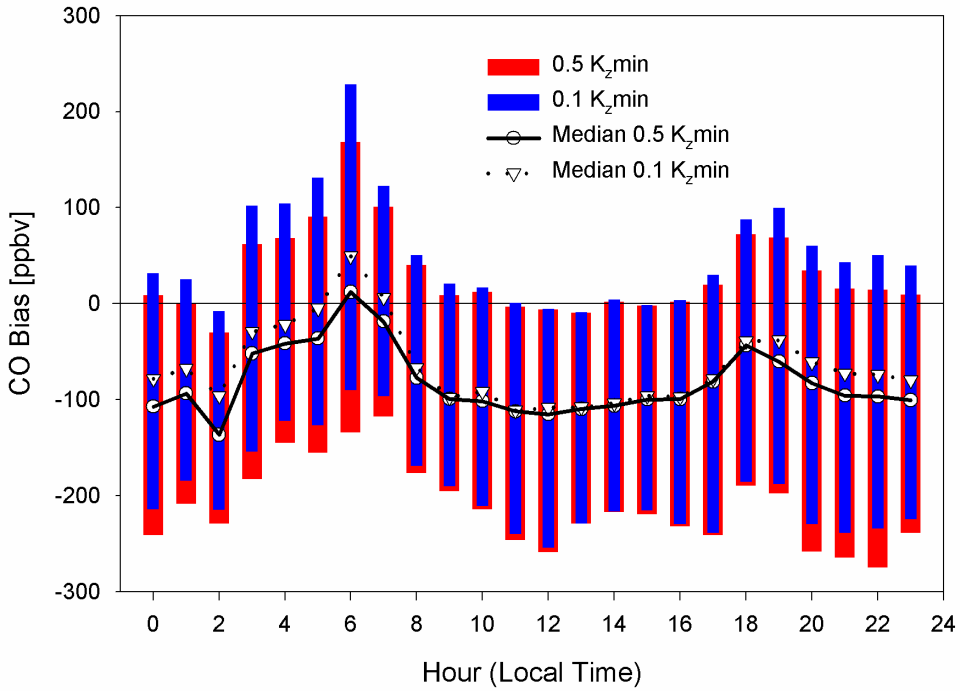

Figure 5.11: Medians (black markers) and quartiles (shaded boxes) of the hourly CO bias at AQS surface monitoring sites for the 0.5 $K_Z$min (red; circles) and 0.1 $K_Z$min cases (blue; triangles).

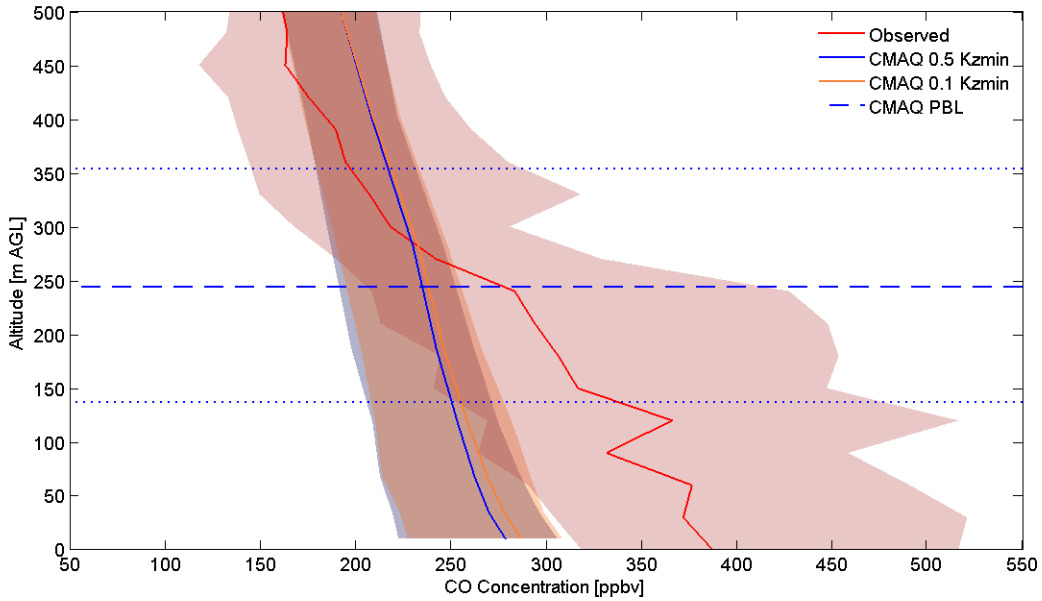

Figure 5.12: Comparison of observed (red) and modeled morning CO vertical profiles. The solid lines are the medians, and the shaded areas represent the quartiles of the data. The blue line corresponds to 0.5 $K_Z$min case, and the orange line corresponds to the 0.1 $K_Z$min case.

thermal convective mixing has already begun in the model. In contrast, at 5 AM local time, the gradient in CO concentration from the surface to 100 m increases by 2-20%, such that the lowest portion of the vertical profile changes shape and is no longer well mixed (Figure 5.13). It appears that the onset of turbulent mixing as a result of thermal fluctuations is occurring too quickly in the model.

In the morning, observed ozone vertical profiles have a minimum in ozone at the surface, and an increase in ozone concentration with altitude at a rate of 0.05 ppbv/m up to an altitude of 600 m (Figure 5.14). Above 600 m, ozone gradually decreases. In the 0.5 $K_Z$min case, ozone concentrations are overestimated by 15% between the surface and 400 m, and the gradient in ozone between 0-250

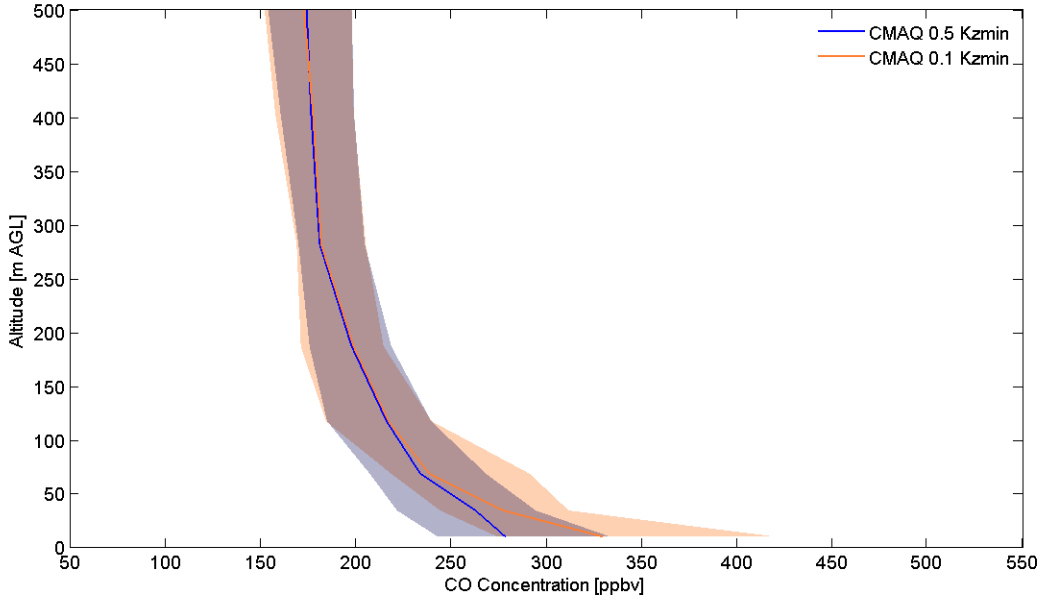

Figure 5.13: Comparison of modeled morning CO vertical profiles at 5 AM. The solid lines are the medians, and the shaded areas represent the quartiles of the data.

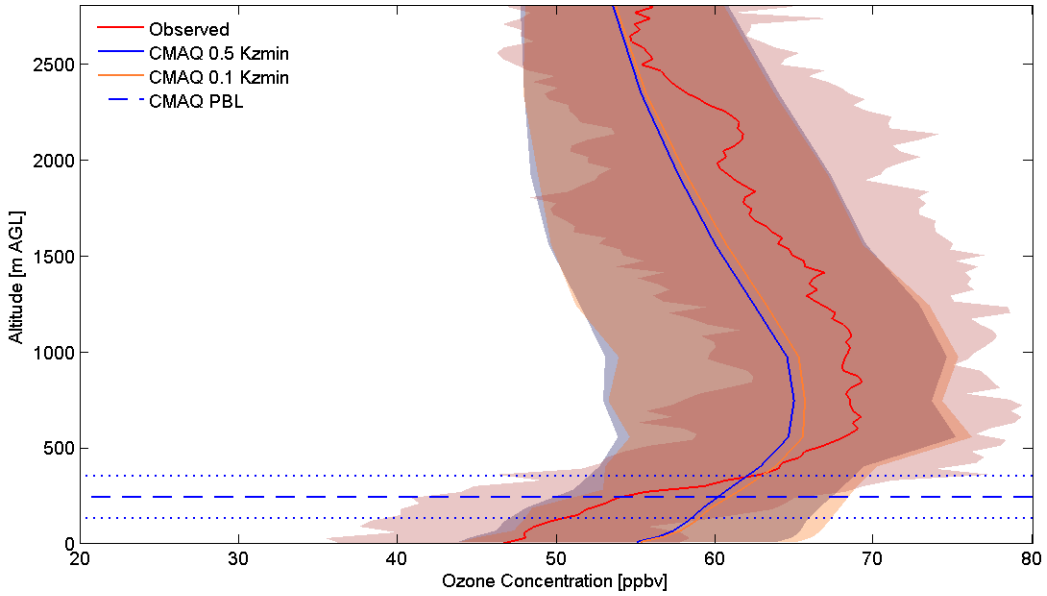

Figure 5.14: Comparison of observed (red) and modeled morning ozone vertical profiles. The solid lines are the medians, and the shaded areas represent the quartiles of the data. The blue line corresponds to 0.5 $K_Z$min case, and the orange line corresponds to the 0.1 $K_Z$min case.

m is underestimated. Above 400 m, the model underestimates ozone concentrations by 6%. In the 0.1 $K_Z$min case, below 400 m ozone concentrations do not change. Above 400 m, there is a 1 ppbv increase in ozone. This is likely a result of less ozone aloft mixing down to the surface at night. Comparison of the 0.5 $K_Z$min and 0.1 $K_Z$min case ozone vertical profiles of ozone at 5 AM show a 2-4% increase in ozone between 100-700 m when mixing is slowed down (Figure 5.15). Increasing ozone concentrations in the residual layer by slowing down nighttime mixing may enhance the models ability to simulate long range transport.

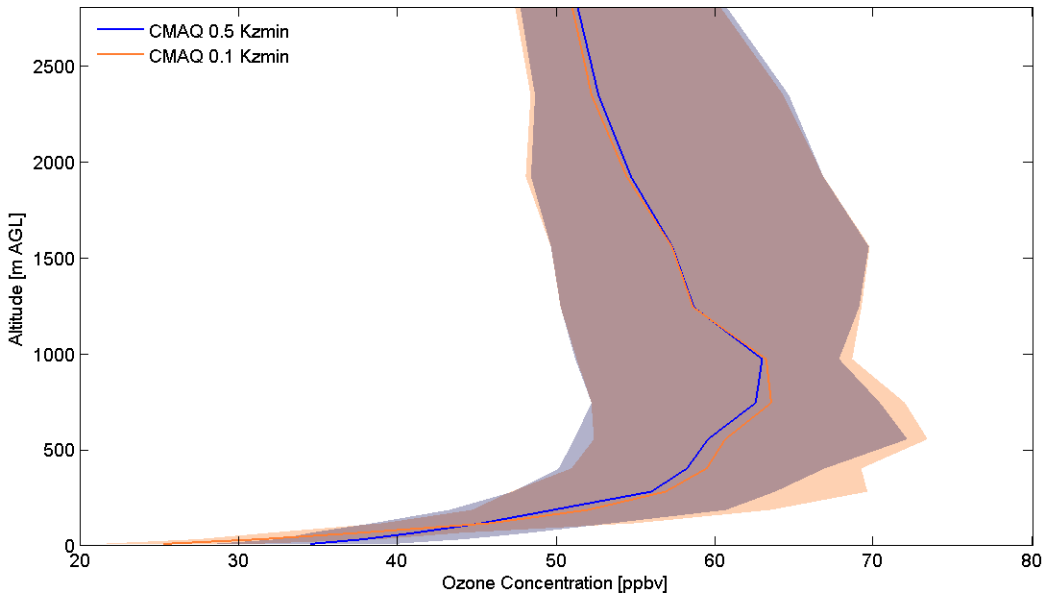

Figure 5.15: Comparison of modeled ozone vertical profiles at 5 AM. The solid lines are the medians, and the shaded areas represent the quartiles of the data.

5.6 Conclusions

Changing the default CMAQ minimum K_Z lower limit to 0.1 m^2/s results in better model agreement with surface ozone observations, although there is little impact during daylight hours. The model better captures the observed ozone minimum and the profile shape with slower mixing. The afternoon peak ozone has a larger component formed as a result of morning chemistry. A smaller minimum K_Z also increases ozone concentrations aloft because less ozone is mixed down to the surface at night.

NO_X dry deposition increased by 30-70% in the model when the $K_Z$min was decreased. Consequently, fewer NO_X molecules from local sources in the model will be available in the morning to make ozone. NO_X molecules that have been transported from distant sources in the model become more important.

The model compared to observations overestimates nighttime surface NO_2 concentrations in urban areas. This may a result of underestimation of the deposition velocity of NO_2 at high concentrations (>10 ppbv) in the model. A nonlinear deposition path for NO_2 would have the effect of increasing the deposition velocity. However, as a result of this deposition mechanism, NO_2 has the potential to be re-emitted in the morning as NO.

Model performance of CO and ozone morning vertical profiles improves, but not greatly, when $K_Z$min is reduced. When turbulent vertical mixing is reduced, the shape of the CO and ozone vertical profiles is closer to observation. However, the effect is not large enough to bring the model and measurements into agreement. Yet,

there is a considerable effect on the modeled CO and ozone vertical profile shape a few hours earlier than when the observations were taken. Thus, the well-mixed CO and ozone morning vertical profiles may be a result of overestimated turbulent mixing after sunrise.

Chapter 6

Measurement of NO_2 Using Cavity Ring-Down Spectroscopy

6.1 Introduction

NO_X plays a central role in local and global biogeochemical cycles of reactive nitrogen. In polluted atmospheres where high ozone concentrations are a problem, monitoring of NO_2 is necessary to understand the effects of control strategies, to monitor progress for compliance with regulatory standards, and understand the formation and loss of ozone. There is also a need for NO_2 vertical profiles for satellite validation and to study pollutant transport in models (U.S. EPA, 2009).

In light of new findings linking respiratory illnesses with short-term exposure to high NO_2 concentrations, the EPA has proposed tougher NO_2 standards and a comprehensive NO_2 monitoring system near roadways, where the highest levels of NO_2 are often found. To meet the monitoring demands put forth by this new legislation and to address the need for model and satellite validation data, a specific, reliable, fast, economical method for monitoring NO_2 in rural and urban environments will be needed.

A variety of methods exist for measuring NO_2, ranging from relatively inexpensive off-the-shelf commercial analyzers to research grade, highly sensitive techniques. In the AQS monitoring network, NO_2 observations for compliance with EPA's NO_2 NAAQS is usually accomplished with reduction of NO_2 to NO followed by reaction

with ozone and chemiluminescence using commercially available instruments (U.S. EPA, 2006); the concentration of NO_2 is determined from the difference between NO_X (the sum of NO and NO_2) and NO measured directly.

The most common method for conversion of NO_2 to NO, and the one used in the AQS network, is to pass a sample over 375C Mo. This technique also converts a variety of other species, including peroxy acetyl nitrate, organic nitrates, HONO, and HNO_3, to NO. While this technique is adequate for demonstrating compliance with the NO_2 standard, it can overestimate NO_2 substantially (Fehsenfeld, et al., 1987, Poulida, et al., 1994).

Other methods for ambient measurements of NO_2 have been reviewed (Navas, et al., 1997, Parrish and Fehsenfeld, 2000, McClenny, et al., 2002, Clemitshaw, 2004, EPA, 2006), and will be briefly summarized here. These instruments are generally custom build research grade devices that are not widely available.

Photolysis of NO_2 followed by chemiluminescence offers greater specificity than the hot Mo reduction discussed above (Gao, et al., 1994). Detection limits for this method can reach 25 pptv/10 s with 10% uncertainty for NO_2, while the detection limit for commercial instruments using thermal reduction are in the 100 pptv range (Del Negro, et al., 1999). However, the photolysis efficiency of NO_2 to NO is less than unity. Thus the technique requires frequent calibration. Chemiluminescence of NO_2 with luminol does not require conversion to NO (Schiff, et al., 1986). However the luminol technique is nonlinear at low NO_2 concentrations, and will respond to peroxy acetyl nitrate (PAN).

The Matrix Isolation Electron Spin Resonance (MIESR) technique involves

cryogenic trapping of NO_2 followed by electron spin resonance. This method has a detection limit of 20 ppt with 10% error, but requires 30 min sampling (Mihelcic, et al., 1985, Parrish and Fehsenfeld, 2000). Differential Optical Absorption Spectroscopy (DOAS) is a remote sensing long path absorption technique that measures the integrated concentration of NO_2 over several kilometers (Edner, et al., 1993, Stevens, et al., 1993). Although this technique allows for large area monitoring, it requires high-power lasers. Tunable Diode Laser Absorption Spectroscopy (TDLAS) is a specific in-situ spectroscopic technique for NO_2, but tends to have a higher detection limit (50 ppt) than chemiluminescence. Finally, Laser Induced Fluorescence (LIF) is a specific technique that is free of interferences with a low (10 ppt) detection limit. However, this method also requires high-power lasers (Sandholm, et al., 1990, Cohen, 1999)

A number of intercomparison studies demonstrating the accuracy of these research grade instruments have generally found agreement within 10-30% (Fried, et al., 1987, Fehsenfeld, et al., 1990, Sickles, et al., 1990, Kenny, et al., 1994, Harder, et al., 1997, Dunlea, et al., 2007). Because of the inherent drawbacks mentioned above, use of these labor intensive and expensive methods has generally been restricted to short-term field studies. In this chapter, I will present results, which have appeared in Castellanos, et al. (2009b), from the implementation of a commercial Cavity Ring-Down Spectrometer to measure ambient NO_2 in a polluted environment.

6.2 Cavity Ring-Down Spectroscopy

Cavity Ring-Down Spectroscopy (CRDS) is a highly sensitive optical absorption technique that uses the rate of decay of light intensity in an optical cavity to measure the concentration of an analyte. The principles of CRDS have been described previously (O'Keefe and Deacon, 1988, Jongma, et al., 1995, Romanini, et al., 1997, Hargrove, et al., 2006); briefly, a light pulse is coupled into an optical cavity made up of two highly reflecting mirrors (Figure 6.1). At each pass the small fraction of light that is transmitted through one end of the cavity is monitored with a photodetector. The light passes through the sample hundreds of times resulting in path lengths on the order of kilometers, and great sensitivity. The exponential decay of light intensity inside the cavity can be characterized by a cavity ring-down time constant, t, a function of the reflectivity of the mirrors, the length of the cavity, Raleigh scattering by air, and absorption by the analyte (6.1).

$$I(t) = I_0 e^{(-t/\tau)} \tag{6.1}$$

If the analyte fills the length of the cavity, the analyte number concentration (N molecules cm^{-3}) can be determined by 6.2, where τ_0 is the ring-down time constant when the absorbing analyte is absent from the cavity, c is the speed of light, and σ is the analyte absorption cross section in cm^2/molecule.

$$N = \frac{1}{c\sigma}\left(\frac{1}{\tau} - \frac{1}{\tau_0}\right) \tag{6.2}$$

The development of CRDS for absorption studies can be traced back to O'Keefe and Deacon (1988) who were the first to record an absorption spectrum of molec-

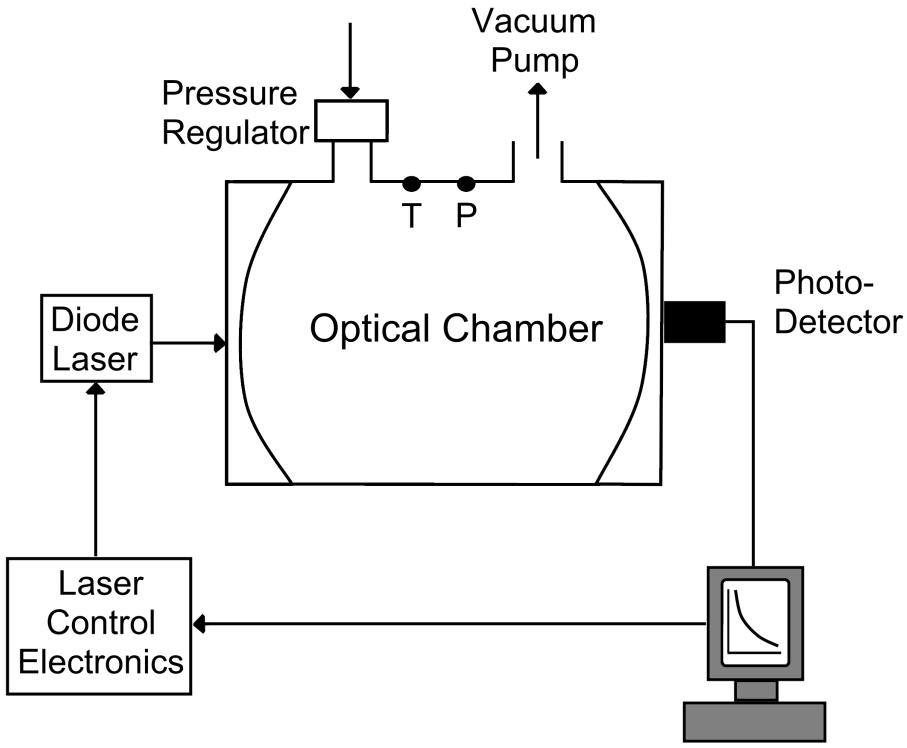

Figure 6.1: A schematic diagram of the CRDS apparatus used to measure NO_2. Pressure in the optical chamber is maintained 170 torr (227 hPa). The mirrors, 30 cm apart, reflect 99.95% of the radiation from the 407.38 nm laser resulting in an effective path length approaching 1000 m.

ular oxygen with CRDS. Since then, many groups have used CRDS for trace gas measurements (Jongma, et al., 1995, Scherer, et al., 1995, Romanini, et al., 1997, Vasudev, et al., 1999, Lauterbach, et al., 2000, Fuchs, et al., 2009). For a review of the many uses of CRDS see Berden (2005) and Wheeler et al. (1998).

6.3 Experimental Method

6.3.1 Cavity Ring-Down Spectrometer

In this work, we characterize a commercially available CRDS NO_2 detector (RMT-200, Los Gatos Research, Inc., Mountain View, CA), and describe modifications to enhance its detection limit. The instrument comes equipped with a small, continuous-wave, diode laser operating at 407.38 nm with a pulse rate of 1,200 Hz, highly reflecting mirrors (99.95% at 390-425 nm) separated by 30 cm, and a pressure regulator that maintains the internal pressure of the cavity at 170 torr (227 hPa). Because few tropospheric constituents have significant absorption cross-sections or ambient concentrations in this spectral range, the method is essentially free of interferences (Hargrove, et al., 2006, Fuchs, et al., 2009). The absorption cross-section of glyoxal is the same order of magnitude as that of NO_2, but is present in the atmosphere at part per trillion by volume (pptv) levels. At ambient NO_2 concentrations well below the part per billion by volume (ppbv) level this could lead to a bias in the measurement.

The instrument baseline drifts and for ambient observations, the instrument must regularly measure a NO_2-free or background ring-down time. Accordingly, we installed a solenoid valve wired to a timer to periodically divert the sample air through a scrubber. We found that commercial metal oxide scrubbers found in TECO Model 49 and Dasibi Model 1003AAS ozone analyzers effectively removed NO_2 from sample air. A ring-down time equal to that of zero air was observed for samples of 13-140 ppbv NO_2 at room temperature after passing through the

scrubber.

The software algorithms to calculate NO_2 concentration from ring-down time, including the NO_2 absorption cross-section, were used as supplied by the instrument manufacturer. The instrument calculates and records the NO_2 concentration every second from the average of roughly 1,000 ring-down times. Background correction was completed in post processing.

The instrument was calibrated with NO_2 generated by gas phase titration (GPT) of NO with O_3. The amount of NO_2 generated for excess ozone can be calculated from either the loss of ozone or the known initial concentration of NO. We mixed compressed air, a small flow of NO-in-Nitrogen (Air Products, 3.14 parts per million by volume (ppmv)), and 300 ppbv ozone generated with a UV lamp in an ozone calibrator (Model 49C, Thermo Electron Corporation, Franklin, MA) to produce NO_2 concentrations in the range of 13-140 ppbv (Figure 6.2). A revised concentration of 3.13 ppmv NO and 3.58 ppmv NO_X was found for the commercial NO-in-Nitrogen standard after comparison with a NIST standard reference material (SRM # 2627a). We estimate the uncertainty of the NO_X concentration in the standard to be $\pm 10\%$ (95% confidence interval).

6.3.2 Photolysis Followed by Chemiluminescence

The National Oceanic and Atmospheric Administration (NOAA) constructed a chemiluminescence detector from commercial chemiluminescence detectors (Model 42s, Thermo Electron Corporation). Addition of a high-output silent discharge

ozone electrode (Ozonology, Inc., Northbrook, IL) and a high capacity Teflon diaphragm pump (DTC-120, Kurt J. Lesker Co., Clairton, PA) enhanced the sensitivity. NO and NO_X were measured simultaneously on dedicated channels, and NO_2 was determined by difference. A photolytic NO_2 to NO converter made up of two UV light emitting diode (LED) arrays was operated on the NO_X channel (Luke, et al., 2009). The converter design, based on that of a solid-state light source converter (US Patent 7,238,328) developed by Air Quality Design, Inc. (Golden, CO), consisted of a 225 cm^3 cylindrical quartz cell illuminated longitudinally with two UV LED arrays (λ max = 395 $\pm$ 5 nm; Opto Diode Corp., Newbury Park, CA) at each end. A custom-built power supply provided current control and thermal overload protection to each array. Highly reflective Teflon (Gigahertz-Optik Inc., Newburyport, MA) used on the outer cell surfaces enhance photon reflectivity. At the nominal sample flow of 1 slm and pressure of 100 torr, cell residence time was approximately 2 s. Correction of NO and NO_2 values for variations in ambient O_3 (e.g., Ridley, et al., 1988) was not necessary.

The LED arrays impart little heat, which avoids interference from decomposition of PAN, N_2O_5, or HO_2NO_2. This instrument is also insensitive to other reactive compounds such as HNO_3, organonitrates, amines, and particulate nitrate which can be reduced to NO in commercial instruments using hot molybdenum and research grade instruments using gold-catalyzed CO. With the photolysis method, only nitrous acid (HONO) has a considerable interference potential; it has a significant absorption cross section at 395 nm, but its photolysis potential is only 1.4% of that of NO_2 at λmax = 395 nm. Recent tests on the NOAA instrument suggest

a HONO interference of about 5%, suggesting that the peak emission wavelength is slightly shorter than 395 nm.

6.3.3 Intercomparison on Ambient Air

The intercomparison of ambient NO_2 measurements by the CRDS and NOAA chemiluminescence instruments was conducted on January 5-18, 2009. The two instruments sampled ambient air outside of the laboratory window next to a busy parking lot in College Park, MD. Diverting sample air through the scrubber every 15 min for 3 min established a background for the CRDS instrument. To test the efficiency of the NO_2 scrubber and to measure any artifact in the measurement by the chemiluminescence device, the inlet line was flooded with zero air every 5 hours for 15 minutes. The chemiluminescence device was calibrated every 5 hours with a 55-65 ppbv mixture of NO (Scott Marin, 20.17 ppmv) in zero air, and the photolytic conversion efficiency of NO_2 to NO was tested every two to three days using GPT that generated 40 ppbv of NO_2 (Stedman, 1976). The GPT was also used to monitor the sensitivity of the CRDS instrument.

6.4 Results

6.4.1 Detection Limit and Response Time

From a reading of zero air, the 3s detection limit of the CRDS instrument is 0.2 ppbv integrated over 10 seconds (s), and 0.06 ppbv for 60 s. A first order response to a step-change in concentration was observed, with a response time of

	CRDS Analyzer	NOAA Chemiluminescence	Thermo Electron Corp. Model 42i TL
3σ Detection Limit (Averaging Time)	60 (60 s) pptv	100 (60 s) pptv	75 (120 s) pptv
Response Time	18 s(95%)	3 s(95%)	60 s
Power Draw	90 W	1000 W	300 W
Dimensions W x H x D [cm]	42.5 x 22 x 56	42 x 33 x 58.4	42.5 x 22 x 58.4
Weight	23 kg		25 kg

Table 6.1: A comparison of the performance statistics for a Thermo Electron Corp. chemiluminescence analyzer (as reported by the manufacturer), the CRDS analyzer, and the NOAA chemiluminescence instrument.

18 ± 1 s to reach 95% of the new signal. The CRDS NO_2 detector has an internal volume of 460 cm^3, including the optical cavity and tubing. At a typical flow rate of 560 cm^3 min^{-1}3 and an internal pressure of 170 torr, this corresponds to a residence time of 11 s. Thus, with larger pumping speeds, the instrument is capable of faster response times.

Table 6.1 lists a comparison of performance statistics for a commercial chemiluminescence instrument with a Mo heated catalyst (as reported by the manufacturer), the NOAA research grade device used in this intercomparison, and the CRDS instrument. The fixed internal pressure, low power draw, and compact size of the CRDS instrument makes it ideal for aircraft use at altitudes up to 10 km.

6.4.2 Calibration and Water Interference

The CRDS NO_2 measurements and the NO_2 concentrations calculated from the change in ozone concentration upon gas phase titration with the NO_X standard

dilutions were in excellent agreement (Figure 6.2). The least squares fit has a slope and intercept of 1.02 ± 0.02 and -1.8 ± 1.5ppbv, respectively, and a linear correlation coefficient R= 0.999. The slope of the comparison of CRDS NO_2 measurements to the concentration of NO_2 calculated from the mass flow rate of the NO_X standard dilutions has a low bias (linear least squares slope of 0.95 ± 0.01, intercept of 0.9 ± 0.6 ppbv, and linear correlation of R= 0.999) probably as a result of NO_2 losses in the mixing volume, tubing, and fittings, or errors in the flow controller calibrations, concentration of the NO calibration standard, etc.

An interference of 4.8 ppbv equivalent NO_2 was found for 2.2% water, similar to findings by Hargrove, et al. (2006). At constant altitude near the Earth's surface, where humidity changes slowly, monitoring the background ring-down time is an adequate correction for water. In rapidly changing ambient environments, as on an airplane, background corrections must occur frequently or water must be removed from the sample air. Furthermore, the NO_2 scrubber was found to be water sensitive; the metal oxide mixture acts as a reservoir for water, which leads to a positive interference during dry conditions (Wilson and Birks, 2006). We found that a three-meter coil of Nafion (Model MD-110-72F-4, Perma Pure, Inc., Toms River, NJ) tubing at the inlet of the CRDS instrument effectively eliminated the interference from water vapor, with undetectable losses of NO_2 for concentrations in the ppbv range.

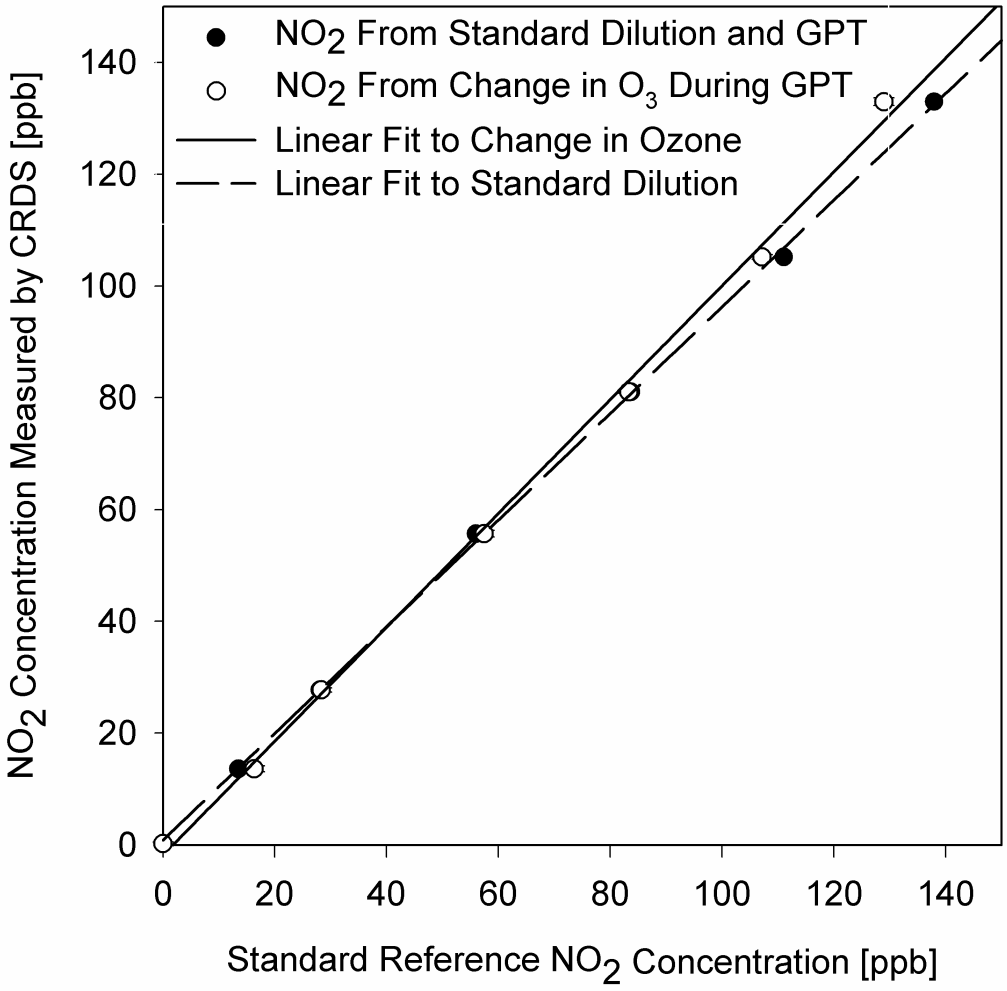

Figure 6.2: Comparison of NO_2 measured by CRDS to NO_2 concentrations calculated from a known concentration of NO in excess ozone (filled circles) and from the decrease in ozone concentration (open circles) monitored with an ozone detector based on UV absorption. The least squares fit to the data generated from the change in ozone concentration (solid line) has a slope of 1.02 ± 0.02, an intercept of -1.8 ± 1.5 ppbv; R= 0.999. The least squares fit to the data generated from the standard dilution (broken line) has a slope of 0.95 ± 0.01, an intercept of 0.9 ± 0.6 ppbv; R= 0.999. The error bars for each point are the same size or smaller than the circles.

6.4.3 Ambient Intercomparison

The comparison of the CRDS instrument with the NOAA chemiluminescence device measuring ambient air showed good agreement during both polluted and relatively clean time periods (Figure 6.3). On January 5-9 the correlation had a slope of 0.960 ± 0.002, an intercept of 0.28 ± 0.03 ppbv, and R of 0.995 (Figure 6.4a). The correlation drifted slightly with time. On January 10-16 the correlation had a slope of 0.932 ± 0.002, an intercept of -0.61 ± 0.04 ppbv, and R of 0.982 (Figure 6.4b).

The data before January 10^{th} are more reliable because the chemiluminescence analyzer experienced significant dynamic drift in the sensitivity of both channels during the remainder of the comparison (Figure 6.5) because variability in the power supply may have led to changes in the pumping speed (the sensitivity of a chemiluminescence instrument to NO is a linear function of the pumping speed). This introduced uncertainty in the calibration factor for this instrument on the order of 5%. Also, error in the NO_2 measurement by CRDS after January 9th developed because aerosols degraded the mirror surfaces and increased the noise. Although the sample air was passed through a 1 μm Teflon filter, some particles were still able to enter the cavity; the inlet was located roughly 10 meters from a popular idling spot for large trucks in the parking lot. A filter that removes particles down to 0.1 μm diameter is recommended. These interference events were identified by sharp increases in the standard deviation of the 1,000 ring-down events captured every second. After January 16, 2009 the ring-down times were too short to consider the

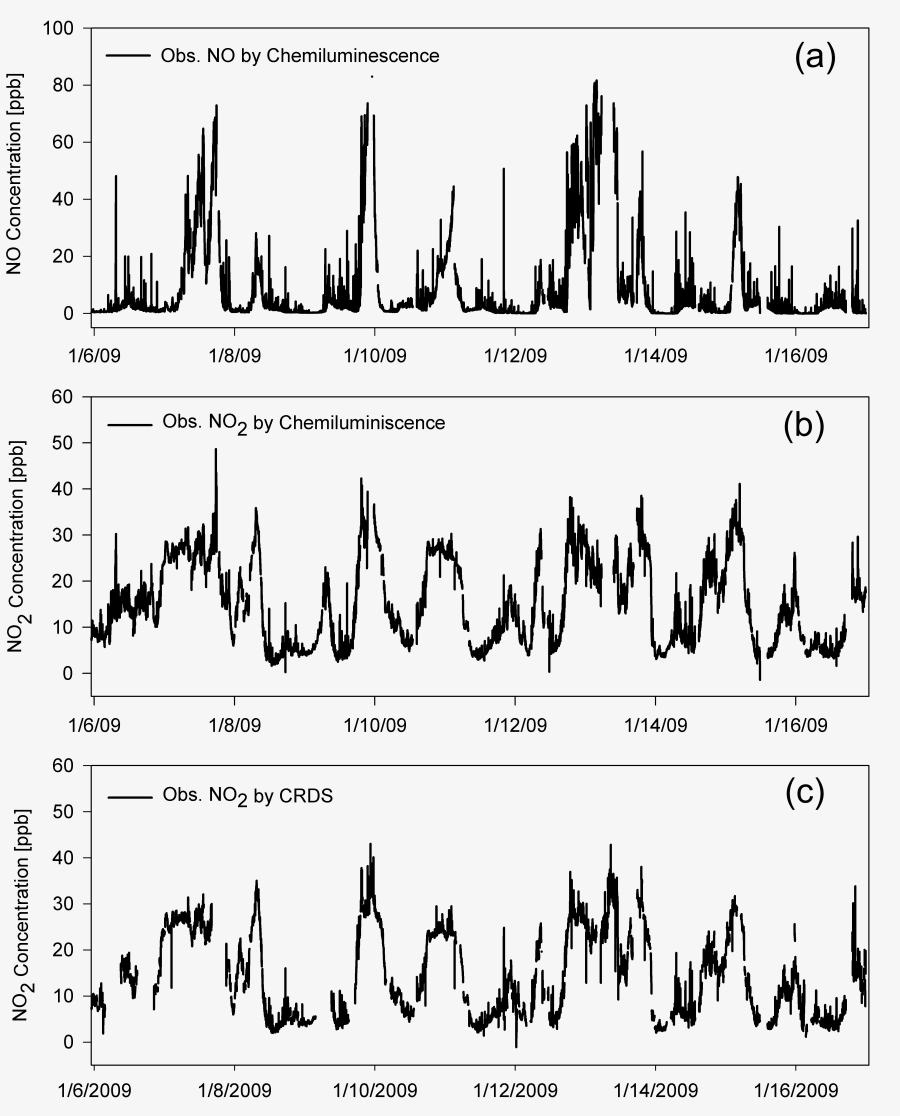

Figure 6.3: Ambient NO (a) and NO_2 measurements by chemiluminescence (b) and CRDS (c) from January 5, 2009 to January 16, 2009 in a suburban Maryland setting.

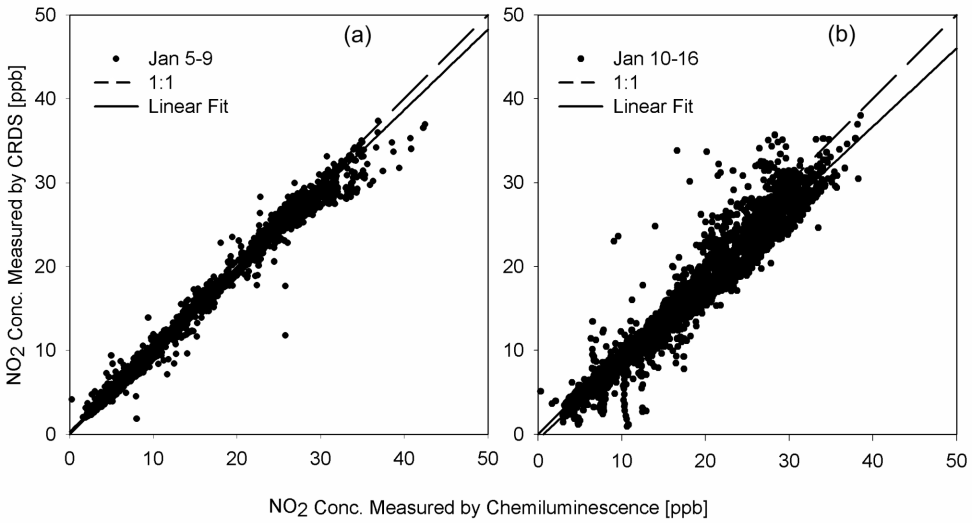

Figure 6.4: Scatter plots of ambient NO_2 measured by CRDS and chemiluminescence on January 5-9, 2009 (a) and January 10-16, 2009 (b). The slope, intercept, and R of the linear least squares fit to the January 5-9, 2009 data are 0.960 ± 0.002, 0.28 ± 0.03ppbv, and 0.995, respectively. The slope, intercept, and R of the linear least squares fit to the January 10-16, 2009 data are 0.932 ± 0.002, -0.61 ± 0.04 ppbv, and 0.982, respectively. The dashed line represents a one to one fit.

data reliable.

Over the course of January 5-16, the sensitivity of the CRDS instrument was analyzed eight times with GPT, and was found to fluctuate by 3% with no apparent systematic trend. The average sensitivity from these calibrations was used in the correlation plots with the chemiluminescence measurements to eliminate variability due to errors in the calibration technique. The efficiency of the NO_2 scrubber, analyzed every five hours, remained consistent with the results of our initial experiment throughout the intercomparison. Calibrations with the Nafion drying tubing showed no detectable losses of NO_2.

The two instruments capture the daily cycle of NO_X due to photochemistry and boundary layer development (Figure 6.6). The local maximum of NO_2 occurs at 7 am (local standard time) during the peak in morning rush hour when fresh NO from cars is emitted into the shallow mixed layer where it reacts with ozone to produce NO_2. The ratio of NO/NO_2 peaks at noon signaling maximum photolysis of NO_2 to NO (and photochemical ozone production), and there is generally higher NO_X at night reflecting the daily evolution of mixing height.

6.5 Discussion

Measurements of NO_2 with custom-built CRDS instruments at 405-425 nm have accurately detected NO_2 concentrations from 0.15 ppbv to 200 ppmv (O'Keefe, et al., 1999, Evertsen, et al., 2002, Mazurenka, et al., 2005, Fuchs, et al., 2009). A previous intercomparison study with a commercial chemiluminescence device uti-

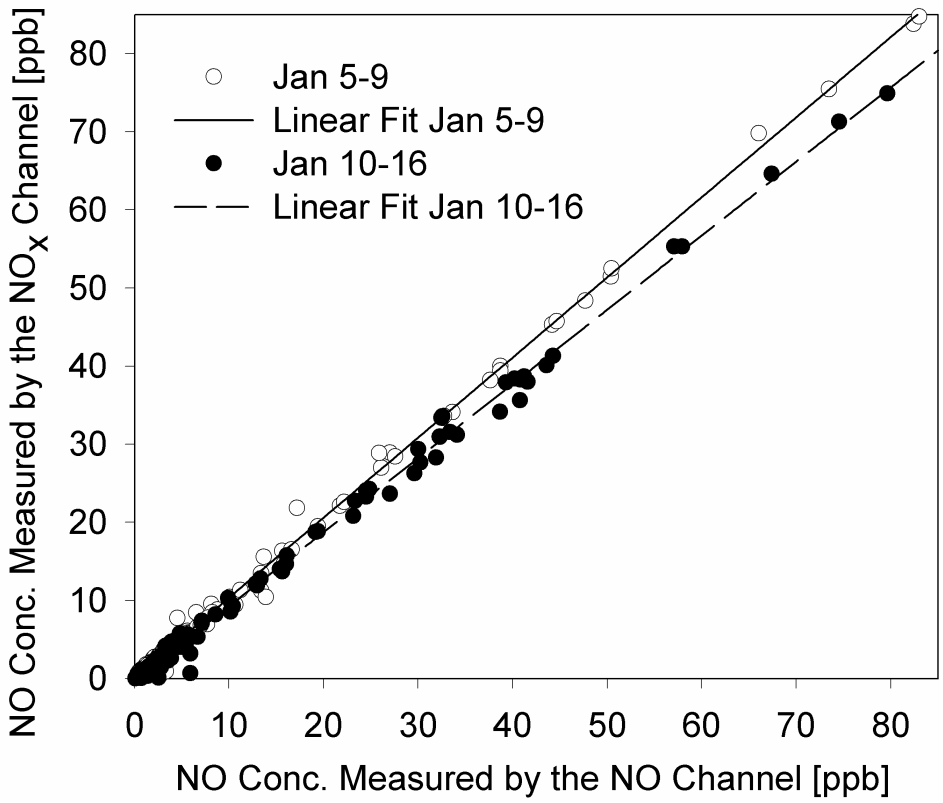

Figure 6.5: Scatter plot of NO concentrations measured by the NO and dark NO_X channels of the chemiluminescence device on January 5-9, 2009 (open circles) and January 10-16, 2009 (closed circles). The slope drifted from 1.025 $\pm$ 0.004 on January 5-9 to 0.949 $\pm$ 0.004 on January 10-16. On January 5-9, the two channels of the instrument give consistent measurements of NO over the concentration range observed. After January 10^{th}, the sensitivity of both channels drifted dynamically.

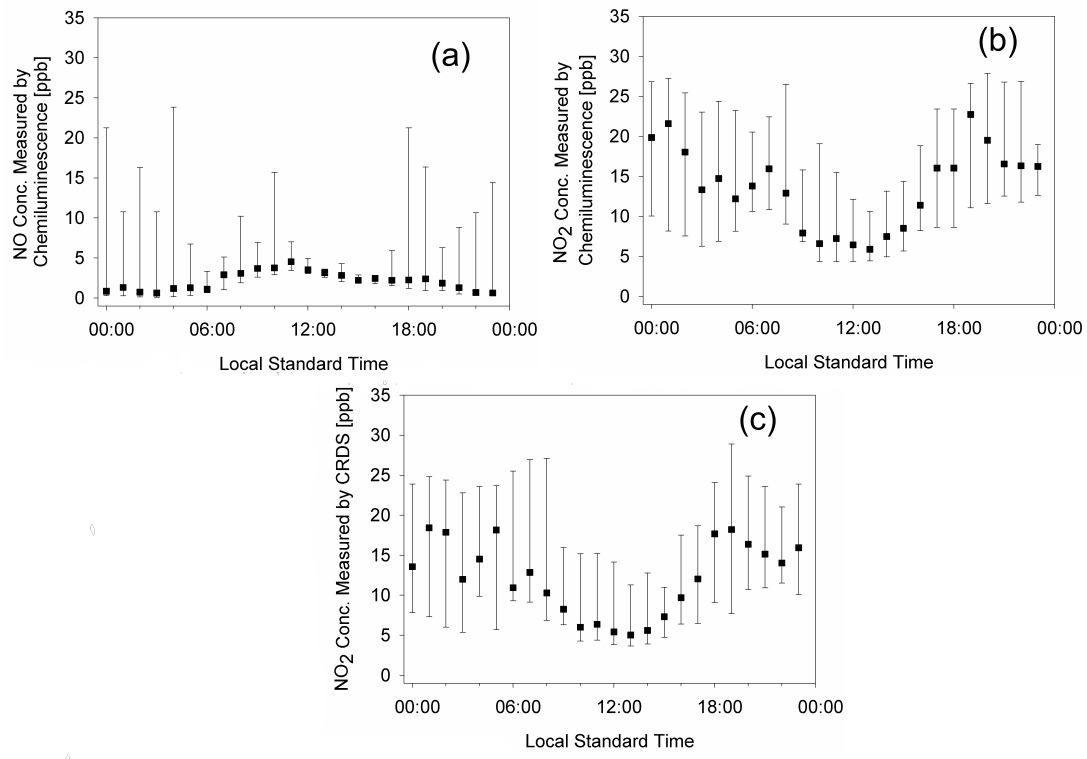

Figure 6.6: Diel cycle of ambient NO (a) and NO_2 (b) measurements by chemiluminescence and NO_2 (c) measured by CRDS. The markers are the median hourly concentrations, and the error bars are the 25th and 75th percentiles. High concentrations of NO_2 are seen at night because the temperature inversion inhibits vertical mixing and high concentrations of NO are seen during the daylight hours because solar UV radiation photolyzes NO_2 to NO.

lizing thermal conversion of NO_2 to NO showed an average agreement within 5% (Wada and Orr-Ewing, 2005). However, the sample air was collected from within the laboratory where deposition of HNO_3 and other interfering substances onto the laboratory surfaces would eliminate the artifact in the chemiluminescence technique. We find similar results for the performance of a modified commercial CRDS NO_2 analyzer during a twelve-day intercomparison with a chemiluminescence device utilizing photolytic conversion of NO_2 to NO. The least squares fit gave a slope of 0.960 ± 0.002 and R of 0.995 over the five days when the two instruments were performing optimally. The concentration of ambient NO_2 ranged from 2 to 40 ppbv. Care must be taken to filter particles from the sample stream because when particles enter the optical cavity the noise level increases substantially. Also, the variations in the NO sensitivity of the NOAA detector may have been caused by variations in the pumping speed as a result of power fluctuations in our laboratory. Repeating the experiment with a cleaner source of line power and a smaller filter may produce better overall results.

Our studies show that a lightweight, commercial CRDS NO_2 detector can, with appropriate modifications, measure NO_2 with rapid response, specificity, and sensitivity adequate for urban and rural continental environments. The most important modification is regular chemical zeroing with a commercial, metal oxide catalyst. The low power required and fixed internal pressure makes this analyzer suitable for aircraft use up to 10 km altitude. The modified CRDS method shows great promise for ground level monitoring of NO_2 and for airborne measurements.

Chapter 7

Conclusions

7.1 Overview

The sensitivity of the Community Multiscale Air Quality (CMAQ) model to the temporal variation of four emissions sectors was investigated to understand the effect of the daily variability in emissions on modeled ozone. Decreasing the variability of mobile source emissions changed the 8-hour maximum ozone concentration in urban areas on days with high (greater than 80 ppbv) ozone by up to $\pm$ 7 ppbv, resulting in a decrease in the number of 80 ppbv exceedances. Increasing the variability of point source emissions effected ozone concentrations by $\pm$ 6 ppbv, but only in areas close to the source. The patchy result of positive and negative sensitivities close to each other may be due to the weakness of the model at transporting point source emissions, which underestimates the area and magnitude of ozone generated by point source emissions. Because of this weakness, the model appears to be able to respond more realistically to emissions control strategies that target the time of day of emissions from mobile, area, and non-road sources than from point sources. The other emissions source groups also affected the number of 80 ppbv exceedances, but on a more local level. This reinforces the importance of understanding local emissions characteristics in order to compose effective ozone abatement strategies.

CO is an ideal tracer for analyzing pollutant transport in AQMs because the

atmospheric lifetime is longer than the timescale of boundary layer mixing. To be able to use CO as a tracer, model performance of CO must be well understood. An evaluation of CO model performance in CMAQ was carried out using aircraft observations taken for the Regional Atmospheric Measurement, Modeling and Prediction Program (RAMMPP) in the summer of 2002. A Comparison of modeled and observed CO total columns was generally in agreement within the combined uncertainty. There is little evidence that the CO emissions inventory is grossly overestimated. CMAQ predicts the same vertical profile shape for all of the observations: CO well mixed throughout the boundary layer. However, the majority of observations have poorly mixed air below 500 m, and well mixed air above. Under the configuration where CO does not dry deposit, the total column of CO is within 5-6% of observations, but CO concentrations continue to be underestimated near the surface because the vertical profile shape remains well mixed. CMAQ appears to predict faster CO transport away from the surface than is observed. At higher altitudes, above the modeled and observed PBL, the model underestimates CO concentrations by 10-15%, suggesting that boundary layer venting by convection is underestimated in the model.

Turbulent mixing in the model is represented with K-theory. A minimum K_Z that scales with fractional urban land use is imposed in order to account for subgrid scale obstacles in urban areas and the urban heat island effect. Micrometeorological observations suggest the minimum K_Z is somewhat high. A sensitivity case where the minimum was reduced from 0.5 m^2/s to 0.1 m^2/s was carried out. Model performance of surface ozone observations at night increased significantly. The model

better captures the observed ozone minimum with slower mixing. As a result, the afternoon peak ozone has a larger component formed during morning chemistry. The use of a smaller $K_Z$min also increases ozone concentrations in the residual layer, increasing the potential for long-range transport in the model. Model performance of CO and O_3 morning vertical profiles improves, but the effect of slower nighttime mixing is not large enough to bring the model and measurements into agreement. The modeled well-mixed CO and ozone morning vertical profiles may be a result of overestimated turbulent mixing after sunrise.

A small, commercially available cavity ring-down spectroscopy (CRDS) NO_2 detector suitable for surface and aircraft monitoring was modified and characterized. A metal oxide scrubber was added to remove NO_2 and provide a chemical zero, improving the detection limit (3s of the background noise) from several parts per billion by volume (ppbv) to 0.06 ppbv, integrated over 60 s. Known interferences by water and particles were removed using Nafion tubing and a 1 μm Teflon filter, respectively. A 95% response time of 18 $\pm$ 1 s was observed for a step change in concentration. The CRDS detector was run in parallel to an ozone chemiluminescence device with photolytic conversion of NO_2 to NO. The two instruments measured ambient air in suburban Maryland. A least-squares fit to the comparison data resulted in a slope of 0.960 $\pm$ 0.002 and R of 0.995, showing agreement within experimental uncertainty.

7.2 Recommendations For Future Work

In Chapter 3, I analyzed the sensitivity of CMAQ to the temporal variation of the four anthropogenic emissions sectors. Mobile source variability had a significant effect on the model prediction of ozone. In areas where motor vehicle emissions dominate the NO_X inventory, analysis of the variability of near roadway observations of NO_X may prove insightful. Strategies for implementing stochastically emitting peaking units in emissions inventories are currently under consideration for the next comprehensive emissions inventory developed by the regional planning organizations. Under the current model configuration, increased variability in the large upwind point sources may not have a significant effect on modeled ozone in the Mid-Atlantic. Peaking units located near ozone nonattainment areas should be investigated.

In Chapter 4, I presented a model performance study of CO and showed that the modeled CO total column is generally in agreement with observations. Vertical profile measurements of CO in the Northeast taken by RAMPP are available from 1996 to present, and tropospheric column content of CO from the MOPPITT satellite are available from 2000. More confidence in the CO emissions inventories would be gained if the year-to-year trend in emissions also matched the trend in the CO total column observed by aircraft and satellites.

In Chapter 4 and 5, I presented results suggesting that vertical turbulent mixing in the model is occurring too quickly (K_Z is too high), but transport into the free troposphere by deep convective updrafts may be underestimated. An investiga-

tion into the relative rates of the CMAQ convective mixing and turbulent diffusion scheme is necessary. Understanding the relative rates of subsidence to updraft in the convective scheme and the effect on ozone model performance will be useful. An investigation into the model convective height will also be necessary. Model sensitivity studies have shown that increased vertical resolution improved model performance of surface ozone (Appel, et al., 2007). An in-depth analysis for the process behind this improvement would also be useful.

In Chapter 5, model performance for surface ozone concentration generally improved when nighttime mixing was slowed down. In rural areas the NO_2 bias improved but remained significantly underestimated, while in urban areas the bias in NO_2 increased. An analysis is needed that demonstrates the effect on model performance of NO_X by the improved parameterization of processes that control the availability of NO_X. For example, including in the model the heterogeneous conversion of NO_2 to HONO, a more highly variable N_2O_5 accommodation coefficient, and oxidation of alkyl nitrates would be helpful.

In Chapter 6, the implementation of a small commercial CRDS NO_2 detector for ambient monitoring in polluted environments was demonstrated. A comparison to NO_X observed at the Beltsville monitoring site may give more confidence in the technique. Including this instrument in the RAMPP aircraft sampling platform will provide useful measurements for observing the effects of emissions control strategies, ground truth validation for satellites, model performance studies, and understanding the effects of long range transport on ozone in the Northeast. Adding a temperature ramped inlet that decomposes PAN, alkyl nitrates, HONO and HNO_3 to NO_2 will

facilitate the measurement of vertical profiles of NO_y with the CRDS method as well.

Bibliography

[1] U.S. Environmental Protection Agency. Integrated science assessment for carbon monoxide (second external review draft). Technical Report EPA/600/R-09/019B, 2009.

[2] K.W. Appel, A.B. Gilliland, G. Sarwar, and R.C. Gilliam. Evaluation of the community multiscale air quality (cmaq) model version 4.5: Sensitivities impacting model performance part i-ozone. *Atmospheric Environment*, 41:9603–9615, 2007.

[3] J.R. Arnold and R.L. Dennis. Testing cmaq chemistry sensitivities in base case and emissions control runs at search and sos99 surface sites in the southeastern us. *Atmospheric Environment*, 40:5027–5040, 2006.

[4] J. Ayres, R. Maynard, and R. Richards. *Air Pollution and Health*. Imperial College Press, London, 2006.

[5] K. Baumann, E. J. Williams, W. M. Angevine, J.M. Roberts, R. B. Norton, G. J. Frost, F. C. Fehsenfeld, S. R. Springston, S. B. Bertman, and B. Hartsell. Ozone production and transport near nashville, tennessee: Results from the 1994 study at new hendersonville. *Journal of Geophysical Research*, 105(D7):9137–9153, 2000.

[6] S. Berman, J. Y. Ku, and S. T. Rao. Spatial and temporal variation in the mixing depth over the northeastern united states during the summer of 1995. *Journal of Applied Meteorology*, 38(12):1661–1673, 1999.

[7] T. H. Bertram and J. A. Thornton. Toward a parameterization of n2o5 reactivity on aqueous particles: the competing effects of particle liquid water, nitrate, and chloride. *Atmospheric Chemistry and Physics*, 9:8351–8363, 2009.

[8] I. Bey, D. J. Jacob, R. M. Yantosca, J. A. Logan, B. D. Field, A. M. Fiore, Q. B. Li, H. G. Y. Liu, L. J. Mickley, and M. G. Schultz. Global modeling of tropospheric chemistry with assimilated meteorology: Model description and evaluation. *Journal of Geophysical Research, [Atmospheres]*, 106(D19):23073–23095, 2001.

[9] G. A. Bishop and D. H. Stedman. Motor vehicle emissions variability. *Journal of the Air and Waste Management Association*, 46:667–675, 1996.

[10] G. A. Bishop and D. H. Stedman. A decade of on-road emissions measurements. *Environmental Science and Technology*, 42:1651–1656, 2008.

[11] B.J. Bloomer, J. Stehr, C.A. Piety, R. Salawitch, and R.R. Dickerson. Observed relationships of ozone air pollution with temperature and emissions. *Geophysical Research Letters*, 36:L09803, 2009.

[12] S. S. Brown, T. B. Ryerson, A. G. Wollny, C. A. Brock, R. Peltier, A. P. Sulliva, R. J. Weber, W. P. Dube, M. Trainer, J. F. Meagher, F. C. Fehsenfeld, and A. R. Ravishankara. Variability in nocturnal nitrogen oxide processing and its role in regional air quality. *Science*, 311:67–70, 2006.

[13] D. Brunner, J. Staehelin, H. L. Rogers, M. O. Kohler, J. A. Pyle, D. A. Hauglustaine, L. Jourdain, T. K. Berntsen, M. Gauss, I. S. A. Isaksen, E. Meijer, P. van Velthoven, G. Pitari, E. Mancini, V. Grewe, and R. Sausen. An evaluation of the performance of chemistry transport models - part 2: Detailed comparison with two selected campaigns. *Atmospheric Chemistry and Physics*, 5:107–129, 2005.

[14] R Buchdahl, C.D. Willems, M Vander, and A. Babiker. Associations between ambient ozone, hydrocarbons, and childhood wheezy episodes: a prospective observational study in south east london. *Occupational and Environmental Medicine*, 57:86–93, 2000.

[15] R. T. Burnett, R. E. Dales, M. E. Raizenne, D. Krewski, P. W. Summers, G. R. Roberts, M. Raad-Young, T. Dann, and J. Brook. Effects of low ambient levels of ozone and sulfates on the frequency of respiratory admissions to ontario hospitals. *Environmental Research*, 65:172–194, 1994.

[16] J. A. Businger, J. C. Wyngaard, Y. Izumi, and E. F. Bradley. Flux-profile relationships in the atmospheric surface layer. *Journal of the Atmospheric Sciences*, 28:181–189, 1971.

[17] D. Byun and K.L. Schere. Review of the governing equations, compurational algorithms, and other components of the models-3 community multiscale air quality (cmaq) modeling system. *Applied Mechanics Reviews*, 59:51–77, 2006.

[18] D. W. Byun, Young. J., J. Pleim, M. T. Odman, and K. Alapaty. Numerical transport algorightms for the community multiscale air quality model (cmaq) chemical transport model in generalized coordinates. Technical Report EPA/600/R-99/030, US Environmental Protection Agency, 1999.

[19] D. W. Byun, S.-T. Kim, and S.-B. Kim. Evaluation of air quality models for the simulation of a high ozone episode in the houston metropolitan area. *Atmospheric Environment*, 41:837–853, 2007.

[20] P. Castellanos, W. T. Luke, P. Kelley, S. H. Ehrman, and R. R. Dickerson. Modification of a commercial cavity ring-down spectroscopy no2 detector for enhanced sensitivity. *Review of Scientific Instruments*, 80:113107, 2009.

[21] P. Castellanos, J.W. Stehr, R.R. Dickerson, and S.H. Ehrman. The sensitivity of modeled ozone to the temporal distribution of point, area, and mobile source emissions in the eastern united states. *Atmospheric Environment*, doi:10.1016/j.atmosenv.2009.05.045, 2009.

[22] X. H. Chen, D. Hulbert, and P. B. Shepson. Measurement of the organic nitrate yield from oh reaction with isoprene. *Journal of Geophysical Research*, 103:25563–25568, 1998.

[23] Kevin L. Civerolo, Huiting Mao, and S. Trivikrama Rao. The airshed for ozone and fine particulate pollution in the eastern united states. *Pure and Applied Geophysics*, 160:81–105, 2003.

[24] R. C. Cohen. Laser-induced fluorescence detection of atmospheric no2 at parts per trillion mixing ratios: Implications for nitrogen oxide photochemistry in the stratosphere and troposphere. *Abstracts of Papers of the American Chemical Society*, 218:U348–U348, 1999.

[25] R. Conrad and W. Seiler. Role of microorganisms in the consumption and production of atmospheric carbon monoxide. *Applied Environmental Microbiology*, 9:1353–1356, 1980.

[26] P. Constant, L. Poissant, and R. Villemur. Annual hydrogen, carbon monoxide, and carbon dioxide concentrations and surface to air exchanges in a rural area (quebec, canada). *Atmospheric Environment*, 42:5090–5100, 2008.

[27] L. A. Del Negro, D. W. Fahey, R. S. Gao, S. G. Donnelly, E. R. Keim, J. A. Neuman, R. C. Cohen, K. K. Perkins, L. C. Koch, R. J. Salawitch, S. A. Lloyd, M. J. Proffitt, J. J. Margita, R. M. Stimpfle, G. P. Bonne, P. B. Voss, P. O. Wennber, C. T. McElroy, W. H. Swartz, T. L. Kusterer, D. E. Anderson, L. R. Lait, and T. P. Bui. Comparison of modeled and observed values of no2 and jno2 during the photochemistry of ozone loss in the arctic region in summer (polaris) mission. 1999.

[28] B. Eder and S. Yu. A performance evaluation of the 2004 release of models-3 cmaq. *Atmospheric Environment*, 40(26):4811–4824, 2006.

[29] H. Edner, P. Ragnarson, S. Spannare, and Sune Svanberg. Differential optical absorption spectroscopy (doas) system for urban atmosperic pollution monitoring. *Applied Optics*, 32:327–333, 1993.

[30] R. Evertsen, A. Staicu, N. Dam, A. van Vliet, and J. J. ter Meulen. Pulsed cavity ring-down spectroscopy of no and no2 in the exhaust of a diesel engine. *Applied Physics B: Lasers and Optics*, 74(4):465, 2002. 10.1007/s003400200828.

[31] M. Faraji, Y. Kimura, E. McDonald-Buller, and D. Allen. Comparison of the carbon bond and saprc photochemical mechanisms under conditions relevant to southeast texas. *Atmospheric Environment*, 42:5821–5836, 2008.

[32] J. Fine, L. Vuilleumier, S. Reynolds, P. Roth, and N. Brown. Evaluating uncertainties in regional photochemical air quality modeling. *Annual Review of Environment and Resources*, 28:59–106, 2003.

[33] B. Finlayson-Pitts and J.N. Pitts Jr. *Chemistry of the Upper and Lower Atmosphere*. Academic Press, New York, 1999.

[34] Arlene M. Fiore, Daniel J. Jacob, Isabelle Bey, Robert M. Yantosca, Brendan D. Field, and Andrew C. Fusco. Background ozone over the united states in summer: Origin, trend, and contribution to pollution episodes. *Journal of Geophysical Research*, 107(D15):4275, 2002.

[35] Sheldon K. Friedlander. *Smoke, Dust, and Haze*. Oxford University Press, New York, second edition edition, 2000.

[36] T. M. Frischer, C. Studnicka, E. Gartner, F. Tauber, A. Horak, J. Veiter, J. Spengler, J. Kuhr, and R. Urbanek. Lung function growth and ambient ozone: a 3-year population study in schoolchildren. *American Journal of Respiratory and Critical Care Medicine*, 160:390–396, 1999.

[37] M. W. Gallagher, E. Nemitz, J. R. Dorsey, D. Fowler, M. A. Sutton, M. Flynn, and J. Duyzer. Measurements and parameterizations of small aerosol deposition velocities to grassland, arable crops, and forest: influence of surface roughness length on deposition. *Journal of Geophysical Research*, 107:4154, 2002.

[38] W.J. Gauderman, H Gilliland, G.F. and.Vora, E. Avol, D. Stram, R. McConnell, D. Thomas, F. Lurmann, H.G. Margolis, E.B. Rappaport, K. Berhane, and Peters J.M. Association between air pollution and lung function growth in southern california schoolchildren: results from a second cohort. *American Journal of Respiratory and Critical Care Medicine*, 166:76–84, 2002.

[39] E. Gego, A. Gilliland, J. Godowitch, S.T. Rao, P.S. Porter, and C. Hogrefe. Modeling analyses of the effects of changes in nitrogen oxides emissions from the electric power sector on ozone levels in the eastern united states. *Journal of the Air and Waste Management Association*, 58:580–588, 2008.

[40] M.W. Gery, G.Z. Whitten, J.P. Killus, and M.C. Dodge. A photochemical mechanism for urban and regional scale computer modeling. *Journal of Geophysical Research*, 94:12925, 1989.

[41] A.B. Gilliland, C. Hogrefe, R.W. Pinder, J.M. Godowitch, K.L. Foley, and S.T. Rao. Dynamic evaluation of regional air quality models: Assessing changes in o3 stemming from changes in emissions and meteorology. *Atmospheric Environment*, 42:5110–5123, 2008.

[42] J.M. Godowitch, A.B. Gilliland, R.R. Draxler, and S.T. Rao. Modeling assessment of point source nox emission reductions on ozone air quality in the eastern united states. *Atmospheric Environment*, 42(1):87–100, 2008.

[43] G.A. Grell, J. Dudhia, and D.R. Stauffer. A description of the 5th generation penn state/ncar mesoscale model (mm5). Technical Report NCAR/TN 398+STR, National Center for Atmospheric Research, 1994.

[44] J.C Hains, B.F. Taubman, A.M. Thompson, L.T. Marufu, J.W. Stehr, and R.R. Dickerson. Origins of chemical pollution derived from mid-atlantic aircraft profiles using a clustering technique. *Journal of Geophysical Research*, 42(8):1727–1741, 2008.

[45] Jennifer Hains. *A chemical climatology of lower tropospheric trace gases and aerosols over the Mid-Atlantic Region*. PhD thesis, University of Maryland, 2007.

[46] Z. Han, M. Zhang, and J. An. Sensitivity of air quality model prediction to parameterization of vertical eddy diffusivity. *Environmental Fluid Mechanics*, 9:73–89, 2009.

[47] S.R. Hanna, J.C. Chang, and M.E. Fernau. Monte carlo estimates of uncertainties in predictions by a photochemical grid model (uam-iv) due to uncertainties in input variables. *Atmospheric Environment*, 32(21):3619–3628, 1998.

[48] James Hargrove, Liming Wang, Karen Muyskens, Mark Muyskens, David Medina, Susan Zaide, and Jingsong Zhang. Cavity ring-down spectroscopy of ambient no2 with quantification and elimination of interferences. *Environmental Science and Technology*, 40(24):7868–7873, 2006.

[49] H. Hass, H. J. Jacobs, M. Memmescheimer, A. Ebel, and J. S. Change. Simulation of a wet deposition case in europe using the european acid deposition model (eurad). In *Air Pollution Modeling and its Applications VIII*, pages 205–213. Plenum Press, New York, 1991.

[50] C. Hogrefe, S.T. Rao, I.G. Zurbenko, and P.S. Porter. Interpreting the information in ozone observations and model predictions relevant to regulatory policies in the eastern united states. *Bulleting of the American Meteorological Society*, 91:2083–2106, 2000.

[51] C. V. Horii, J. W. Munger, and S. C. Wofsy. Fluxes of nitrogen oxieds over a temperature deciduous forest. *Journal of Geophysical Research*, 109:D08305, 2004.

[52] L. W. Horowitz, A. M. Fiore, G. P. Milly, R. C. Cohen, A. Perring, P. J. Wooldridge, P. G. Hess, L. K. Emmons, and J.-F. Lamarque. Observational contraints on the chemistry of isoprene nitrates over the eastern united states. *Journal of Geophysical Research*, 112:D12S08, 2007.

[53] R. C. Hudman, L. T. Murray, D. J. Jacob, D. B. Millet, S. Turquety, S. Wu, D. R. Blake, A. H. Goldstein, J. Holloway, and G. W. Sachse. Biogenic vs anthropogenic sources of co in the united states. *Geophysical Research Letters*, 35:L04801, 2008.

[54] A. Ito, S. Sillman, and J. E. Penner. Global chemical transport model study of ozone response to changes in chemical kinetics and biogenic volatile organic compounds emissins due to increasing temperatures: Sensitivities to isoprene nitrate chemistry and grid resolution. *Journal of Geophysical Research*, 114:D09301, 2009.

[55] D. J. Jacob. Documentation and evaluation of the geos-chem simulation for 2002. Technical report, Harvard University, June 24 2005.

[56] Daniel J. Jacob. Introduction to atmospheric chemistry. 1999.

[57] Mark Z. Jacobson. *Fundamentals of Atmospheric Modeling*. Cambridge University Press, Cambridge, 2005.

[58] R. T. Jongma, M. G. H. Boogaarts, I. Holleman, and G. Meijer. Trace gas-detection with cavity ring down spectroscopy. *Review of Scientific Instruments*, 66(4):2821–2828, 1995. ISI Document Delivery No.: QT331 Times Cited: 110 Cited Reference Count: 17 English Article 0034-6748.

[59] S.-W. Kim, A. Heckel, S.A. McKeen, G.J. Frost, E.-Y. Hsie, M.K. Trainer, A. Richter, J.P. Burrows, S.E. Peckham, and G.A. Grell. Satellite-observed u.s. power pland nox emission reductions and their impact on air quality. *Geophysical Research Letters*, 33:GL027749, 2006.

[60] Lawrence I. Kleinman, William F. Ryan, Peter H. Daum, Stephen R. Springston, Yin-Nan Lee, Linda J. Nunnermacker, and Judith Weinstein-Lloyd. An ozone episode in the philadelphia metropolitan area. *Journal of Geophysical Research*, 109:D20302, 2004.

[61] Hampden D Kuhns, Claudio Mazzoleni, Hans Moosmuller, Djordje Nikolic, Robert E Keislar, Peter W Barber, Zheng Li, Vicken Etyemezian, and John G Watson. Remote sensing of pm, no, co and hc emission factors for on-road gasoline and diesel engine vehicles in las vegas, nv. *Science of the Total Environment*, 322:123–137, 2004.

[62] Winston T. Luke, Paul Kelley, Barry L. Lefer, James Flynn, Bernhard Rappenglck, Michael Leuchner, Jack E. Dibb, Luke D. Ziemba, Casey H. Anderson, and Martin Buhr. Measurements of trace gases and noy composition in houston, texas. *Atmospheric Environment*, 2009.

[63] V. Mallet and B. Sportisse. Uncertainty in a chemistry-transport model due to physical parameterizations and numerical approximations: An ensemble approach applied to ozone modeling. *Journal of Geophysical Research*, 111:D01302, 2006.

[64] Amit Marmum, Wei Liu, Yuhang Wang, Armistead G Russell, and Eric S Edgerton. Evaluation of model simulated atmospheric constituents with observations in the factor projected space: Cmaq simulations of search measurements. *Atmospheric Environment*, 43:1839–1849, 2009.

[65] L.C. Marr, D.R. Black, and R.A. Harley. Formation of photochemical air pollution in central california: 1. development of a revised motor vehicle emission inventory. *Journal of Geophysical Research*, 107(D6):5–1:5–9, 2002.

[66] M. Mazurenka, R. Wada, A. J. L. Shillings, T. J. A. Butler, J. M. Beames, and A. J. Orr-Ewing. Fast fourier transform analysis in cavity ring-down spectroscopy: application to an optical detector for atmospheric no2. *Applied Physics B: Lasers and Optics*, 81(1):135, 2005. 10.1007/s00340-005-1834-1.

[67] Stanley Middleman. *An Introduction to Fluid Mechanics*. John Wiley and Sons, Inc., New York, 1998.

[68] D. Mihelcic, P. Musgen, and D. H. Ehhalt. An improved method of measuring tropospheric no2 and ro2 by matrix-isolation and electron-spin-resonance. *Journal of Atmospheric Chemistry*, 3(3):341–361, 1985. ISI Document Delivery No.: A0292 Times Cited: 56 Cited Reference Count: 19 English Article 0167-7764.

[69] J. M. Moxley and K. A. Smith. Factors affecting utilization of atmospheric co by soils. *Soil Biology and Biochemistry*, 30:65–79, 1998.

[70] C.F. Murphy and D.T. Allen. Hydrocarbon emissions from industrial release events in the houston-galveston area and their impact on ozone formation. *Atmospheric Environment*, 39:3785–3798, 2005.

[71] J. Nam, M. Webster, Y. Kimura, H. Jeffries, W. Vizuete, and D.T. Allen. Reductions in ozone concentration due to controls on variability in industrial flare emissions in houston, texas. *Atmospheric Environment*, 42:4198–4211, 2008.

[72] P. Nowacki, P. J. Samson, and S. Sillman. Sensitivity of urban airshed model (uam-iv) calculated air pollution concentrations to the vertical diffusion parameterization during convective meteoroloical situations. *Journal of Applied Meteoroloy*, 35:1790–1803, 1996.

[73] New York State Department of Environmental Conservation (NYSDEC). Cmaq model performance and assessment 8-h otc ozone modeling. Technical Report TSD-1e, 2006.

[74] New York State Department of Environmental Conservation (NYSDEC). Meteorological modeling using penn state /ncar 5th generation mesoscale model (mm5). Technical Report TSD-1a, 2006.

[75] New York State Department of Environmental Conservation (NYSDEC). Processing of biogenic emissions for otc/mane-vu modeling,. Technical Report TSD-1b, 2006.

[76] University of North Carolina (UNC). Smoke v2.2 users manual, 2008.

[77] A. O'Keefe, J. J. Scherer, J. B. Paul, and R. J. Saykally. *Cavity Ring-Down Spectroscopy*. ACS, Washington, DC, 1999.

[78] Anthony O'Keefe and David A. G. Deacon. Cavity ring-down optical spectrometer for absorption measurements using pulsed laser sources. *Review of Scientific Instruments*, 59(12):2544, 1988.

[79] D. D. Parrish and F. C. Fehsenfeld. Methods for gas-phase measurements of ozone, ozone precursors and aerosol precursors. *Atmospheric Environment*, 34(12-14):1921–1957, 2000. ISI Document Delivery No.: 299JP Times Cited: 52 Cited Reference Count: 242 English Review 1352-2310.

[80] David D Parrish. Critical evaluation of us on-road vehicle emissions inventory. *Atmospheric Environment*, 40:2288–2300, 2006.

[81] E. H. Pechan and Associates Inc. (Pechan). Technical support document for 2002 mane-vu sip modeling inventories version 3, final report to the mid-atlantic/northeast visibility union. Technical report, 2006.

[82] A. E. Perring, T. H. Bertram, P. J. Wooldridge, A. Fried, B. J. Heikes, J. Dibb, J. D. Crounse, P. O. Wennberg, N. J. Blake, D. R. Blake, W. H. Brune, H. B. Singh, and R. C. Cohen. Airborne observations of total rono2: new contraints on the yield and lifetime of isoprene nitrates. *Atmospheric Chemistry and Physics*, 9:1451–1463, 2009.

[83] M. Placet, C.O. Mann, R.O. Gilbert, and M.J. Niefer. Emissions of ozone precursors from stationary sources: a critical review. *Atmospheric Environment*, 34:2183–2204, 2000.

[84] A. K. Pollack, C. Lindhjem, T. E. Stoecknius, C. Tran, G. Mansell, M. Jimenez, G. Wilson, and S. Coulter-Burke. Evaluation of the u.s. epa mobile6 highway vehicle emission factor model. Technical report, 2004.

[85] S. Rao, J-Y. Ku, S. Berman, K. Zhang, and H. Mao. Summertime characteristics of the atmospheric boundary layer and relationships to ozone levels over the eastern united states. *Pure and Applied Geophysics*, 160:21–55, 2003.

[86] B. A. Ridley, M. A. Carroll, A. L. Torres, E. P. Condon, G. W. Sachse, G. F. Hill, and G. L. Gregory. An intercomparison of results from ferrous sulphate and photolytic converter techniques for measurements of nox made during the nasa gte/cite 1 aircraft program. *Journal of Geophysical Research, [Atmospheres]*, 93(D12):15,803–15,811, 1988.

[87] D. Romanini, A. A. Kachanov, and F. Stoeckel. Diode laser cavity ring down spectroscopy. *Chemical Physics Letters*, 270(5-6):538–545, 1997. ISI Document Delivery No.: XB517 Times Cited: 117 Cited Reference Count: 23 English Article 0009-2614.

[88] J.B. Ruidavets, M.Cournot, S. Cassadou, M.Giroux, M. Meybeck, and J.Ferrieres. Ozone air pollution is associated with acute myocardial infarction. *Circulation*, 111:563–569, 2005.

[89] W. F. Ryan, B. G. Doddridge, R. R. Dickerson, R. M. Morales, and K. A. Hallock. Pollutant transport during a regional ozone episode in the mid-atlantic states. *Journal of the Air and Waste Management Association*, 48:786–797, 1998.

[90] S. T. Sandholm, J. D. Bradshaw, K. S. Dorris, M. O. Rodgers, and D. D. Davis. An airborne compatible photofragmentation two-photon laser-induced fluorescence instrument for measuring background tropospheric levels of no, no x, and no2. *Journal of Geophysical Research, [Atmospheres]*, 95:10155–10161, 1990. 10.1029/JD095iD07p10155.

[91] E. Sanhueza, Y. Dong, D. Scharffe, J. M. Lobert, and P. J. Crutzen. Carbon monoxide uptake by temperate forest soils: the effects of leaves and humus layers. *Tellus*, 50B:51–58, 1998.

[92] Amir Sapkota, J. Morel Symons, Jan Kleissl, Lu Wang, Marc B. Parlange, John Ondov, Patrick N. Breysse, Gregory B. Diette, Peyton A. Eggleston, and Timothy J. Buckley. Impact of the 2002 canadian forest fireson particulate matter air quality in baltimore city. *Environmental Science and Technology*, 39:24–32, 2005.

[93] D. Scharffe, W. M. Hao, L. Donoso, P. J. Crutzen, and E. Sanhueza. Soil fluxes and atmospheric concentration of co and ch4 in the norther part of the guyana shield, venezuela. *Journal of Geophysical Research*, 95:22475–22480, 1990.

[94] J. J. Scherer, D. Voelkel, D. J. Rakestraw, J. B. Paul, C. P. Collier, R. J. Saykally, and A. Okeefe. Infrared cavity ringdown laser-absorption spectroscopy (ir-crlas). *Chemical Physics Letters*, 245(2-3):273–280, 1995. ISI Document Delivery No.: TB703 Times Cited: 88 Cited Reference Count: 20 English Article 0009-2614.

[95] Bret A. Schichtel and Rudolf B. Husar. Eastern north american transport climatology during high- and low-ozone days. *Atmospheric Environment*, 35:1029–1038, 2001.

[96] J.H. Seinfeld and S.N. Pandis. *Atmospheric chemistry and physics: from air pollution to climate change*. John Wiley and Sons, Inc., Hoboken, New Jersey, 2006.

[97] J. M. Sigler, X. Lee, and W. Munger. Emissions and long-range transport of gaseous mercury from a large-scale canadian boreal forest fire. *Environmental Science and Technology*, 37:4343–4347, 2003.

[98] M. Sprengnether, K. L. Demerjian, N. M. Donahue, and J. G. Anderson. Product analysis of the oh oxidation of isoprene and 1,3-butadiene in the presense of no. *Journal of Geophysical Research*, 107:4268, 2002.

[99] D. H. Stedman. A flow independent procedure for the gas phase titration of an ozone source. *Journal of the Air Pollution Control Association*, 26:62, 1976.

[100] R. K. Stevens, R. J. Drago, and Y. Mamane. A long path differential optical-absorption spectrometer and epa-approved fixed-point methods intercomparison. *Atmospheric Environment, Part B: Urban Atmosphere*, 27(2):231–236, 1993. ISI Document Delivery No.: LQ788 Times Cited: 13 Cited Reference Count: 9 English Article 0957-1272.

[101] Z. Tao, S.M. Larson, A. Williams, M. Caughey, and D.J. Wuebbles. Sensitivity of regional ozone concentrations to temporal distribution of emissions. *Atmospheric Environment*, 38:6279–6285, 2004.

[102] B. F. Taubman, B. L. Vant-Hull, C. A. Piety, B. G. Doddridge, R. R. Dickerson, and Z. Li. Smoke over haze: Aircraft observations of chemical and optical properties and the effects on heating rates and stability. *Journal of Geophysical Research*, 109:D02206, 2004.

[103] B.T. Taubman, L.T. Marufu, C.A. Piety, B.G. Doddridge, J.W. Stehr, and R.D. Dickerson. Airborne characterization of the chemical, optical, and meteorological properties, and origins of a combined ozone-haze episode over the eastern united states. *Journal of the Atmospheric Sciences*, 61:1781–1793, 2004.

[104] U.S. Environmental Protection Agency (USEPA). Compilation of photochemical models' performance statistic for 11/94 ozone sip applications. Technical report, 1996.

[105] U.S. Environmental Protection Agency (USEPA). The ozone report: Measuring progress through 2003. Technical report, 2004.

[106] U.S. Environmental Protection Agency (USEPA). Air quality criteria and for ozone and related photochemical oxidants, 2006.

[107] Gary W. vanLoon and Stephen J. Duffy. *Environmental Chemistry*. Oxford, New York, 2000.

[108] R. Vasudev, A. Usachev, and W. R. Dunsford. Detection of toxic compounds by cavity ring-down spectroscopy. *Environmental Science and Technology*, 33(11):1936–1939, 1999.

[109] F. M. Vukovich. Boundary layer ozone variations in the eastern united states and their association with meteorological variations: Long-term variations. *Journal of Geophysical Research*, 99:16,839–16,850, 1994.

[110] Fred M. Vukovich and James Scarborough. Aspects of ozone transport, mixing, and chemistry in the greater maryland area. *Atmospheric Environment*, 39:7008–7019, 2005.

[111] Fred M. Vukovich and John Sherwell. An examination of the relationship between certain meteorological parameters andsurface ozone variations in the baltimorewashington corridor. *Atmospheric Environment*, 37:971–981, 2003.

[112] R. Wada and A. J. Orr-Ewing. Continuous wave cavity ring-down spectroscopy measurement of no2 mixing ratios in ambient air. *Analyst*, 130(12):1595–1600, 2005. ISI Document Delivery No.: 983PD Times Cited: 12 Cited Reference Count: 24 English Article 0003-2654.

[113] S. Wang, R. Ackermann, C. W. Spicer, J. D. Fast, M. Schmeling, and J. Stutz. Atmosperic observations of enhanced no2-hono conversion on mineral dust particles. *Geophysical Research Letters*, 30:1595, 2003.

[114] C Warneke, J. A. de Guow, A. Stohl, O. R. Cooper, P. D. Goldan, W. C. Kuster, J. S. Holloway, E. J. Williams, B. M. Lerner, S. A. McKeen, M. Trainer, F. C. Fehsenfeld, E. L. Atlas, S. G. Donnelly, Verity Stroud, Amy Lueb, and S. Kato. Biomass burning and anthropogenic sources of co over new england in the summer of 2004. *Journal of Geophysical Research*, 111:D23S15, 2006.

[115] M. Webster, J. Nam, Y. Kimura, H. Jeffries, W. Vizuete, and D.T. Allen. The effect of variability in industrial emissions on ozone formation in houston, texas. *Atmospheric Environment*, 41:9580–9593, 2007.

[116] M. D. Wheeler, S. M. Newman, A. J. Orr-Ewing, and M. N. R. Ashfold. Cavity ring-down spectroscopy. *Journal of the Chemical Society, Faraday Transactions*, 94(3):337–351, 1998. ISI Document Delivery No.: YW963 Times Cited: 184 Cited Reference Count: 119 English Review 0956-5000.

[117] M.C. White, R.A. Etzel, W.D. Wilcox, and C. Lloyd. Exacerbations of childhood asthma and ozone pollution in atlanta. *Environmental Research*, 65:56–68, 1994.

[118] D.J. Williams, W.T. Potter, W.W. Clarkson, D.A. Sanders, and J.E. Stevens. The impact of background ozone on compliance with revised national ambient air quality standards. *Journal of the Air and Waste Management Association*, 59:52–57, 2009.

[119] Kevin L. Wilson and John W. Birks. Mechanism and elimination of water vapor interference in the measurement of ozone by uv absorbance. *Environmental Science and Technology*, 40(20):6361–6367, 2006.

[120] G.W. Wong, F.W. Ko, T.S. Lau, S.T. Li, D. Hui, S.W. Pang, R. Leung, T.F. Fok, and C.K.W. Lai. Temporal relationship between air pollution and hospital admissions for asthmatic children in hong kong. *Clinical and Experimental Allergy*, 31:565–569, 2001.

[121] S. Wu, L. J. Mickley, D. J. Jacob, J. A. Logan, R. M. Yantosca, and D. Rind. Why are there large differences between models in global budgets of tropospheric ozone? *Journal of Geophysical Research*, 112:D05302, 2007.

[122] S. Yonemura, S. Kawashima, and H. Tsuruta. Continuous measurements of co and h2 deposition velocities onto an andisol. *Tellus*, 51B:688–700, 1999.

[123] S. Yonemura, S. Kawashima, and H. Tsuruta. Carbon monoxide, hydrogen, and methane uptake by soils in a temperate arable field and a forest, 2000.

[124] S Yu, R Mathur, G Sarwar, D Kang, D Tong, G Pouliot, and J Pleim. Eta-cmaq air quality forecasts for o3 and related species using three different photochemical mechanisms (cb4, cb05, saprc-99): comparisons with measurements during the 2004 icartt study. *Atmospheric Chemistry and Physics Discussions*, 9:22955–22992, 2009.

[125] Shaocai Yu, Rohit Mathur, Kenneth Schere, Daiwen Kang, Jonathan Pleim, and Tanya Otte. A detailed evaluation of the eta-cmaq forecast model performance for o3, its related precursors, and meteorological parameters during the 2004 icartt study. *Journal of Geophysical Research*, 112:D12S14, 2007.

[126] D.-L. Zhang, X.-Y. Shou, and R.R. Dickerson. Upstream urbanization exacerbates urban heat island effects. *Geophysical Research Letters*, doi:10.1029/2009GL041082, 2009.

[127] D.L. Zhang and W.Z. Zheng. Diurnal cycles of surface winds and temperatures as simulated by five boundary layer parameterizations. *Journal of Applied Meteorology*, 43:157–169, 2004.